



THE HONG KONG  
POLYTECHNIC UNIVERSITY

香港理工大學

Pao Yue-kong Library

包玉剛圖書館

---

## Copyright Undertaking

This thesis is protected by copyright, with all rights reserved.

**By reading and using the thesis, the reader understands and agrees to the following terms:**

1. The reader will abide by the rules and legal ordinances governing copyright regarding the use of the thesis.
2. The reader will use the thesis for the purpose of research or private study only and not for distribution or further reproduction or any other purpose.
3. The reader agrees to indemnify and hold the University harmless from and against any loss, damage, cost, liability or expenses arising from copyright infringement or unauthorized usage.

### IMPORTANT

If you have reasons to believe that any materials in this thesis are deemed not suitable to be distributed in this form, or a copyright owner having difficulty with the material being included in our database, please contact [lbsys@polyu.edu.hk](mailto:lbsys@polyu.edu.hk) providing details. The Library will look into your claim and consider taking remedial action upon receipt of the written requests.

**The Hong Kong Polytechnic University**

**Department of Electronic and Information Engineering**

**Design of a Transcutaneous Power Regulator  
for Artificial Hearts**

**Kam-Cheung Tang**

**A thesis submitted in partial fulfilment of the requirements for  
the degree of Master of Philosophy**

**December 2010**

## **CERTIFICATE OF ORIGINALITY**

I hereby declare that this thesis is my own work and that, to the best of my knowledge and belief, it reproduces no material previously published or written, nor material that has been accepted for the award of any other degree or diploma, except where due acknowledgement has been made in the text.

\_\_\_\_\_ (Signed)

Kam-Cheung Tang (Name of Student)

*To my mother*

# Abstract

A high-efficiency transcutaneous power regulator for artificial hearts with pulse-width-modulation phase-locked-loop (PWM-PLL) control has been built with a digital signal processor (DSP) as the primary side controller, and a new method of sensing the output voltage inside the human body utilizing the same power transcutaneous transformer as the medium for signal transmission is introduced. The feedback signal is modulated in the secondary in a frequency band above the PWM-PLL cut-off frequency and below the converter switching frequency. In this way, the feedback signal can be demodulated from the primary current that can be measured. A SPICE macromodel for the double-tuned resonant converter is developed to help design the control loop and the selection of modulation-demodulation frequency bands.

A hardware prototype using a single-chip DSP together with analog filters was built and the control software was implemented in DSP program codes. A phase-locked-loop (PLL) switching frequency locking function is constructed by using an on-chip analog comparator. It saves extra hardware for the PLL control. Using a DSP controller, closed-loop stability control can be implemented as software codes and digital control algorithms are used in the system design. The steady-state voltage loop control algorithm uses a modified PI controller with input voltage feed-forward. Another software module is added to shorten the time of output voltage transient in the event of an output load change. This algorithm is based on the response characteristics of the primary side inductor current and output loading estimation.

The power efficiency of the regulator system is optimized by setting the switching frequency close to the resonant point. The resulting efficiency is between 87% and 94% for the output load power from 12W to 60W. For a more restricted output power range commonly used by artificial heart systems (15W – 35W), the power efficiency is over 90% for all loads.

# Publications

## Papers

1. Kam-Cheung Tang, Siu-Cheung Wong, and Chi K. Tse, “Design of a closed-loop transcutaneous power regulator for artificial hearts,” *IEEE Transactions on Biomedical Circuits and Systems*, submitted.
2. Kam-Cheung Tang, Siu-Cheung Wong, and Chi K. Tse, “Design of a transcutaneous power regulator for artificial hearts,” in *Proceedings of 2nd IEEE International Symposium on Power Electronics for Distributed Generation Systems (PEDG 2010)*, June 2010, pp. 89-95, Hefei, China.

# Acknowledgements

Firstly, I would like to thank my supervisors, Dr. S. C. Wong and Prof. C. K. Tse, for their valuable advices, patient guidance, and encouragement.

Secondly, I am grateful to the people and technical staff, whom I have met in the laboratory, for their friendship and help: Dr. Y. M. Lai, Dr. S. C. Tan, Mr. S. Y. Lam, Dr. Sufen Chen, Alun Lun, Barry Mok, Nick Ng and Roger Yau.

Finally, special thanks go to my mother and my siblings for their understanding and support.

# Table of Contents

Abstract.....	i
Publications.....	ii
Acknowledgements.....	iii
Table of Contents.....	iv
List of Figures.....	vi
List of Tables.....	viii
Nomenclature List.....	ix
Chapter 1 Introduction.....	1
1.1 Background.....	1
1.2 Near Field and Far Field.....	3
1.3 Inductive Coupling and Capacitive Coupling.....	6
1.4 Literature Review.....	6
1.4.1 TET System Development.....	6
1.4.2 Secondary Voltage Feedback and Data Telemetry.....	12
1.4.3 Secondary Side Battery.....	15
1.4.4 Health Issue: Tissue Heating & EM Fields Radiation.....	18
1.5 Objectives of the Thesis.....	20
1.6 Overview of the Thesis.....	20
Chapter 2 System Modelling.....	21
2.1 Transcutaneous Transformer.....	21
2.2 Topology of Compensation Networks.....	22
2.3 Phase-Shifted Full-Bridge Operations.....	24
2.4 AC Equivalent Circuit.....	27
2.5 Relationship between Input Voltage and Primary Current.....	29
2.5.1 Full Duty Ratio Control.....	29
2.5.2 PWM Control.....	31
2.6 SPICE Macromodel.....	34
2.6.1 Line-to-Output Converter Response.....	38
2.6.2 (AC) Output Voltage-to-Primary Current Response.....	39
Chapter 3 System Design.....	42
3.1 Primary Side Controller Board.....	42
3.1.1 Primary Side DSP Functional Requirements.....	42
3.1.2 Primary Side DSP Selection.....	43

3.1.3	Inductor Coils Selection.....	45
3.1.4	Resonance Capacitors Selection.....	47
3.1.5	Power MOSFETs Selection.....	48
3.1.6	Rectifier Diodes Selection.....	49
3.1.7	Hardware Prototype Board.....	49
3.2	Secondary Side Controller Board.....	52
3.3	Switching Frequency Control.....	54
3.4	Secondary Output Voltage Feedback Control .....	58
3.5	Voltage Loop Control .....	61
3.6	Effect of Duty Ratio on Output Voltage (Input Voltage Feed-forward) .....	64
3.7	Transient Output Voltage Control .....	64
Chapter 4	Experimental Results .....	68
4.1	Essential Waveforms at Steady-State .....	68
4.2	Output Voltage Transient Response .....	73
4.3	Frequency Tracking With Moving Gap.....	76
4.4	Converter Efficiency .....	77
4.5	Loss Analysis .....	78
Chapter 5	Conclusion.....	86
5.1	Summary .....	86
5.2	Contributions.....	86
5.3	Suggestions for Future Work.....	87
5.3.1	Simpler Control Algorithm – No PWM Control .....	87
5.3.2	Data Logging with PC and Search for Better Control Algorithm .....	88
5.3.3	AC Input Power Regulator.....	88
5.3.4	Testing with Non-Resistive Load and Battery Charging.....	89
5.3.5	Secondary Side Rectification and Tone Signalling using Synchronous	
Rectifiers		90
Appendix 1	Circuit Diagram of Primary Side Controller Board .....	91
Appendix 2	Circuit Diagram of Secondary Side Controller Board .....	93
Appendix 3	SPICE Circuit File for Line-to-Output Response Generation (Gap = 10	
mm)		94
Appendix 4	SPICE Circuit File for Ip Response Generation (Gap = 20 mm) .....	98
Appendix 5	ADC & Comparator Resolution Requirements.....	102
References.....		104

# List of Figures

Figure 1-1:	Near field and far field regions .....	3
Figure 1-2:	A spherical co-ordinate system around a short current carrying wire [1] .....	4
Figure 2-1:	Transcutaneous Transformer .....	21
Figure 2-2:	Basic topologies for primary and secondary compensation network [66] .....	22
Figure 2-3:	Phase-shifted full-bridge operations.....	24
Figure 2-4:	Transcutaneous power regulator .....	27
Figure 2-5:	Input-to-output voltage transfer ratio .....	28
Figure 2-6:	Relationship between primary current $I_P$ and input voltage $V_S$ at resonant frequency for different loading conditions.....	29
Figure 2-7:	Current cut level at different switching frequency ( $V_{IN} = 30$ V, gap = 10 mm, full duty ratio) .....	31
Figure 2-8:	Primary current cutting level for different loads.....	33
Figure 2-9:	SPICE macromodel transformation for $R, L, C$ elements .....	36
Figure 2-10:	SPICE macromodel for circuit simulation .....	37
Figure 2-11:	Line-to-output response of TET circuit.....	38
Figure 2-12:	SPICE macromodel with ac $V_{tone}$ at output side.....	39
Figure 2-13:	Frequency response of primary current to secondary tone signal.....	40
Figure 3-1:	Block diagram of dsPIC33FJ16GS502 DSP [138] .....	44
Figure 3-2:	Primary side controller board and transcutaneous transformer.....	49
Figure 3-3:	Expanded view to show the current pick-up toroid.....	51
Figure 3-4:	Secondary side rectifier board.....	51
Figure 3-5:	Mechanical setup for transcutaneous transformer.....	52
Figure 3-6:	Block diagram of PIC12F615 MCU [139].....	53
Figure 3-7:	Secondary side controller board.....	54
Figure 3-8:	Block diagram of analog PLL .....	54
Figure 3-9:	Loop filter for CPPLL.....	55
Figure 3-10:	Block diagram of all-digital PLL .....	56
Figure 3-11:	Frequency response of primary current to secondary tone signal for different output load $R_L$ .....	60
Figure 3-12:	Converter response using PI compensation .....	62
Figure 3-13:	Time delay for tone signal from secondary side to primary.....	63

Figure 3-14: Output voltage $V_O$ and primary current $I_P$ during load transient from 9.6 $\Omega$ to 48 $\Omega$ (no PWM control) .....	65
Figure 4-1: Converter waveforms at gap separation of 10 mm ( $V_{IN} = 30$ V).....	69
Figure 4-2: Converter waveforms at gap separation of 20 mm ( $V_{IN} = 30$ V).....	70
Figure 4-3: Converter waveforms at gap separation of 15 mm ( $V_{IN} = 30$ V).....	71
Figure 4-4: Converter waveforms at gap separation of 15 mm ( $V_{IN} = 45$ V).....	72
Figure 4-5: Output voltage response during load transient, $V_{IN} = 30$ V, $k = 0.51$ .....	74
Figure 4-6: Output voltage variation during transformer gap movement .....	75
Figure 4-7: Output voltage when no frequency control is made during gap movement...	76
Figure 4-8: Measured converter efficiency .....	77
Figure 4-9: PSFB PWM operating modes for resonant converter [148].....	82
Figure 4-10: Loss analysis of the transcutaneous power regulator at $V_{IN} = 30$ V and two different gap separations .....	83

# List of Tables

Table 1-1:	Frequency Bands Designation and Their Wavelength .....	5
Table 1-2:	Throughput Requirement for Medical Sensing Devices [99] .....	15
Table 1-3:	SAR Limits according to ICNIRP.....	19
Table 2-1:	Measured parameters for transcutaneous transformer.....	22
Table 2-2:	Parameters for SPICE Macromodel .....	37
Table 3-1:	Comparison between TI's DSP and Microchip's DSP .....	44
Table 3-2:	Skin Depth of Copper Wire at Various Frequencies.....	46
Table 3-3:	AWG Gauges Table.....	46
Table 3-4:	Measured Results of Transcutaneous Transformer Coils .....	47
Table 3-5:	Tone Frequency Assignment for Secondary Output Voltage.....	60
Table 3-6:	Data Coefficients for Goertzel Algorithm .....	61
Table 4-1:	Series Resistances for Resonant Tank Components.....	80
Table 4-2:	Power Losses Calculation .....	84

# Nomenclature List

Symbol	Description
$C_P$	Primary side compensation capacitor
$C_S$	Secondary side compensation capacitor
$D$	Duty ratio
$f_r$	Resonant frequency
$f_s$	Switching frequency
$I_P$	Primary inductor current
$I_S$	Secondary inductor current
$k$	Transformer coupling coefficient
$L_1$	Primary side leakage inductance
$L_2$	Secondary side leakage inductance
$L_M$	Transformer mutual inductance
$L_P$	Transformer primary inductance
$L_S$	Transformer secondary inductance
$n$	Transformer turns ratio
$V_{IN}$	Input supply voltage
$V_O$	Secondary output voltage
$V_S$	Equivalent input ac voltage

# Chapter 1 Introduction

## 1.1 Background

With the increasing number of biomedical devices implanted inside the human body, methods of providing safe power sources to these devices have been studied for a long time. Power supplies through direct wiring are not encouraged because these methods of power delivery have the potential risk of infection associated with wires across the skin. On the other hand, Transcutaneous Energy Transfer (TET) with power coupling through the skin without direct electrical connectivity becomes favourable. The TET technique is implemented through a transcutaneous transformer where the primary and the secondary coils are separated by the patient's skin, forming two electrically isolated systems during the process of power transfer. A common way of power transfer is through an inductive power link. Inductive powering has been a reliable and simple method to wirelessly transfer power and data over short distances.

In this thesis, the design of a transcutaneous power regulator for artificial hearts is discussed, and a new method of passing secondary output voltage information to the primary for closed-loop regulation is proposed.

To begin with, it will be instructive to know what devices are now implanted inside the human body, and what their typical power requirements are. The following is a list of implantable biomedical devices that can be found inside the human body:

- Cochlear implants, also known as bionic ears, are surgically-implanted electronic devices that partially restore hearing of deaf people by applying electric stimulation to the auditory nerve. The power consumption is  $< 60$  mW. They are powered by inductive coupling.
- Retinal implants in the visual cortex help restore vision either through retina stimulation via the optical nerve or directly stimulating the cortex. The power consumption is 3.2 mW, and they are also powered by inductive coupling.
- Cardiac pacemakers are devices that help regulate heart rhythms and restore the heart's pumping function through electrical stimulation. The natural rhythmic electrical signals from the atria are detected and processed, and the output is a properly timed sequence of pulses to stimulate the ventricles to contract. The power consumption is in the order of 100  $\mu$ W. Energy source may be provided by lithium-ion batteries.

- Implantable cardioverter-defibrillators (ICD) are small battery-powered electrical impulse generators which are implanted in patients who are at risk of sudden cardiac death due to ventricular fibrillation and ventricular tachycardia. The devices are programmed to detect cardiac arrhythmia and correct it by delivering a jolt of electricity. A power of 4-6 W for a period of 6 to 15 seconds is required during the time of electrical shock generation. At normal time, the power consumption is low. Nowadays, the functions of pacemakers and defibrillators are usually combined together and the final devices are commonly referred to as ICD.
- Implantable drug delivery systems deliver metered doses of a drug to localized sites, eliminating the requirement of manual handling. In addition, drug doses can be delivered to the disease location in a highly concentrated form that would be damaging to the body if delivered in a traditional manner. The drug delivery system may be implemented with implantable micro-electro-mechanical systems (MEMS). The device would be permanently implanted and capable of delivering daily doses of a drug for up to 1 year. The power requirement of the system is typically  $\sim 370 \mu\text{W}$ . Power and communication with the device would be provided by wireless links that would only be activated when required.
- The capsule endoscope is not a real implant, but a wireless electronic system that operates over the entire length of the small intestine. It captures the internal image by camera and delivers the image in real time by a radio link. Typical power consumption is  $\sim 128.4 \text{ mW}$ . The device may be powered by a small size battery, but for longer time operation and higher quality video images, the device will be powered by inductive coupling.
- BMI (brain-man-interface) is a set of sensors that is implanted inside the brain that records activity of different regions of the brain. The power consumption depends on the number of sensors. A typical value is  $\sim 13.5 \text{ mW}$ . The sensors may be powered by implanted battery or via inductive coupling.

Another device that can be implanted inside the human body is the artificial heart, and it is used to replace the normal heart. The main functions include circulation of the blood flow within the human body and regulation of the blood pressure within a normal level range. Due to the operation of the blood pump, the power consumption for the artificial heart is much higher than all other implants. It is ranged from 15 W to 35 W. The power requirement for the artificial heart system is much higher than the other implanted devices. Thus, the

power supply requires larger coils for the transcutaneous transformer so that sufficient energy can be provided by the inductive link.

## 1.2 Near Field and Far Field

The setup of wireless links for transfer of power or information involves the use of electromagnetic (EM) radiation. If the electromagnetic waves are time varying, then there will be interaction between the magnetic fields and the electric fields, and they are related to each other by Maxwell's equations.

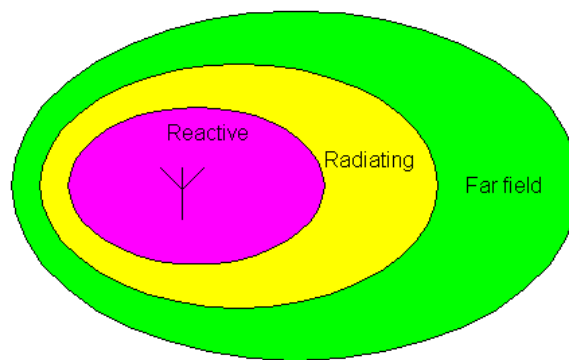
$$\vec{\nabla} \times \vec{E} = -\frac{\partial \vec{B}}{\partial t} \quad (\text{Faraday's law}) \quad (1.1)$$

$$\vec{\nabla} \times \vec{H} = \frac{\partial \vec{D}}{\partial t} + \vec{J} \quad (\text{Ampere's law}) \quad (1.2)$$

$$\vec{\nabla} \cdot \vec{D} = \rho \quad (\text{Gauss's law}) \quad (1.3)$$

$$\vec{\nabla} \cdot \vec{B} = 0 \quad (1.4)$$

where  $\vec{D}$  represents the electric displacement,  $\vec{E}$  the electric field strength,  $\vec{J}$  the free electric current density,  $\vec{B}$  the magnetic flux density,  $\vec{H}$  the magnetic field strength, and  $\rho$  the free electric-charge density. All variables are functions of position and time.



Near field = Reactive + Radiating

Figure 1-1: Near field and far field regions

When a transmitting source (usually called an antenna) is generating EM waves, according to the EM-field characteristics, the space surrounding it can be divided into two main regions, namely, far field and near field, as illustrated in Figure 1-1. In the far field, electric and magnetic fields propagate outward as electromagnetic waves and are perpendicular to each other and to the direction of propagation. The angular field distribution

does not depend on the distance from the transmitting source,  $r$ . The fields are uniquely related to each other via free-space impedance and decay as  $1/r$ .

In the near field, the field components have different angular and radial dependence (e.g.,  $1/r^3$ ). The near-field region includes two sub-regions: *radiating*, where the angular field distribution is dependent on the distance, and *reactive*, where the energy is stored but not radiated.

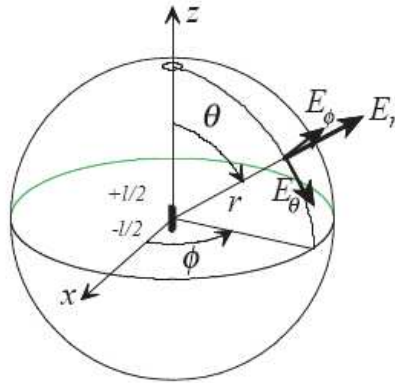


Figure 1-2: A spherical co-ordinate system around a short current carrying wire [1]

Consider an example of a short wire in free space carrying an alternating current  $I$ , as shown in Fig. 1-2 [1], where  $i = I \sin(\omega t)$ . The wire length  $l$  is assumed to be much smaller than the wavelength  $\lambda$ . Solving the Maxwell equations in spherical co-ordinates produces [3, pp. 165-167)

$$E_r = -\sqrt{\frac{\mu}{\epsilon}} \frac{I \cdot l \cdot \cos \theta}{r \lambda} \left[ \frac{1}{4\pi^2} \frac{\lambda^2}{r^2} \cos\left(2\pi \frac{r}{\lambda} - \omega t\right) + \frac{1}{2\pi} \frac{\lambda}{r} \sin\left(2\pi \frac{r}{\lambda} - \omega t\right) \right] \quad (1.5)$$

$$E_\theta = \sqrt{\frac{\mu}{\epsilon}} \frac{I \cdot l \cdot \sin \theta}{2r \lambda} \left[ \frac{1}{4\pi^2} \frac{\lambda^2}{r^2} \cos\left(2\pi \frac{r}{\lambda} - \omega t\right) + \frac{1}{2\pi} \frac{\lambda}{r} \sin\left(2\pi \frac{r}{\lambda} - \omega t\right) + \cos\left(2\pi \frac{r}{\lambda} - \omega t\right) \right] \quad (1.6)$$

$$E_\phi = H_r = H_\theta = 0 \quad (1.7)$$

$$H_\phi = \frac{I \cdot l \cdot \sin \theta}{2r \lambda} \left[ -\frac{1}{2\pi} \frac{\lambda}{r} \sin\left(2\pi \frac{r}{\lambda} - \omega t\right) + \cos\left(2\pi \frac{r}{\lambda} - \omega t\right) \right] \quad (1.8)$$

At distances  $r$  much smaller than a wavelength  $\lambda$  from the current-carrying wire, the highest-order terms in  $\lambda/r$  dominate and the equations reduce to quasi-stationary equations of two oscillating  $E$  and  $H$ -fields. The fields near the wire are mainly non-radiating and they are the reactive near fields.

At distances well away from the wire,  $r$  is much larger than  $\lambda$ , and the terms in  $\lambda/r$  can be neglected, giving

$$E_r = E_\phi = H_r = H_\theta = 0 \quad (1.9)$$

$$E_\theta = \sqrt{\frac{\mu}{\epsilon}} \frac{I \cdot l \cdot \sin \theta}{2r\lambda} \cos\left(2\pi \frac{r}{\lambda} - \omega t\right) \quad (1.10)$$

$$H_\phi = \frac{I \cdot l \cdot \sin \theta}{2r\lambda} \cos\left(2\pi \frac{r}{\lambda} - \omega t\right) \quad (1.11)$$

This approximation describes the  $E$  and  $H$ -fields that propagate away from the wire and is therefore referred to as the far field radiation. Note that the magnetic and electric components are mutually perpendicular.

Table 1-1: Frequency Bands Designation and Their Wavelength

Designation	Frequency	Wavelength
Very low frequency (VLF)	3 – 30 kHz	100 – 10 km
Low frequency (LF)	30 – 300 kHz	10 – 1 km
Medium frequency (MF)	0.3 – 3 MHz	1 – 0.1 km
High frequency (HF)	3 – 30 MHz	100 – 10 m
Very high frequency (VHF)	30 – 300 MHz	10 – 1 m
Ultra high frequency (UHF)	0.3 – 3 GHz	1 – 0.1 m
Super high frequency (SHF)	3 – 30 GHz	100 – 10 mm
Extremely high frequency	30 – 300 GHz	10 – 1 mm

For antennas whose sizes are comparable to the wavelength, the approximate boundary between the far-field and the near-field region is commonly given as  $r = 2*D^2/\lambda$ , where  $D$  is the maximum antenna dimension and  $\lambda$  is the wavelength. For electrically small antennas, the radiating near-field region is small and the boundary between the far-field and the near-field regions is commonly given as  $r = \lambda/2\pi$ . Table 1-1 shows the wavelength of different frequency bands. For biomedical implants with coupling frequency under 30 MHz, it can be assumed that the EM fields are under near field operations.

When there is a receiver located in the near field of the transmitter antenna, the coupling between the two items affects both impedances of the transmitter and the receiver as well as the field distribution around them. The equivalent antenna performance parameters (i.e., gain and impedance) can no longer be specified independently of each other and become position and orientation-dependent. The near field of a transmitter antenna can have

several tangential and radial electric and magnetic field components which can all contribute to coupling. Two fundamental cases are magnetic (inductive) coupling and electric (capacitive) coupling.

### 1.3 Inductive Coupling and Capacitive Coupling

The coupling mechanism in near-field transmission can be either magnetic (inductive) or electric (capacitive). Depending on the environment, the field distribution can be affected by the presence of various objects. Inductively coupled systems where most reactive energy is stored in the magnetic field, are mostly affected by objects with high magnetic permeability. For power transfer through the skin layer, the magnetic permeability of biological tissue is practically equal to the magnetic permeability of air,  $\mu_0$ . There is no significant difference in the magnetic flux distribution when the medium is changed.

The capacitance of a device with two metallic plates of area  $A$ , with separation  $d$ , and the gap filled with material of relative permittivity  $\epsilon_r$  is given by

$$C = \frac{\epsilon \cdot \epsilon_r \cdot A}{d} \quad (1.12)$$

For capacitively coupling systems where most of the reactive energy is stored in electric field, they are affected by objects of high dielectric permittivity. Since the body has much higher permittivity (e.g., the  $\epsilon_r$  for skin is 120 at 13.56 MHz, and it is 47 at 433 MHz [4]), relatively speaking, inductive coupling is much more efficient for transcutaneous power transfer. However, in some previous research works [5], experiments were carried out to study capacitive coupling for power transfer and data telemetry with positive results.

### 1.4 Literature Review

In this section, only transcutaneous energy transmission systems (TETS) for artificial hearts or TETS with high power rating (over 10 W) are considered. Other transcutaneous powering systems/methods that are targeted for low-power biomedical devices will not be discussed in this thesis.

#### 1.4.1 TET System Development

The development of the TET system was started by J.C. Schuder's group in the 1960s [6-11]. In July 1960, some months after the announcement that dogs can be kept alive for 3 and 5 hours with implanted hearts, a team was formed at the University of Missouri-

Columbia to study the ways to transport energy into the body without piercing the skin. They had developed the theoretical background for a radio frequency system involving inductive coupling between a thin. The device included a small pancake-shaped coil on the surface of the chest and another coil subcutaneously within the chest. The theoretical transfer efficiency is about 95%. Transformer coils of different sizes were built, and they were tested at different separation distances [6]. This was the birth of the transcutaneous energy transformer (TET). Results of the experiments showed that a larger transformer coupling coefficient,  $k$ , was obtained when a larger coil set was used, and the coupling coefficient decreased rapidly with the separation distance. At the same time, experimental evaluations were done in dogs at 50 and 69 W levels. An ac source was used to drive the external coil, the internal coil was coupled with a resonant capacitor and the working frequency is 400 kHz. There is no exact figure of power efficiency, but when the secondary output was driving a mechanical rotary pump, the overall efficiency from the battery to shaft was 16.2%.

Extensive works were done by the group continuously on transcutaneous energy transfer. They had studied the use of ferrite core to increase the transformer coupling effect. The efficiency of electromagnetic energy transport between an external coil and an implanted coil within the body can be appreciably increased by the utilization of a suitable ferrite core [7]. This fact can be viewed as the increase of flux concentration by the ferrite core that increases the coupling coefficient between the TET coils. Other experiments were done to study the effect of long-term exposure to the electromagnetic field for living dogs and mice. The results suggested that it may be possible to transport large amounts of electromagnetic energy into the body without long-term adverse effects on the organism [9]. The group also did experiments on the transmission of 1 kilowatt of power to a living dog [10]. During one hour of experiment, the temperature of the internal coil rose from 98°F to 103 °F. The temperature rise was equivalent to a power loss of 5.2 W, which was closed to theoretical prediction.

The experiments done by Schuder's group were using a high frequency ac power amplifier to drive the TET primary. A more practical circuit was suggested in [12] that can be operated from a battery supply. This device was basically a transistor square wave generation circuit, together with a full bridge for driving the transformer primary. More transcutaneous power transformers were built subsequently [14, 16].

Although there were more research interests for the transcutaneous energy transfer for artificial hearts, there were no practical systems in use. According to a report in 1975 [18], almost all artificial heart projects at that time were using nuclear engine [13, 17] as the power source. Only the Jarvik electro-hydraulic heart system developed by the University of Utah attempted to use the inductive coupling techniques.

More practical results were obtained by Sherman's team [20]. A TET system was built and in vivo evaluations were done in 9 Pitmann Moore miniature pigs. The system transmitted approximately 25 W through the animal when switched on. The on and off times were adjusted such that approximately 12 W mean power was transmitted. After 149 days of live testing, the surrounding tissues around the TET system were found normal. The results strongly indicate that animal tissues are well tolerated of the implanted coils for toxicity, heat, impaired perfusion or exposure to high frequency electric and magnetic fields.

Other successful experiments were done at the Pennsylvania State University [23, 26, 47] and at the Oita University [24]. In [47], the peak efficiency of their TET system had been increased to 87%.

Starting from 1990, TET systems with adaptive frequency tuning started to appear. Ghalary and Cho [34, 63] modelled the transcutaneous converter as a series resonant converter. In this converter, large leakage inductances of the transformer were incorporated into the resonant inductor. Analysis of the full-bridge, zero-voltage-switched series resonant converter was presented, and a design procedure was given. The design can accommodate output loading variation as well as variation in air gap separation. The theoretical analysis was verified by an experimental converter which transferred 12-48 W through an air gap of 1-2 cm. In addition, the small-signal behaviour of the converter was predicted and compared with experimental measurements. Finally, a control loop was designed that ensured stability and optimum regulator performance. However, in the research, the feedback control circuitry was hard-wired.

While Ghalary's control circuitry used resonant circuit only at the secondary side of the transformer, Cho and his students proposed a double tuned duty cycle control circuit for transcutaneous energy transmission [64]. A constant frequency duty cycle control method was proposed. In this method, the ON-time of the switches in the primary bridge was controlled to generate a quasi-square wave and the operating frequency was fixed near the resonant frequency in order to maximize the effect of resonance. The output voltage was controlled by the duty cycle of the primary switches.

The control circuit was further improved in [65] with compensation of the leakage inductances on both sides of the transcutaneous transformer. By minimizing the circulating current of the magnetizing inductance, enforcing zero-voltage switching (ZVS) of the primary switches, and zero-current switching (ZCS) of the secondary rectifier diodes, the efficiency can be significantly improved, especially at the secondary side. The power efficiency ranged from 65% to 80%, with  $k_{\min}$  the best and  $k_{\max}$  the worst. Only frequency control was used, and there was no PWM control.

At the same time, Zierhofer [31] proposed to use a class E tuned power oscillator for transcutaneous power and data transmission. The idea was to combine class E amplifier with a tuned inductive link. In addition, the class E amplifier was self oscillating. Oscillation frequency was not fixed, but influenced by the mutual position of the coils. This self oscillating final stage has two basic advantages over a driven RF amplifier. First, no oscillator is necessary for generating an RF voltage, thus avoiding additional power losses. Second, oscillation frequency offset due to coupling variations significantly improves power transmission performance since the resulting oscillation frequency tracks the absolute transmission efficiency maximum. The system was tested with coil distance up to 8 mm, and the overall efficiency varied between 60% and 70%.

The class E circuit was first invented by N.O. Sokal and A.D. Sokal [28] in 1975. It is a very good power driving circuit for loosely coupled transformers, especially at high frequency. Only single transistor is needed in the driving circuit and the switching loss is minimal. The class E circuit was further studied by other researchers [29-30]. It is the basic driving circuit for RFID devices and most of the low power (below 1 W) implanted devices use class E driver for power transmission. However, in order to achieve the lossless switching conditions, operating frequency has to be controlled to a limited range. When the coupling coefficient  $k$  is changing, it is difficult to adjust the frequency correctly.

Troyk [37] described another class-E control method with “high-Q approximation” which simplified the design procedures. A closed-loop controller was designed to compensate for transmitter and receiver variations, and a method of data modulation using synchronous frequency shifting was described. Other class-E driver designs were reported in [40, 54]. Another novel converter [42] was developed in Japan, which was based on a tuned-circuit oscillator operating at class C condition.

Mussivand’s group [41, 44] at the University of Ottawa had developed another TET system with auto-tuned function. The same system was also in used at the University of Utah. The design was very popular, and many artificial heart researches have also adapted this functional design. Details of the design can be found in [41]. A resonant capacitor  $C_p$  was placed in parallel with the transformer primary and another capacitor  $C_s$  was placed serially with the transformer secondary. The secondary resonant frequency was approximately one half the resonant frequency of the primary coil. This resulted in a dual resonant design. Because the coils were tuned to distinctly different frequencies, there was no need to precisely control the resonant frequencies to ensure effective power transfer. The current flowing in the primary coil had two components, one attributable to the resonant current of the primary coil and the other attributable to the reflected load current from the secondary coil. The condition of secondary resonance can be detected by comparing the phase

relationship between the voltage and current in the primary coil. The system was able to deliver maximum output power of approximately 60 W at a coil separation of 5 mm, falling to approximately 45 W at a coil separation of 15 mm. The system can deliver a maximum efficiency of 75-80%, reducing to approximately 60% at 60 W. The operating frequency ranged from 510 kHz to 420 kHz. In a later design, the switching frequency was increased to 1 MHz.

Phillips [45] proposed another high capacity transcutaneous energy transmission system, where the DC/DC converter was a boost converter with a constant frequency control circuit. This circuit provided a constant DC voltage of 20-40V to the following stage. The DC/RF converter was a half-bridge circuit with two N-channel power MOSFETs operating at a frequency of 1.0 MHz. The primary circuit was tuned to an operating frequency above the resonance frequency. A maximum efficiency of 77% was measured with a resistive load.

Matsuki *et al.* [48, 49] from Tohoku University (Japan) developed two circuits for secondary side rectification: (i) a push-pull type of synchronous rectifier; (ii) a voltage doubler type of synchronous rectifier. The temperature rise of the rectifying circuits can be reduced to 30-50% of that of the conventional Schottky diode bridge circuit. In [58, 60], the synchronous rectifier system was further improved by using digital PLL technique to provide appropriate turnoff timing and prevents the system from shoot through conditions. As a result, the resonant capacitor  $C$  and the smoothing inductor  $L$  were eliminated from the secondary side circuit.

Okamoto *et al.* [61] introduced a new structure in the energy coil pairs. A small size energy-receiving coil was used which had an outer diameter of 53 mm. There was a ferrite core of 38 mm diameter. The air-core energy transmission coil had an outer diameter of 92 mm and an internal diameter of 70 mm. In power transfer operation, the receiving coil together with the skin layer will be completely fitted into the center region of the energy transmission coil, producing a self-aligned mechanical construction for best coupling.

In recent years, the controller design of the TET system has become more complicated, and some of them have employed FPGA or ASIC to construct the hardware systems [69, 73, 76, 79].

Si *et al.* [68] presented a method to regulate the power transfer over a wireless link by adjusting the resonant operating frequency of the primary converter. A switched-capacitor method of varying the effective resonant capacitance of the primary power converter was proposed and developed. The relationship between the output power delivered and the primary operating frequency was derived, and a phase control method was used to change the operating frequency of the push-pull resonant converter while satisfying the soft

switching conditions fully. The idea of using switched capacitors to control the switching frequency is novel, but the overall design is not effective because it assumes that the coupling coefficient  $k$  is fixed and it requires a reference voltage that is derived from the output voltage.

In [69], Li *et al.* presented a new FPGA controlled high frequency converter for contactless power transfer. The converter is based on full bridge discontinuous energy injection and free oscillation of a series tuned resonant circuit. By taking the advantage of the fast response rate of FPGA circuit, a variable frequency controller was developed to achieve accurate ZCS operation of the switches. The primary side current waveform is monitored and the zero current crossing position (in time) was detected for switching frequency control. For output power control, the peak level of the primary current is compared with a reference level, and the system is switched between the energy injection mode and free oscillation mode according to the result of comparison.

The design by Dissanayake *et al.* [70-71] was based on the design proposed in [68] (all are from University of Auckland), but the secondary side output voltage was obtained from 2.4 GHz RF communication channel (nRF24E1 Nordic transceivers) and experiments were done with real animal, the sheep. The maximum surface temperature of the secondary coil was increased by a mean value of  $3.4 \pm 0.4^\circ\text{C}$  and the mean temperature rise for 20 mm gap separation was  $0.8 \pm 0.1^\circ\text{C}$ . The efficiency of the system exceeded 80% across a wide range of coil orientations.

Thrimawithana and Madawala [77] presented a new primary side control technique for IPT (inductive power transfer). In order to regulate the load voltage, the track current was controlled by accurately estimating the mutual coupling and output voltage through the variation of reflected primary voltage. The proposed circuit is basically a double-tuned parallel-parallel resonant circuit with an additional  $L_1$  inductor at the primary. With some mathematical manipulations it was shown that the secondary side voltage can be determined by the real part of  $V_{C_1}$  where  $C_1$  is the primary side resonant capacitor. Experimental data were obtained to calculate the  $\text{Re}[V_{C_1}]$  output power values and the results matched with theoretical estimated values. However, no real system was built using the new design idea.

Another contactless energy transfer system using FPGA was developed by Moradewicz and Kazmierkowski [76]. The system produced 3 kW high powers and the designed resonant frequency was 60 kHz. There may be variation in magnetic coupling and the resonant frequency may change. The circuit is a series-series double-tuned resonant converter and the IGBT switching devices are operating under ZCS conditions. The FPGA control circuitry is simple. For an  $N$ -period cycle time sequence, the peak value of primary

current within this period is compared with the previously saved value. If the new peak primary current is larger than the previously saved value, then the switching frequency is adjusted in the same direction as the last frequency adjustment. On the other hand, if the peak primary current is smaller, then the frequency adjustment will be in the reverse direction. There is also hardware circuitry that ensures ZCS conditions for the IGBT devices. The design is effective but there is limitation on the output loading range. For light load condition where  $R_L$  is large, the  $G_v$  voltage gain will not have a peak within the operating regions of the frequency range. Under this condition, there will be no current peak for the proper operation of the FPGA circuitry.

A TET power regulator was proposed by Chen *et al.* [72], which is also a double-tuned resonant converter in series-series topology. Both switching frequency and duty ratio control were used in the regulation of the secondary output voltage. The switching frequency was adjusted by PLL technique to ensure ZVS conditions of the MOSFET drivers. The resulting switching frequency was above the resonant frequency but close to the resonant point for best power efficiency. Output voltage regulation was handled by a UCC3895 phase-shift full-bridge PWM controller. It is assumed that a circuitry for  $V_O$  voltage feedback remotely from the secondary side was used.

#### **1.4.2 Secondary Voltage Feedback and Data Telemetry**

At the beginning, research in TET systems was focused on the power link setup and the efficiency improvement, and there were no provisions for voltage feedback or data telemetry. But since the human body is a complicated biological system, it is necessary to monitor or record the internal status when the artificial heart is in operation, so data telemetry has become an important issue. There are many ways of information transmission from within the human body to the outside world:

- *Opto/light coupling* [27, 30, 39, 44, 80-87]: In the early designs, photo-couplers were used to transmit information from the secondary side to the primary side. For analog signal transmission, frequency modulation through V/F converter and demodulation by F/V converter will be used to improve S/N ratio. For digital data transmission, serial data in RS232 format will be transmitted with light in 'on'/'off' state as data bit. For newer systems, the light source will come from higher power LED diodes or laser diodes. These devices can generate high intensity light source and high data transmission rate can be achieved. Optical telemetry is attractive because it is not influenced by electromagnetic interference (EMI) and has sufficient transmitting ability.

However, this ability decreases rapidly with skin thickness and with relative dislocations between the luminous element and the receiving element. Another problem with optical coupling is the alignment between the light source and the receiver.

- *Magnetic coupling associated with the power transmission coils* [33, 49, 88-91]: Another set of signal coils will be attached to the primary and secondary sides of the transcutaneous transformer. Since the magnetic path has been created by the transcutaneous transformer, there is no alignment problem. In order to reduce the switching noise from the power transformer, different wiring topology will be used for the signal coils. Also, the frequency band for data signal transmission is much higher than the switching frequency band such that the switching noises can be filtered out in an easier way.
- *RF radio link* [92-99]: With the popular use of RFID technology (and availability of chip set solutions) and the low-power consumption (in  $\mu\text{W}$ ), the use of RF link for implanted devices data telemetry is becoming more and more popular. Table I (from [97]) summarizes the monitoring and control system configurations of some well known artificial heart systems (in year 2005). Out of the seven systems, three of them do not have telemetry functions. One system uses infrared for data communication, and the remaining three systems use RF link. It can be seen that RF data link is a favourable choice. An added advantage of using RF data link is that no physical (surface-of-the-skin) contact between the patient and the controller is required. A communication distance around 2 m or less is sufficient for good data reception. More information on RF frequency usage is given in the paragraphs below.
- *Load-Shift Keying (LSK)* [100-103]: The load-shift keying is based on a property of inductive coupler (i.e., the transcutaneous transformer), in which a change in the secondary load is reflected onto the primary as impedance change. Usually digital data are transmitted as '0'/'1' data patterns with the 'on'/'off' control of a switch at the secondary side. The data carrier is the same as the switching frequency and the data bit rate will be set to a fraction of the switching frequency. This technique is commonly in use with class E power converter circuits. Data can only be transmitted from the secondary side to the primary side. Thus, it is just a back telemetry implementation.
- *Intra-body communication* [104-111]: Using the human body as the transmission medium enables wireless communication without transmitting radio waves through the air. The idea of intra-body communication was first proposed by Zimmerman [104], who adopted electrostatic coupling of low frequency signals. However, the method is susceptible to the conditions of the surrounding environment such as the earth ground

for the return path. There is another type of intra-body communication. The human body is being treated as a waveguide, with high-frequency electromagnetic waves generated at a terminal propagating through the body, and received by another terminal. For ease of attachment, usually the communication receiver is connected to the patient's wrist.

Although data telemetry becomes an important issue for artificial heart systems, very few systems include the feedback of real-time output voltage in their designs. This is because there are backup batteries at the secondary side of the system that serve as energy buffer when input power is low. Also, the coupled voltage delivered to the secondary will seldom be used directly by the implanted hardware circuits, and there will be another level of voltage down conversion. However, a regulated secondary output voltage can ensure that the internal circuits are all operating at their best design conditions so that the power efficiency can be optimized and the heat loss generated are minimized.

For information being transmitted through the data link, two infrared (IR) transmitter/receiver modules were used to set up a simultaneous bidirectional communications link with data rate up to a baud rate of 9,600 bps [80]. The following operating parameters were transmitted from the implanted device: operating mode, beat rate, systolic fraction, internal transcutaneous energy transfer (TET) voltage during systole and diastole, the status of the cyclic redundancy checking, and assorted warnings. In addition, data from a blood chamber diaphragm position sensor are also transmitted. This data received at the primary side will be displayed as a waveform on the LCD.

In [89], signals were transmitted using figure-of-eight coils, and five-channel signal transmission in frequency-division multiplex (FDX) was performed. Three waveforms were transmitted that simulated the pump flow rate, blood pressure, and ECG generated from a human body.

Additional information that can be transmitted by the implanted device is given in Table 1-2.

Table 1-2: Throughput Requirement for Medical Sensing Devices [99]

Sensor Type	Throughput (kbps)
SpO <sup>2</sup>	0.01 – 0.1
Glucose	0.01 – 0.1
Blood pressure	0.01 - 10
ECG	10 - 100 (12-bit, 300 Hz, ×20)
EEG	10 - 200 (6 kbps, ×32)
EMG	10 - 1500 (16-bit, 8 kHz, ×12)

Furthermore, in the RF data link, there are regulations on the use of frequency band for radio communication. Frequency bands that can legally be used by a medical telemetry device are limited to the Medical Implants Communication Service (MICS) band (402 – 405 MHz) and the Industrial, Scientific and Medical bands (ISM): 902 – 928 MHz, 2.4 – 2.4835 GHz, and 5.725 – 5.825 GHz. The ISM bands are open to the public while the MICS band is for medical devices.

Wireless medical devices and networks operate in several frequency bands under various national and international rules. The IEEE 802.15 Task Group 6 (body area networks, BAN) has developed a communication standard for low power devices and operation on, in or around the human body (but not limited to humans) to serve a variety of applications including medical, consumer electronics / personal entertainment and others.

### 1.4.3 Secondary Side Battery

There are two types of implantable batteries: primary battery and secondary battery. Primary batteries can only be discharged once and they cannot be recharged. They are mainly used to provide energy for implanted devices with low power consumption. Secondary batteries are designed for repeated charging and discharging, but in practice there is an upper limit on the number of charge/discharge cycles. There is a slow deterioration of battery capacity after each charge/discharge cycle, and the capacity of a typical battery will drop to 80% of its initial specified capacity after 1000 to 2000 cycles.

An implantable secondary battery is one of the key components in an artificial heart system because of safety reasons. It must be driven by an internal secondary battery system in the case of interruption of energy transmission from outside the body. Due to the high power consumption of the artificial heart system, the internal battery can only provide power backup for duration between 15 minutes to one hour. The performance of secondary batteries had been improved dramatically since 1960s because of the development of new materials for electrodes, as well as the research and development of new battery technology. Three kinds of rechargeable batteries are commonly used as secondary battery: Ni-Cd secondary battery, Ni-MH secondary battery, and Li-ion battery [112-117].

Nickel-cadmium (Ni-Cd) was first selected as implantable secondary battery for artificial hearts. Later, nickel-metal hydride (Ni-MH) battery and lithium-ion secondary battery (Li-ion) were available as candidates for selection, as both types of batteries can store more energy than a Ni-Cd secondary battery.

The Ni-Cd secondary battery had been widely used in many electric devices for several decades. Stable operation and reliability are advantages of the Ni-Cd secondary battery, but its high surface temperature, which reaches a temperature of higher than 55°C during a 1 C rapid charge, is a serious drawback. If the Ni-Cd secondary battery were to be used for an implantable battery system, it would have to be charged with a low charge current to prevent temperature rise.

Ni-MH secondary batteries are now widely in used. A Ni-MH battery has higher energy-volume density as that of a Ni-Cd battery, and the discharge characteristics of the Ni-MH secondary battery remain constant until the end of discharge. These characteristics are advantageous for interfacing with an actuator and controller of an artificial heart. On the other hand, the high battery surface temperature (45°C) of the battery in the charge phase and its relatively short cycle life are disadvantages for using the battery in implantable devices in the body. The cycle life of the Ni-MH secondary battery (800 cycles) is not sufficient to supply energy to the artificial heart once or twice a day for a period of more than 2 years.

Li-ion secondary batteries are currently the best energy storage devices for portable computer electronics because of their high energy density. They have been commercially available since the 1990s and have been used in a wide range of products such as notebook computers, cellular phones, and digital video cameras. The Li-ion battery is 1.5 times higher in volume and 1.5 to 2 times higher in weight than that of Ni-Cd secondary battery, whereas the voltage of a Li-ion battery (approximately 3.6 V) is approximately 3 times higher than that of a Ni-Cd secondary battery (1.2 V).

There were no detailed information on the charging mechanism for artificial heart systems, but most likely the charging control is done at the secondary because the terminal voltage of the rechargeable battery can only be sensed at the secondary side. Also, if a battery cell is overcharged, gases will be generated, thus raising the internal pressure and temperature and eventually damaging the cell. In [118, 119], a fast charging circuit for Ni-Cd battery used in implant electronic systems was described. The fast charging control can shorten the charging time from 14-20 hours to 20 minutes. In [123], a highly integrated low power wireless interface with battery charging unit for Li-ion cells was developed in standard CMOS process and an integrated circuit IC was formed.

A DSP controller was used for intelligent Li-ion battery management [120]. The internal battery pack was composed of 7 Li-ion cells of 3.6 V/900 mAh per cell. The terminal voltage of each cell was sensed by the DSP with 8-bit resolution, and charge/discharge control was implemented as DSP based software algorithms.

Detailed implementation of a TET system with rechargeable internal back-up battery for a total artificial heart was described in [121]. Seven lithium-ion rechargeable batteries (3.6 V, 800 mAh per unit cell) were connected in series to obtain an actuator driving voltage of 24 V. The Li-ion batteries were charged with a constant current of 400 mA (0.5C) at a constant voltage of 28.7V to maintain safety. The output of the transformer secondary after rectification is 24 V, and the voltage was raised to 28.7 V by a built-in step-up circuit. The batteries were considered to be fully charged when the charging current is reduced to < 100 mA. During the discharge period, the batteries were assumed to be completely discharged when the sum total of all the terminal voltages drops to < 20 V. The time required for the batteries to be fully charged was from 115 min to 117 min.

Heat generation from an implanted device is a critical issue, and the surface temperature must remain below 42°C to prevent burning of the surrounding tissues. Lithium ion batteries for an implantable LVAD generate heat during the discharge phase, and the surface temperature of the batteries depends on the magnitude of the discharge current.

The temperature of a Li-ion rechargeable battery is determined by ohmic loss due to internal resistance, chemical loss in chemical reaction, and release of heat to the surrounding environment. For a complete system, the surface temperature of the battery box must be monitored and the level of charging current has to be limited to prevent excessive heat generation.

#### 1.4.4 Health Issue: Tissue Heating & EM Fields Radiation

Implanted devices inside the human body will generate waste heat, and if the heat energy cannot be properly removed, the rising temperature will damage the surrounding body tissues. For the removal of heat inside a living body, a study on body temperature elevation by implanted heating devices was performed in [124] with 11 calves. The results showed that the body tissues could adapt to the heating source, leading to an increase of heat dissipation rate over time through angiogenesis (i.e., the growth of new blood vessels from pre-existing vessels). Another study [125] showed that blood perfusion was more efficient than ventilation for heat dissipation.

Waste heat can also be generated from the electronic circuitry and from the operating blood driving pump. Another source of heat generation is the charging of the implanted batteries. In [126, 127], thermal characteristics of Li-ion rechargeable batteries during different phases of the charging process were studied.

Tissue temperature can also be increased through direct absorption of electromagnetic energy. A common measure of absorption is the *specific absorption rate* (SAR). The SAR is expressed in units of energy per unit time per unit mass, or W/kg. It is formally defined as

$$SAR = \frac{d}{dt} \left( \frac{dW}{dm} \right) = \frac{d}{dt} \left( \frac{dW}{\rho dV} \right) \quad (1.13)$$

This description provides a qualitative understanding of SAR, but does not facilitate measurement or calculation. It is more helpful to write the above expressions in terms of either temperature rise, or the material parameters and induced electric field

$$SAR = \left( \frac{dT}{dt} \right) c = \frac{\sigma |E|^2}{\rho} \quad (1.14)$$

where  $c$  is the specific heat of the tissue,  $\sigma$  is the electrical conductivity, and  $\rho$  is the density.

The International Council on Non-Ionizing Radiation Protection (ICNIRP) [128] provides a two-tier set of RF limits. Figures 1 and 2 show the reference levels for exposure to time-varying electric fields and magnetic fields, respectively. The ICNIRP standard is used in most European countries and is gaining acceptance in many countries outside North America, including Hong Kong. The exposure limits from the ICNIRP guidelines for electric fields and magnetic fields are whole-body and time averaged. The higher tier is referred to as “Occupational” while the more restrictive tier is referred to as “General Population”. The limits for the electric and magnetic fields are very similar to the limits in the 1997 FCC Regulations [129]. Table 1-3 shows the SAR limits set by ICNIRP. For the frequency range from 100 kHz – 10 MHz, the localized SAR limit is 10 W/kg for occupational exposure and it is 2 W/kg for the general public.

Some research works [131-132] had been done on the current density and specific absorption rate (SAR) analysis of biological tissue surrounding an air-core transcutaneous transformer for an artificial heart. The results showed that powering an artificial heart system inductively will generate EM fields below the ICNIRP's basic restrictions when the frequency is over 250 kHz and the output voltage is under 24 V. Also, measurement results indicated that different types of biological tissues that maximized the current density are different in terms of the range of frequencies. In the low frequency range, it is the muscle and in the high frequency it is the skin. The boundary is in the vicinity of the frequency 600-1000 kHz [131].

Table 1-3: SAR Limits according to ICNIRP

Table 4. Basic restrictions for time varying electric and magnetic fields for frequencies up to 10 GHz.<sup>a</sup>

Exposure characteristics	Frequency range	Current density for head and trunk (mA m <sup>-2</sup> ) (rms)	Whole-body average SAR (W kg <sup>-1</sup> )	Localized SAR (head and trunk) (W kg <sup>-1</sup> )	Localized SAR (limbs) (W kg <sup>-1</sup> )
Occupational exposure	up to 1 Hz	40	—	—	—
	1–4 Hz	40/ <i>f</i>	—	—	—
	4 Hz–1 kHz	10	—	—	—
	1–100 kHz	<i>f</i> /100	—	—	—
	100 kHz–10 MHz	<i>f</i> /100	0.4	10	20
	10 MHz–10 GHz	—	0.4	10	20
General public exposure	up to 1 Hz	8	—	—	—
	1–4 Hz	8/ <i>f</i>	—	—	—
	4 Hz–1 kHz	2	—	—	—
	1–100 kHz	<i>f</i> /500	—	—	—
	100 kHz–10 MHz	<i>f</i> /500	0.08	2	4
	10 MHz–10 GHz	—	0.08	2	4

<sup>a</sup> Note:

1. *f* is the frequency in hertz.
2. Because of electrical inhomogeneity of the body, current densities should be averaged over a cross-section of 1 cm<sup>2</sup> perpendicular to the current direction.
3. For frequencies up to 100 kHz, peak current density values can be obtained by multiplying the rms value by  $\sqrt{2}$  (~1.414). For pulses of duration  $t_p$  the equivalent frequency to apply in the basic restrictions should be calculated as  $f = 1/(2t_p)$ .
4. For frequencies up to 100 kHz and for pulsed magnetic fields, the maximum current density associated with the pulses can be calculated from the rise/fall times and the maximum rate of change of magnetic flux density. The induced current density can then be compared with the appropriate basic restriction.
5. All SAR values are to be averaged over any 6-min period.
6. Localized SAR averaging mass is any 10 g of contiguous tissue; the maximum SAR so obtained should be the value used for the estimation of exposure.
7. For pulses of duration  $t_p$  the equivalent frequency to apply in the basic restrictions should be calculated as  $f = 1/(2t_p)$ . Additionally, for pulsed exposures in the frequency range 0.3 to 10 GHz and for localized exposure of the head, in order to limit or avoid auditory effects caused by thermoelastic expansion, an additional basic restriction is recommended. This is that the SA should not exceed 10 mJ kg<sup>-1</sup> for workers and 2mJ kg<sup>-1</sup> for the general public, averaged over 10 g tissue.

For the temperature rises due to implantable medical devices, it is governed by ISO-14708-1 [149], a standard from the International Organization for Standardization (ISO). Section 17 (“Protection from harm to the patient caused by heat”) of the document stated that “No outer surface of an implantable part of the active implantable medical device shall be greater than 2 °C above the normal surrounding body temperature of 37 °C when implanted, and when the active implantable medical device is in normal operation or in any single-fault condition”.

## 1.5 Objectives of the Thesis

The main objective of this thesis is to design a power supply for artificial hearts with the following features:

- Power requirement: range from 12 W to 60 W (this is an extended power range that covers the power range of 15 W – 35 W for a normal artificial heart system)
- Transformer gap separation: range from 10 mm to 20 mm (gap width can be changed during normal operation, control system will adapt to the new environment at real time)
- Power efficiency: as high as possible (over 90% for 15 W to 35 W output power)
- Secondary side output voltage is regulated at 24 V. The regulation of output voltage is done by the creation of a data channel using the primary current as carrier. This is a new idea and was proofed as a working solution by real hardware.

There is no rechargeable backup battery in our transcutaneous power regulator design. The backup battery may be added as an extension to the current research project.

## 1.6 Overview of the Thesis

Chapter 1 provides a comprehensive literature review on the development of transcutaneous power regulators for artificial hearts.

Chapter 2 describes the ac modelling of the transcutaneous power converter circuit, and the construction of the SPICE macromodel for fast simulation. The idea of using the same power transformer for secondary voltage transmission is introduced, and the selection of frequency band is described.

In Chapter 3, detailed procedures for designing a DSP-based control system for a transcutaneous power regulator are given. These include components selection, system function descriptions and derivation of design formula.

In Chapter 4, experimental results of the hardware design are presented. Measured values of power efficiency are given, together with a detailed loss analysis.

Finally, Chapter 5 concludes the thesis. The major work and contributions are reiterated. Some suggestions for future research are given.

## Chapter 2 System Modelling

The driving circuit for the transcutaneous power regulator is introduced in this chapter, and the control algorithms for regulating the output voltage and tracking the switching frequency are discussed. Also, the converter transfer function is obtained using a SPICE macromodel, and a control compensation for achieving stable system response is derived.

### 2.1 Transcutaneous Transformer

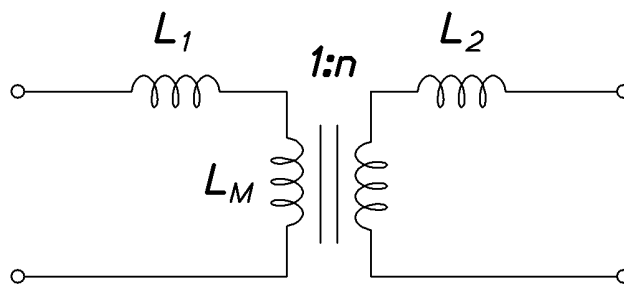


Figure 2-1: Transcutaneous Transformer

In an artificial heart system, the running power is obtained wirelessly through a pair of transcutaneous transformer coils. A transcutaneous transformer is a transformer that works through the skin. There is a skin layer as gap separation between the primary coil and the secondary coil, magnetic flux from the primary side cannot be fully coupled into the secondary side. Electrically, the situation is modelled as leakage inductances in series with an ideal transformer. Figure 2-1 shows the circuit model for the transcutaneous transformer. For the transformer with a turns ratio of  $n$ ,

$$L_p = L_1 + L_M \quad (2.1)$$

$$L_s = L_2 + n^2 L_M \quad (2.2)$$

$$k = nL_M / \sqrt{L_p L_s} \quad (2.3)$$

where  $L_p$  is the primary side inductance,  $L_s$  is the secondary side inductance, and  $L_M$  is the mutual inductance.  $L_1$  is the primary side leakage inductance,  $L_2$  is the secondary side leakage inductance, and  $k$  is the coupling coefficient. The coupling coefficient  $k$  can be regarded as the fractional magnetic flux generated by the transformer primary coil that coupled to the secondary coil. In the ideal case, the value of  $k$  is equal to one. For most practical cases, their coupling coefficients are close to one. For biomedical devices with

inductive power link, however, due to the small size in the coupling coils and the long separation distance, the coupling coefficients are much lower.

For our system, an air-core type transcutaneous transformer was built using AWG46 ( $\times 640$ ) Litz wire. There are 30 turns on the primary side and 29 turns on the secondary side, and the outer diameters are 88 mm and 85 mm, respectively. There is a variation of the value of  $k$  from 0.32 (20 mm) to 0.51 (10 mm) when the gap separation between the transformer coils is changed. Table 2-1 shows the measured parameter values of the transformer at different air gap separations. It can be seen that the coupling coefficient  $k$  decreases with air gap separation, resulting in smaller mutual inductance  $L_M$  and larger leakage inductances  $L_1$  and  $L_2$ .

Table 2-1: Measured parameters for transcutaneous transformer

Air gap	$L_p$ ( $\mu\text{H}$ )	$L_s$ ( $\mu\text{H}$ )	$L_1$ ( $\mu\text{H}$ )	$L_2$ ( $\mu\text{H}$ )	$L_M$ ( $\mu\text{H}$ )	$k$
10 mm	33.29	31.99	16.22	15.99	17.07	0.51
15 mm	33.18	31.90	20.36	20.07	12.82	0.38
20 mm	33.11	31.82	22.30	21.99	10.81	0.32

## 2.2 Topology of Compensation Networks

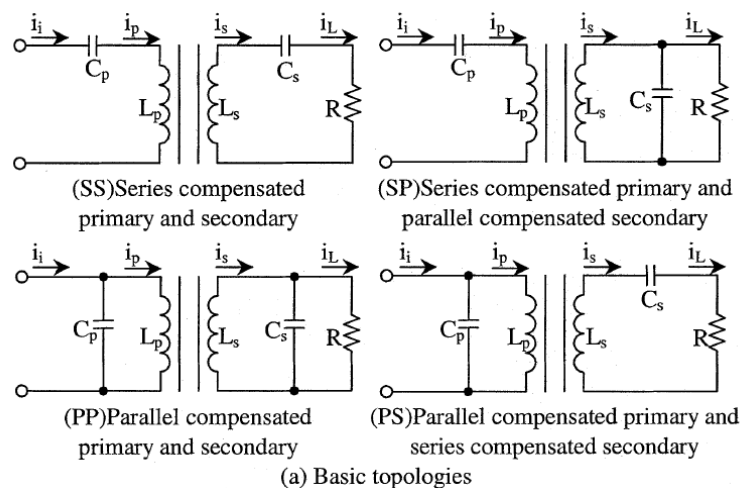


Figure 2-2: Basic topologies for primary and secondary compensation network [66]

The leakage inductances of the transcutaneous transformer can be compensated for by using resonant capacitors placed in series or in parallel to it. The compensation can be done

at both primary and secondary sides, or just only at the primary side or only at the secondary side. From the analytical results given in [67], the series compensation on the primary side is more effective in nullifying the leakage inductance than other single compensation topologies. And the performance of compensating both primary and secondary sides is much better than compensating only one side.

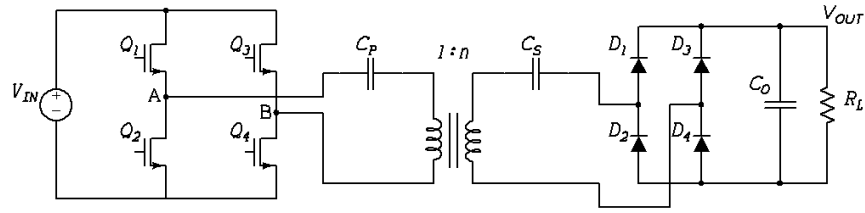
For resonant compensation at both primary and secondary sides, as shown in Figure 2-2, there are four basic topologies: series-series (SS), series-parallel (SP), parallel-series (PS), and parallel-parallel (PP). In the PP and PS topologies, the value of the resonant capacitance is not constant but depends strongly on magnetic coupling and quality factors, which makes frequency control more difficult. However, one advantage of the parallel resonant configuration is that one end of the resonant capacitor is connected to the negative voltage point (or ground point) and it is possible to vary the capacitance value for resonant frequency adjustment. For the SS and SP topologies, experimental results from Moradewicz and Kazmierkowski [76] showed that the efficiency of the system with SP topology is lower than the SS circuit. The efficiency of the SP topology is strongly reduced when the transformer air gap length increases.

For high power systems with large current flow ( $> 100$  A), usually the PP topology is selected for resonant compensation. This is because a series connected capacitor will have large current flowing through it and the resonant voltage is high, thus requiring an expensive capacitor with inevitably short life time.

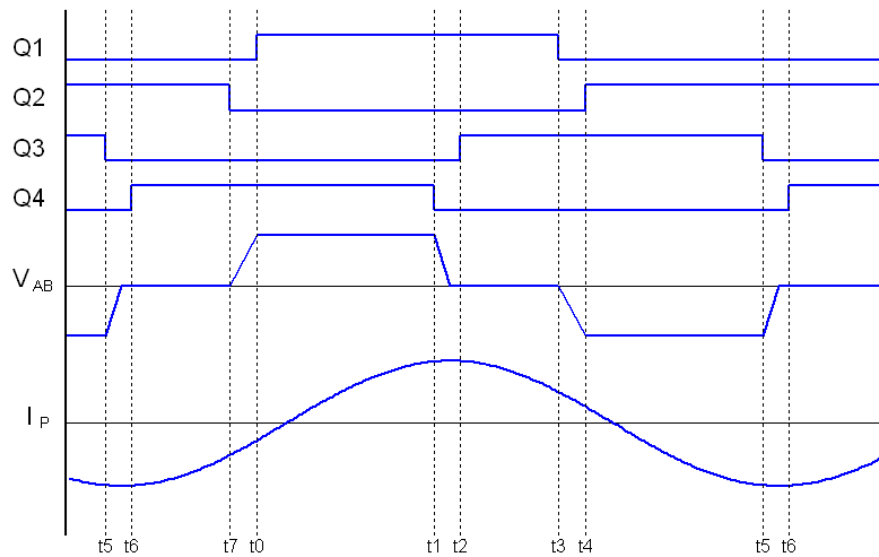
In our transcutaneous power regulator system, the SS topology is used for leakage inductance compensation. An added advantage of the SS topology in our system is that when the air gap separation changes so that the magnetic coupling coefficient  $k$  changes accordingly, but the ratio between the leakage inductances  $L_1$  and  $L_2$  will remain the same as  $L_p/L_s$ . So, the primary and secondary resonant frequencies are in synchronization. When frequency adjustment is made for resonant frequency tuning, both the primary side and the secondary side networks will be tuned to the same resonant point.

Another advantage of series-connected primary compensation is that the  $C_p$  resonant capacitor is acting as a dc blocking capacitor and the transformer can achieve flux balance automatically.

## 2.3 Phase-Shifted Full-Bridge Operations



(a) Circuit diagram



(b) Timing diagram

Figure 2-3: Phase-shifted full-bridge operations

The artificial heart power regulator in our design is actually a phase-shifted (double-tuned) series resonant converter with series compensation capacitors at both primary and secondary sides of the transcutaneous transformer. The primary side driving operation is implemented in a phase-shifted full-bridge circuit. Figure 2-3(a) shows the circuit connection for the phase-shifted full-bridge. The primary and secondary leakage inductances are compensated by series capacitors  $C_P$  and  $C_S$ , respectively. The values of the resonant capacitors in use are  $C_P = 10.99$  nF and  $C_S = 11.09$  nF. By matching the corresponding leakage inductance values for  $L_1$  and  $L_2$ , the resulting resonant frequency ( $f_r$ ) ranges from 321 kHz (20 mm) to 377 kHz (10 mm). At the secondary side, a full-bridge rectifier converts the ac sinusoidal output into a dc level, and the output ripples are filtered out by an output capacitor  $C_O$ .

Each side of the full-bridge is switched on with 50% duty ratio, and the actual control voltage is obtained from the A and B legs. Figure 2-3(b) shows the operations of the phase-shifted full-bridge circuit. Detailed operations at different time phases are discussed as below:

- From  $t_0$  to  $t_1$

At the beginning of  $t_0$ , Q4 has already turned on and  $V_{DS}$  of Q1 is zero. Q1 starts to turn on with ZVS. The primary current  $I_p$  is flowing through Q1,  $C_p$ ,  $L_p$ , and Q4.

- From  $t_1$  to  $t_2$

At time  $t_1$ , Q4 turns off. The stored energy in the primary resonant tank will start to charge the  $C_{OSS}$  of Q4 and discharge the  $C_{OSS}$  of Q3. If the energy in the tank circuit is large enough, voltage at point A will rise to  $V_{IN}$  level. After that, the current  $I_p$  stops flowing through the two  $C_{OSS}$ , it turns on the anti-parallel diode attached to Q3 and  $I_p$  keeps flowing.

- From  $t_2$  to  $t_3$

At  $t_2$ , Q3 starts to turn on.  $I_p$  transfers the current from the anti-parallel diode of Q3 to the MOSFET Q3. The  $I_p$  current will keep flowing through Q1,  $C_p$ ,  $L_p$ , and Q3.

- From  $t_3$  to  $t_4$

At  $t_3$ , Q1 turns off. The stored energy in the primary resonant tank will start to charge the  $C_{OSS}$  of Q1 and discharge the  $C_{OSS}$  of Q2. If the energy in the tank circuit is large enough, voltage at point B will drop to GND level. After that, current  $I_p$  stops flowing through the two  $C_{OSS}$ , but forces its way through the anti-parallel diode attached to Q2.

- From  $t_4$  to  $t_5$

Q1 has already turned on and  $V_{DS}$  of Q2 is zero. Q2 starts to turn on with ZVS. The primary current  $I_p$  is flowing through Q3,  $L_p$ ,  $C_p$ , and Q2.

- From  $t_5$  to  $t_6$

At time  $t_5$ , Q3 turns off. The stored energy in the primary resonant tank will start to charge the  $C_{OSS}$  of Q3 and discharge the  $C_{OSS}$  of Q4. If the energy in the tank circuit is large enough, voltage at point A will drop to GND level. After that, the current  $I_p$  stops flowing through the two  $C_{OSS}$ , but continues its way through the anti-parallel diode attached to Q4.

- From  $t_6$  to  $t_7$

At  $t_6$ , Q4 starts to turn on.  $I_p$  transfers the current from the anti-parallel diode of Q4 to the MOSFET Q4. The  $I_p$  current will keep flowing through Q2,  $C_p$ ,  $L_p$ , and Q4.

- From  $t_7$  to  $t_0$

At time  $t_7$ , Q2 turns off. The stored energy in the primary resonant tank will start to charge the  $C_{OSS}$  of Q2 and discharge the  $C_{OSS}$  of Q1. If the energy in the tank circuit is large enough, voltage at point B will rise to  $V_{IN}$  level. After that, the current  $I_p$  stops flowing through the two  $C_{OSS}$ , but again goes through the anti-parallel diode of Q1.

In order to minimize the turn-on switching loss, the  $V_{DS}$  of Q1, Q2, Q3, and Q4 must be set to zero (or close to zero voltage) at times  $t_0$ ,  $t_4$ ,  $t_2$ , and  $t_6$ , respectively. The condition for this zero voltage switching (ZVS) to occur is that the voltage transition at point A or point B should be completed during the dead time. Taking the transition from  $t_5$  to  $t_6$  as an example, Q3 is turned off and voltage at point B will change from  $V_{IN}$  to GND level. The  $C_{OSS}$  of Q3 will be charged up from zero voltage to the  $V_{IN}$  voltage level. At the same time, the  $C_{OSS}$  of Q4 will be discharged from  $V_{IN}$  to zero voltage. The charging/discharging operations are done by resonant primary current  $I_p$ , and the total charge involved is

$$Q_C = 2 \cdot C_{OSS} \cdot V_{IN} \quad (2.4)$$

Since the switching frequency  $f_s$  is close to the resonant frequency, it is assumed that the primary current  $I_p$  is sinusoidal and

$$I_p = I_m \sin(2\pi f_s t + \phi) \quad (2.5)$$

The total charge from the current  $I_p$  during the dead time period is

$$Q_{I_p} = \int_{t_5}^{t_6} |I_p| dt = \int_{t_5}^{t_6} I_m \sin(2\pi f_s t + \phi) dt = \frac{I_m}{2\pi f_s} |\cos(\phi_{t_6}) - \cos(\phi_{t_5})| \quad (2.6)$$

where  $\phi_{t_5}$  and  $\phi_{t_6}$  are the current phase angles at time  $t_5$  and  $t_6$ , respectively. And

$$\phi_{t_6} - \phi_{t_5} = 2\pi f_s (t_6 - t_5) = 2\pi f_s t_{DT} \quad (2.7)$$

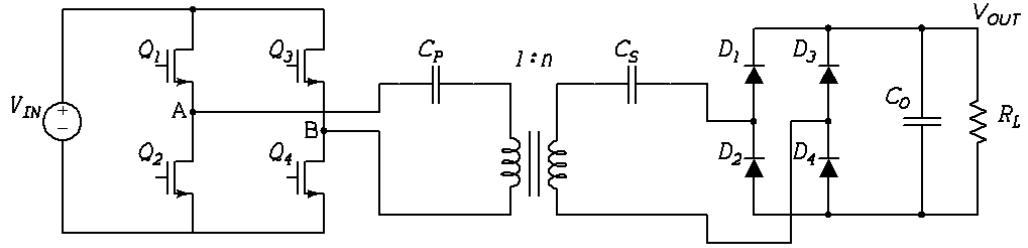
with  $t_{DT}$  is the dead time period. For ZVS condition, the total charge provided by the flow of the primary current must be large enough to charge of the two MOSFET's  $C_{OSS}$  capacitances, i.e.,

$$Q_{I_p} \geq Q_C \quad (2.8)$$

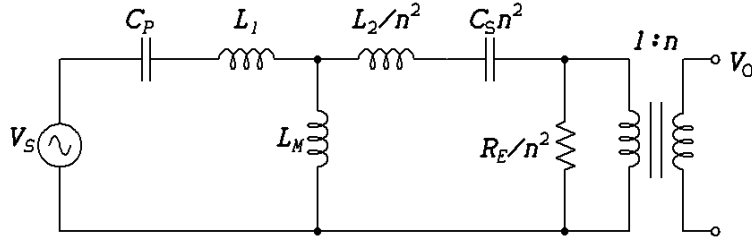
Since the current  $I_p$ 's magnitudes at times  $t_1$ ,  $t_5$  are larger than those at times  $t_3$ ,  $t_7$ , the  $V_{AB}$  transition time for  $C_{OSS}$  charging is shorter.

## 2.4 AC Equivalent Circuit

The circuit of the transcutaneous power supply shown in Figure 2-3(a) is shown again as Figure 2-4(a). Since the switching frequency  $f_s$  of the system is close to the resonant frequency  $f_r$ , the primary inductor current and the secondary inductor current are actually sinusoidal in shape, and the system can be represented by an ac model. Figure 2-4(b) shows the equivalent ac model, with the secondary side circuit network transformed to the primary side. To simplify the ac analysis, all electrical elements are treated as ideal parts.



(a) Circuit diagram



(b) Equivalent circuit

Figure 2-4: Transcutaneous power regulator

From the ac equivalent circuit, the input-to-output transfer function is

$$G_v(\omega) = \frac{j\omega L_M \parallel (Z_S + R_E)/n^2}{Z_P + j\omega L_M \parallel (Z_S + R_E)/n^2} \times \frac{R_E}{Z_S + R_E} \times n \quad (2.9)$$

$$= \frac{j\omega n \cdot L_M \cdot R_E}{Z_P(j\omega n^2 L_M + Z_S + R_E) + j\omega L_M (Z_S + R_E)}$$

where  $Z_P = j(\omega L_1 - 1/\omega C_P)$ ,  $Z_S = j(\omega L_2 - 1/\omega C_S)$ , and  $R_E = 8R_L/\pi^2$ .

In the literature of resonant converters design, the steady-state characteristics for different loading conditions are usually specified by the loaded quality factor  $Q$ , i.e.,

$$Q = \frac{\omega(L_1 + L_2)}{R_E} \quad (2.10)$$

Since in our power regulator system, the leakage inductances  $L_1$  and  $L_2$  vary with the separation distance (i.e., the coupling coefficient  $k$  is changing), the same  $Q$  value may represent different loading conditions. In order to avoid confusion, the true output loading resistances are used as the identification name for the characteristic curves.

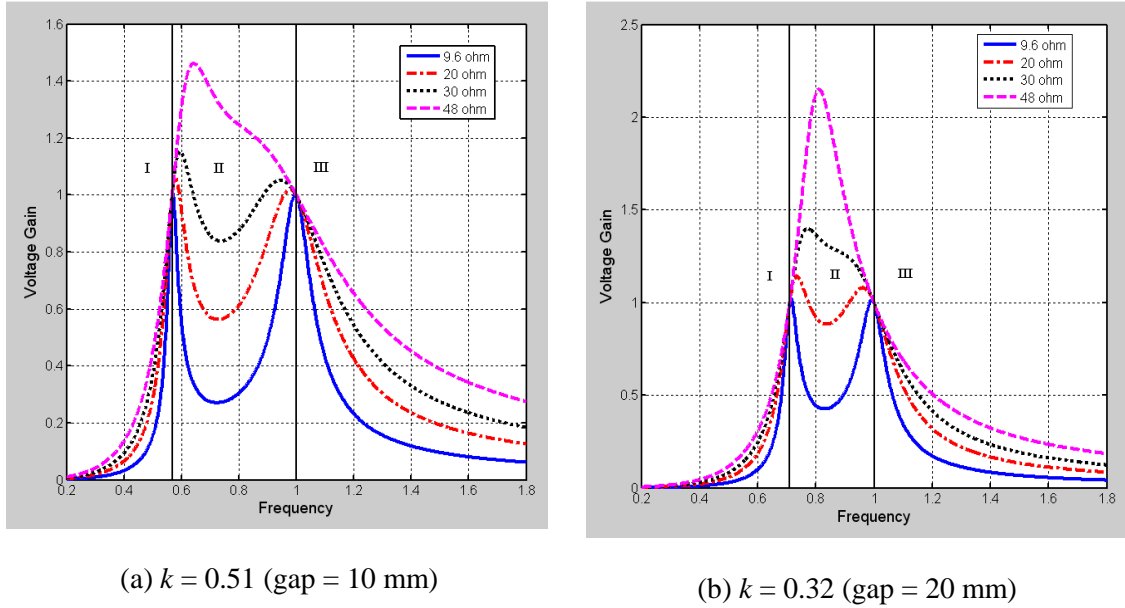


Figure 2-5: Input-to-output voltage transfer ratio

Figure 2-5 shows the input-to-output voltage transfer function for two different values of the coupling coefficient  $k$ , corresponding to a gap separation of 10 mm and 20 mm between the transformer coils. The switching frequency is normalized with the resonant frequency  $f_r$ . The graph can be divided into three regions. Region I covers the range of frequency from the lowest frequency and up to the frequency with unity voltage gain. This region is characterized by the monotonically increasing voltage transfer ratio. Region III covers the range from the resonant frequency  $f_r$  up to the higher frequency range. The voltage gain is unity at the resonant frequency and decreases monotonically with frequency. Region II is the middle frequency region, and the range covered by this region changes with the coupling coefficient  $k$ . This region becomes narrower when  $k$  is smaller. The voltage transfer ratio in Region II varies with the loading condition, which has a large value for light load (large  $R_L$ ) and has valley shape for heavy load (small  $R_L$ ). Using the distance from the region separation frequency for comparison, the gain in Region II is generally higher than those in

Regions I and III, and the higher gain value in Region II is due to the summing effect of the two peaks at the boundary between Region I and between Region III.

For selection of the power converter switching frequency, either Region I or Region III may be considered because of their monotonicity in frequency. Region III is a better choice since the frequency can be set directly proportional to the resonant frequency  $f_r$ . For best power transfer efficiency, the switching frequency should be set close to the resonant frequency. In order to maintain zero-voltage switching (ZVS) condition for the power MOSFET in the full-bridge circuit, the actual switching frequency will be higher than  $f_r$ .

## 2.5 Relationship between Input Voltage and Primary Current

Since the secondary side output voltage of the transcutaneous power supply cannot be directly measured from the primary side, the primary current  $I_p$  becomes an important control parameter for the whole system, both for switching frequency adjustment and for output voltage regulation. It is necessary to have an in-depth understanding of the relationship between the input voltages  $V_{IN}$  or  $V_S$  (in AC analysis) with the primary current  $I_p$  at different loading conditions. The case with full duty ratio where the duty ratio  $D$  is always set to one is studied first, and it is followed by the case with PWM control where the duty ratio  $D$  is controlled to regulate the output voltage at the secondary side.

### 2.5.1 Full Duty Ratio Control

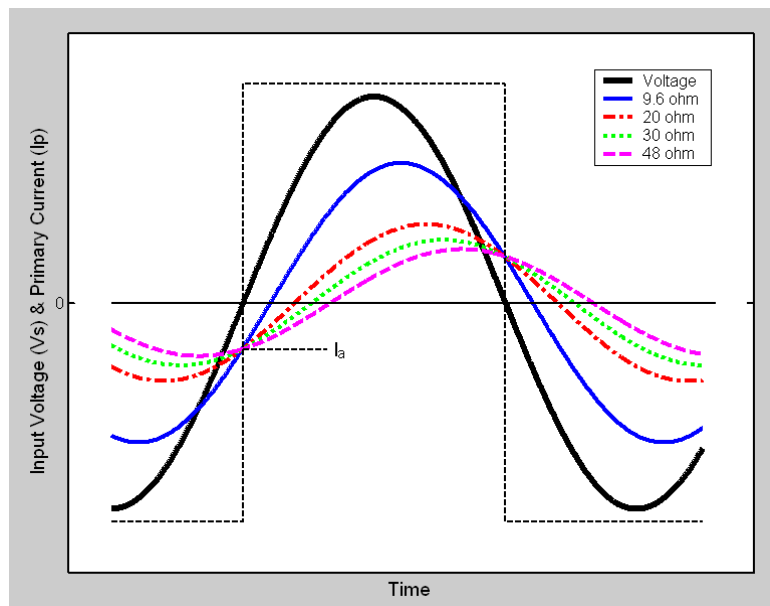


Figure 2-6: Relationship between primary current  $I_p$  and input voltage  $V_S$  at resonant frequency for different loading conditions

Figure 2-6 shows the primary current waveforms for different output loading conditions when the switching frequency  $f_s$  is set to the resonant frequency  $f_r$ . It can be seen that the current waveforms for all loads happen to have the same current level when the input voltage  $V_S$  is zero. At resonance, both  $Z_p$  and  $Z_S$  will be zero and the input impedance is equal to  $j\omega L_M$  in parallel with  $R_E/n^2$ . The primary current is actually the vector sum of two currents,  $I_M$  and  $I_S$ , where  $I_M$  is the magnetizing current and  $I_S$  is the secondary side current reflected to the primary. For resistive load and at resonant frequency,  $I_S$  is in-phase with  $V_S$  and  $I_M$  is  $90^\circ$  out of phase with  $V_S$ . When the sinusoidal input voltage  $V_S$  is at zero level,  $I_S$  is also at zero level and the non-zero level of  $I_P$  current is due to the peak value of  $I_M$  current.

$$I_a = I_{M, pk} = \frac{V_{S, pk}}{|j\omega L_M|} \quad (2.11)$$

The value of  $V_{S, pk}$  is the fundamental component of the square-wave input voltage  $\pm V_{IN}$ , i.e.,

$$V_{S, pk} = \frac{4}{\pi} \cdot V_{IN} \quad (2.12)$$

It can be seen that the current level  $I_a$  is proportional to the input voltage  $V_{IN}$  and  $1/L_M$ , but is independent of the output loading  $R_E$ . This is a very favourable condition for full duty ratio (i.e.,  $D = 1$ ) self-tuning control, and the switching frequency can be adjusted to the resonant frequency by monitoring the  $I_P$  current level.

In order to implement the switching frequency control, it is necessary to know how the  $I_a$  current level changes with frequency  $f$ . First, the input impedance at the primary is

$$Z_{in} = Z_p + j\omega L_M // \left( (Z_S + R_E) / n^2 \right) \quad (2.13)$$

or

$$Z_{in} = |Z_{in}| \angle \theta \quad (2.14)$$

and the current level  $I_a$  can be calculated as

$$I_a = \frac{V_{S, pk}}{|Z_{in}|} \sin(-\theta) = \frac{4}{\pi} \cdot \frac{V_{IN}}{|Z_{in}|} \sin(-\theta) \quad (2.15)$$

Figure 2-7 shows the variation of  $I_a$  when the switching frequency is close to the resonant frequency  $f_r$ . For heavy and medium loading conditions, e.g.,  $R_L = 9.6 \Omega / 20 \Omega / 30 \Omega$ , the current level is changing monotonically so that it is possible to use the current level for resonant frequency tuning. However, for light load condition, e.g.,  $R_L = 48 \Omega$ , the current level is essentially flat and error would be incurred when tuning for resonant frequency.

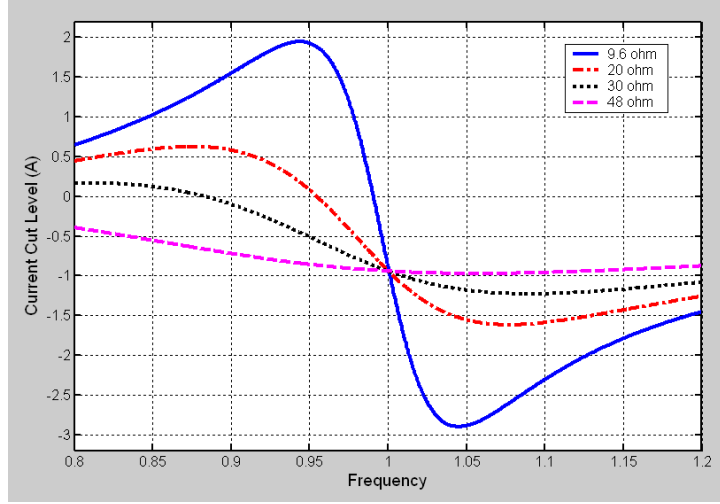


Figure 2-7: Current cut level at different switching frequency ( $V_{IN} = 30$  V, gap = 10 mm, full duty ratio)

## 2.5.2 PWM Control

Next, we consider the case of fixed input voltage and fixed output voltage. For a given input voltage  $V_{IN}$ , when the switching frequency is set to  $f_s$  and with output loading  $R_L$ , it will generate an output voltage  $V_O$ . If the output voltage is higher than the desired output voltage  $V_{OD}$ , under the condition that the switching frequency does not change, then  $V_O$  can be reduced to  $V_{OD}$  by PWM control that adjusts the duty ratio  $D$ .

An output dc voltage of  $V_O$  is equivalent to an output ac signal with peak amplitude of  $V_{O,pk}$ , with relationship given by [133]

$$V_{O,pk} = \sqrt{2} \cdot V_{O,rms} = \frac{4}{\pi} \cdot V_O \quad (2.16)$$

In order to regulate the output voltage  $V_O$  to the desired output voltage  $V_{OD}$ , duty ratio control is applied at the primary side to reduce the effective  $V_{s,pk}$  amplitude, i.e.,

$$V_{s,pk} = \frac{4}{\pi} \cdot V_{IN} \sin\left(\frac{D\pi}{2}\right) \quad (2.17)$$

where  $D$  is the duty ratio with value ranging from 0 to 1. For ideal circuit components, the output voltage is related to the input voltage by the voltage transfer ratio  $G_v(2\pi f_s)$

$$G_v(2\pi f_s) = \frac{V_{O,pk}}{V_{s,pk}} = \frac{\frac{4}{\pi} \cdot V_O}{\frac{4}{\pi} \cdot V_{IN} \sin\left(\frac{D\pi}{2}\right)} = \frac{V_O}{V_{IN} \sin\left(\frac{D\pi}{2}\right)} \quad (2.18)$$

Substituting the value of  $V_O$  with  $V_{OD}$ , the duty ratio  $D$  for a given switching frequency  $f_s$  can be calculated as

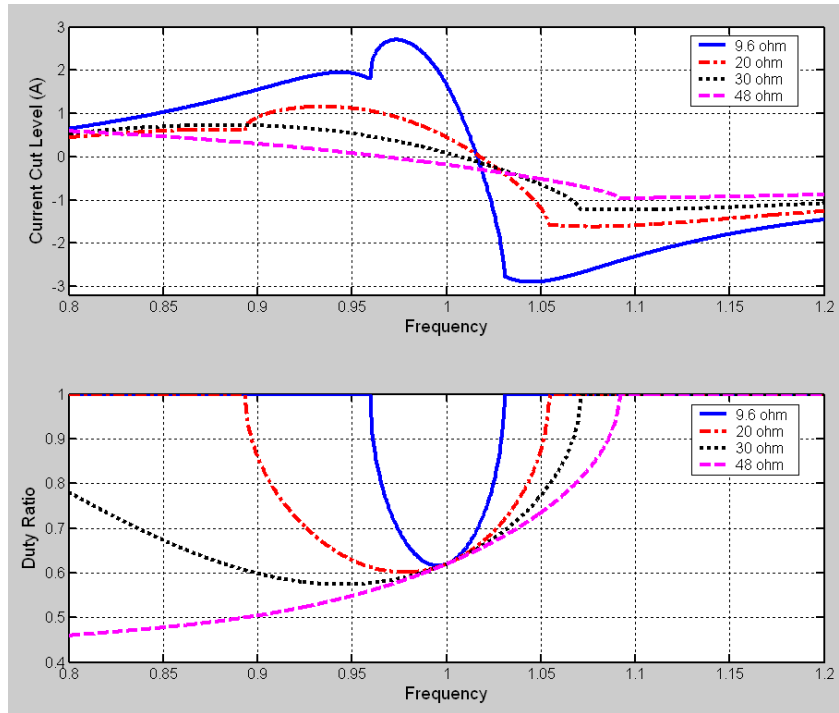
$$D = \frac{2}{\pi} \cdot \sin^{-1} \left( \frac{V_{OD}}{V_{IN} \cdot G_v (2\pi f_s)} \right) \quad (2.19)$$

The effect of non-unity duty ratio generates an additional phase delay between the primary current and the PWM activation signal, the new current cutting level will be

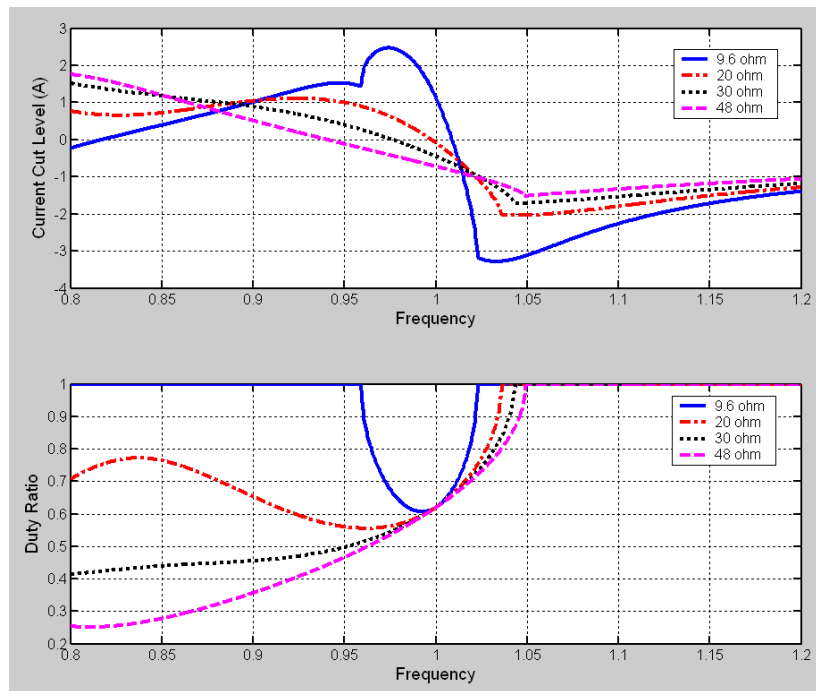
$$I_b = \frac{V_{s,pk}}{|Z_{in}|} \sin \left( \frac{\pi}{2} (1-D) - \angle \theta \right) = \frac{4}{\pi} \cdot \frac{V_{IN}}{|Z_{in}|} \sin \left( \frac{D\pi}{2} \right) \sin \left( \frac{\pi}{2} (1-D) - \angle \theta \right) \quad (2.20)$$

Figure 2-8 shows the current cutting level together with the corresponding duty ratio setting when PWM control is active. Unlike the case with full duty ratio control, these curves under PWM control are better for switching frequency control. Although the curves do not meet at a single point at resonant frequency, the switching frequency can be settled to a frequency above the resonant point with a deviation less than 5%. Such a small deviation is an important criterion for high power coupling efficiency. For full load condition ( $R_L = 9.6 \Omega$ ), the output voltage drops sharply when the switching frequency is away from the resonant frequency. Thus, the switching frequency must be set next to the resonant frequency. On the other hand, there is large variation in the current cutting level, and it is easy to adjust the switching frequency close to the resonant frequency. For light load condition ( $R_L = 48 \Omega$ ), there is a gradual change in the current cutting level (i.e., the current level is not flat) making the control of switching frequency with current level possible. From the graph of Figure 2-8(a), the best current cutting level will be  $-0.3A$ , where the switching frequency will be close together. However, in order to achieve ZVS condition, a lower current level of  $-0.7A$  is chosen and the switching frequency will have larger variation (from  $1.02f_r$  to  $1.07f_r$ ). The graphs in Figure 2-8(b) have similar shape as those in Figure 2-8(a), but the current cutting levels at resonance are larger in magnitude. The larger in current cutting levels is mainly due to a larger magnetization current for smaller  $L_M$  inductance value when the coupling coefficient  $k$  is low. The difference in the primary current level requires adaptive control algorithm that changes the reference current level for different coupling coefficient  $k$ . In actual implementation, the change of  $k$  value is detected by the change in the corresponding resonant frequency  $f_r$  (since the leakage inductances  $L_1$  and  $L_2$  are changed), the reference cut level is gradually changed with the switching frequency.

Adjustment of switching frequency is implemented as phase-locked loop (PLL) frequency tracking control design. The details can be found in Section 3.3.



(a) Coupling coefficient  $k = 0.51$  (gap = 10 mm),  $V_{IN} = 30$  V



(b) Coupling coefficient  $k = 0.32$  (gap = 20 mm),  $V_{IN} = 30$  V

Figure 2-8: Primary current cutting level for different loads

## 2.6 SPICE Macromodel

When the switching frequency is settled, the next step is to retrieve output voltage information from the secondary side and to make sure that the overall control system is stable. For such purposes, a SPICE macromodel is built to generate the system response transfer function. The model is derived from the averaged time-invariant state-space equations obtained from the moving window Fourier Transformation. It allows dc, ac and transient analyses to be carried out at a fast simulation speed. Construction of the SPICE macromodel is based on the technique provided in [134]-[137].

The formulation of the SPICE macromodel is given here, which is based on [134] and [137]. When the power converter is operating close to the resonant frequency  $f_r$ , the inductor currents and capacitor voltages will be sinusoidal in shape. The modulating function or the envelope is assumed to be a slow time-varying function and it can be regarded as constant within one switching period. Based on the above assumptions, the system variables can be transformed to an (almost) time-invariant state-space equation by using the Fourier series

$$x(t) = \sum_{k \in I} \langle x \rangle_k(t) \exp(jk\omega_s t) \quad (2.21)$$

where  $I$  is the set of all integers, and  $\omega_s$  is the switching frequency in rad/s.  $\langle x \rangle_k(t)$ , although strictly a function of time, is assumed to be varying extremely slowly compared to  $\exp(jk\omega_s t)$ , and can therefore be treated as a constant coefficient for the purpose of analysis.  $\langle x \rangle_k(t)$ , also called the  $k$ th coefficient, is determined by

$$\langle x \rangle_k(t) = \frac{1}{T_s} \int_{t-T_s}^t x(\tau) \exp(-jk\omega_s \tau) d\tau \quad (2.22)$$

Similarly,

$$\left\langle \frac{dx(t)}{dt} \right\rangle_k = \frac{1}{T_s} \int_{t-T_s}^t \frac{dx(\tau)}{d\tau} \exp(-jk\omega_s \tau) d\tau$$

Integrating by parts gives

$$\left\langle \frac{dx(t)}{dt} \right\rangle_k = \frac{d}{dt} \langle x(t) \rangle_k + jk\omega_s \langle x(t) \rangle_k \quad (2.23)$$

$\langle x \rangle_k(t)$  is actually a time-varying complex variable, which can be decomposed into the real part and the imaginary part. It is also called phasor representation.

$$\langle x \rangle_k(t) = \langle x \rangle_k^r(t) + j \langle x \rangle_k^i(t) \quad (2.24)$$

Now equation (2.23) can be rewritten as

$$\left\langle \frac{dx(t)}{dt} \right\rangle_k = \left( \frac{d}{dt} \langle x(t) \rangle_k^r - k\omega_s \langle x(t) \rangle_k^i \right) + j \left( \frac{d}{dt} \langle x(t) \rangle_k^i + k\omega_s \langle x(t) \rangle_k^r \right) \quad (2.25)$$

or 
$$\left\langle \frac{dx(t)}{dt} \right\rangle_k^r = \frac{d}{dt} \langle x(t) \rangle_k^r - k\omega_s \langle x(t) \rangle_k^i \quad (2.26)$$

$$\left\langle \frac{dx(t)}{dt} \right\rangle_k^i = \frac{d}{dt} \langle x(t) \rangle_k^i + k\omega_s \langle x(t) \rangle_k^r \quad (2.27)$$

and 
$$\left| \left\langle \frac{dx(t)}{dt} \right\rangle_k \right| = \sqrt{\left| \left\langle \frac{dx(t)}{dt} \right\rangle_k^r \right|^2 + \left| \left\langle \frac{dx(t)}{dt} \right\rangle_k^i \right|^2} \quad (2.28)$$

For a resonant converter operating near the resonant frequency, we may consider only the fundamental frequency term (i.e.,  $k = 1$ ). For a capacitor  $C$ , its voltage and current relationship in phasor representation is

$$\langle i_c \rangle = C \frac{d\langle v_c \rangle}{dt} + j\omega C \langle v_c \rangle \quad (2.29)$$

The phasor representations of the capacitor voltage and current consist of two individual but coupled models as given by

$$\langle i_c \rangle_r = C \frac{d\langle v_c \rangle_r}{dt} - \omega C \langle v_c \rangle_i \quad (2.30)$$

$$\langle i_c \rangle_i = C \frac{d\langle v_c \rangle_i}{dt} + \omega C \langle v_c \rangle_r \quad (2.31)$$

The above two equations can be viewed as a sub-circuit with a capacitor in parallel with a dependent current source.

For an inductor, the voltage across it is proportional to the derivative of the current in the time domain

$$\langle v_L \rangle = L \frac{d\langle i_L \rangle}{dt} + j\omega L \langle i_L \rangle \quad (2.32)$$

or 
$$\langle v_L \rangle_r = L \frac{d\langle i_L \rangle_r}{dt} - \omega L \langle i_L \rangle_i \quad (2.33)$$

$$\langle v_L \rangle_i = L \frac{d\langle i_L \rangle_i}{dt} + \omega L \langle i_L \rangle_r \quad (2.34)$$

The above two equations can be viewed as a sub-circuit with an inductor in series with a dependent voltage source.

For resistor,  $\langle v_R \rangle = R \langle i_R \rangle$ , so

$$\langle v_R \rangle_r = R \langle i_R \rangle_r \quad (2.35)$$

$$\langle v_R \rangle_i = R \langle i_R \rangle_i \quad (2.36)$$

Figure 2-9 shows the phasor transformation for the three basic types of circuit elements: resistor, inductor, and capacitor.

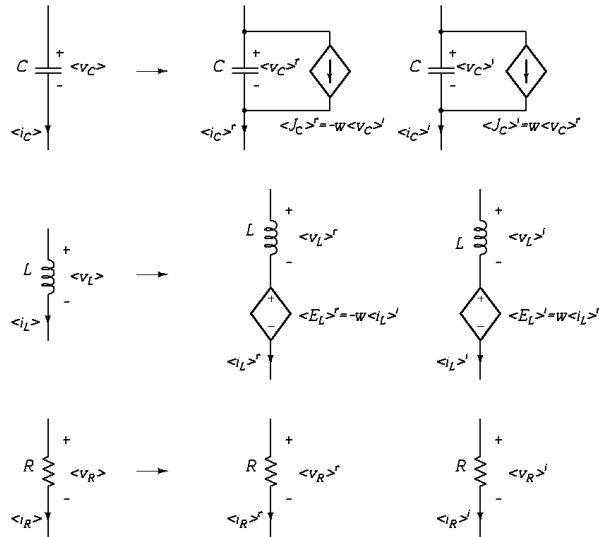


Figure 2-9: SPICE macromodel transformation for  $R$ ,  $L$ ,  $C$  elements

A summary of the procedures for generating the SPICE macromodel from the original resonant circuit is outlined below [135, Pages 4-15]:

1. The circuit is partitioned into two parts: fast switching circuit and slow switching circuit.
2. The fast switching circuit is split into two: the real  $\langle r \rangle$  part and the imaginary  $\langle i \rangle$  part.
3. The driving sources are replaced by their  $k^{\text{th}}$  coefficients in Fourier Transform ( $k = 1$  in our case).
4. In the fast switching circuit, inductance is associated with a dependent series voltage source; and capacitance is associated with a dependent parallel current source.
5. The slow and fast circuits are joined together by the voltage sources parts  $(\langle v_s \rangle, \bar{i}_s)$  and  $(\bar{i}_o, \langle v_o \rangle)$ .

The final SPICE macromodel is shown in Figure 2-10, and the parameter values in the SPICE macromodel are listed in Table 2-2.

Table 2-2: Parameters for SPICE Macromodel

$\langle v_s \rangle^r = 0$	$\langle v_s \rangle^i = -\frac{2}{\pi} V_s$
$\langle v_o \rangle^r = V_o \times \frac{ \langle i_{L2} \rangle^r }{\sqrt{(\langle i_{L2} \rangle^r)^2 + (\langle i_{L2} \rangle^i)^2}}$	$\langle v_o \rangle^i = V_o \times \frac{ \langle i_{L2} \rangle^i }{\sqrt{(\langle i_{L2} \rangle^r)^2 + (\langle i_{L2} \rangle^i)^2}}$
$\langle v_{L1} \rangle^r = \omega_s L_1 \langle i_{L1} \rangle^i$	$\langle v_{L1} \rangle^i = -\omega_s L_1 \langle i_{L1} \rangle^r$
$\langle v_{L2} \rangle^r = \omega_s L_2 \langle i_{L2} \rangle^i$	$\langle v_{L2} \rangle^i = -\omega_s L_2 \langle i_{L2} \rangle^r$
$\langle v_{LM} \rangle^r = \omega_s L_M \langle i_{LM} \rangle^i$	$\langle v_{LM} \rangle^i = -\omega_s L_M \langle i_{LM} \rangle^r$
$\langle i_{CP} \rangle^r = -\omega_s C_P \langle i_{CP} \rangle^i$	$\langle i_{CP} \rangle^i = \omega_s C_P \langle i_{CP} \rangle^r$
$\langle i_{CS} \rangle^r = -\omega_s C_S \langle i_{CS} \rangle^i$	$\langle i_{CS} \rangle^i = \omega_s C_S \langle i_{CS} \rangle^r$

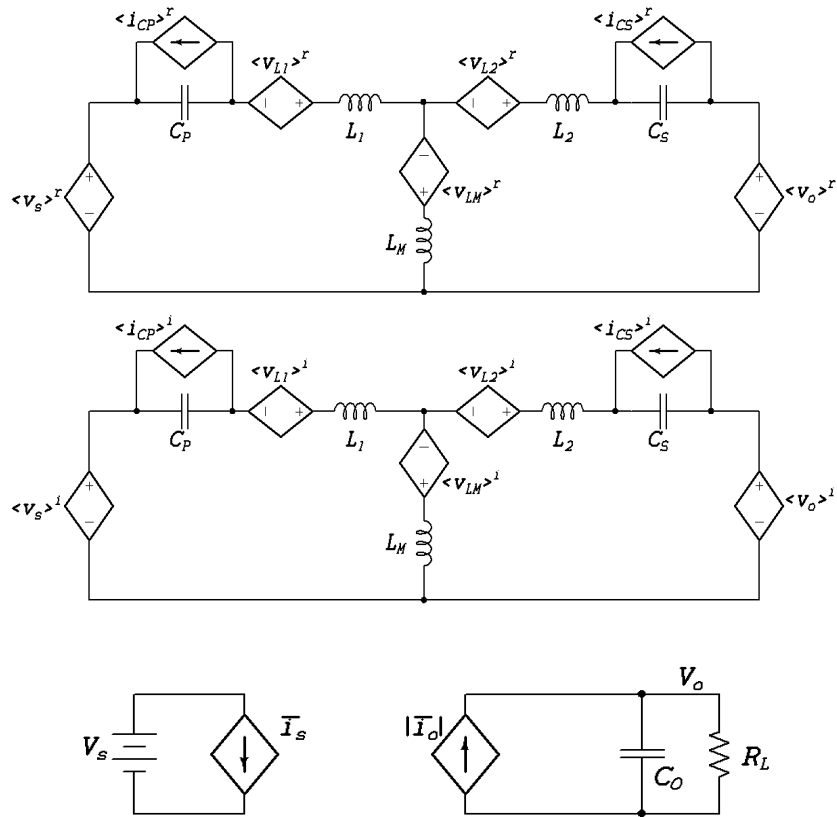
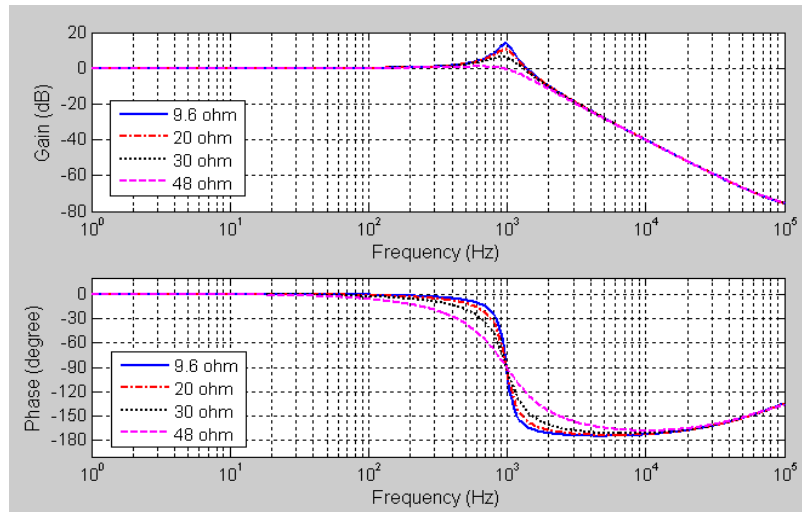
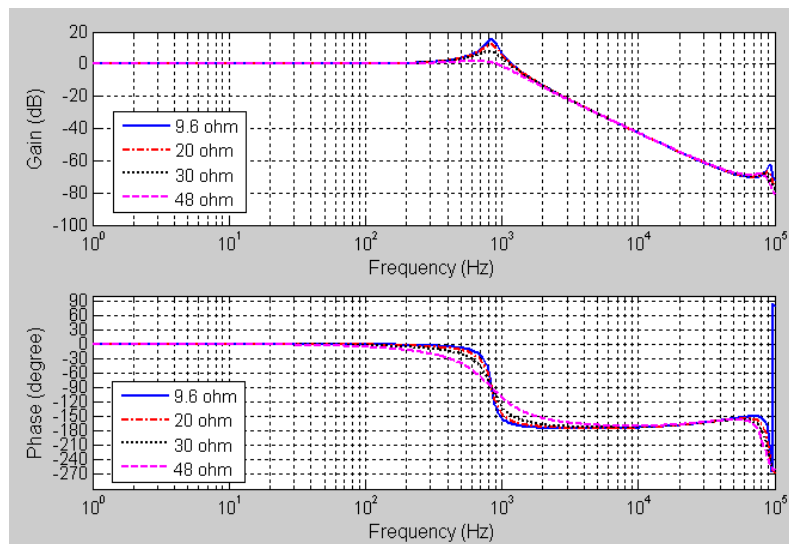


Figure 2-10: SPICE macromodel for circuit simulation

## 2.6.1 Line-to-Output Converter Response



(a) Gap = 10 mm,  $k = 0.51$



(b) Gap = 20 mm,  $k = 0.32$

Figure 2-11: Line-to-output response of TET circuit

By using the SPICE macromodel and applying ac analysis, the line-to-output converter response for two different values of  $k$  are generated, as shown in Figure 2-11. Both the gain and phase response curves are flat from dc to 1 kHz frequency, which indicate neither pole nor zero at dc level. The peaking of magnitude response near 1 kHz frequency followed by a  $-40$  dB/decade region represents a double-pole transfer function, and a phase shift of  $-180^\circ$  in the transition range also indicates the existence of the double poles. There is a high frequency zero near the 100 kHz region, which is shown as the rising of the phase by

90°. The control system can be stabilized under digital control with a PI compensation algorithm. See Section 3.5 for the design of the PI controller.

### 2.6.2 (AC) Output Voltage-to-Primary Current Response

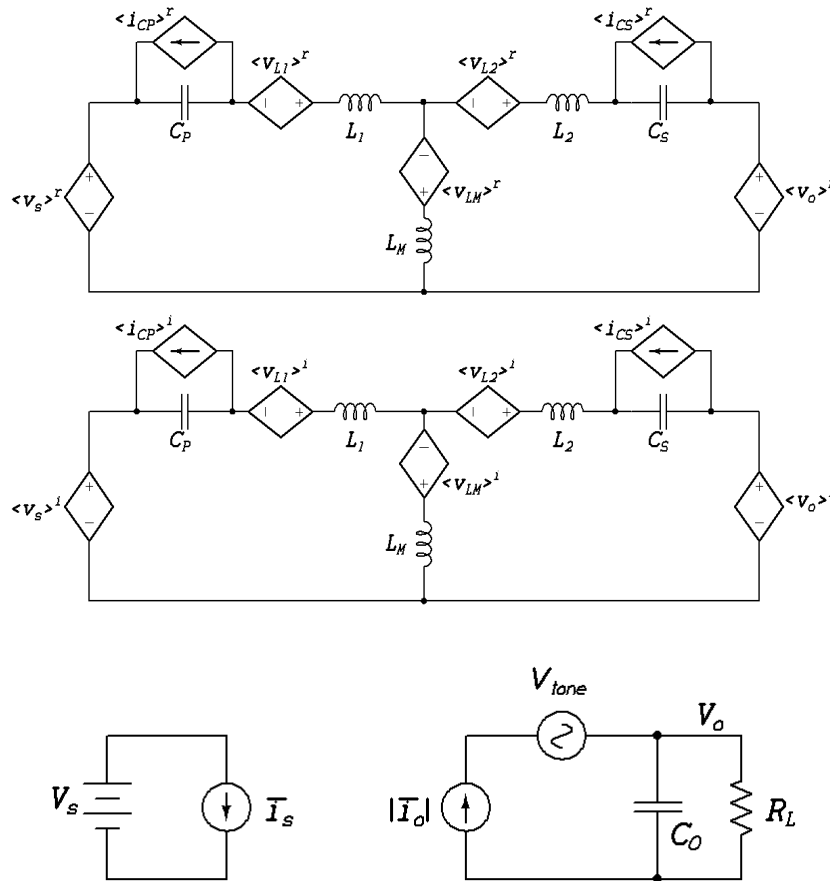
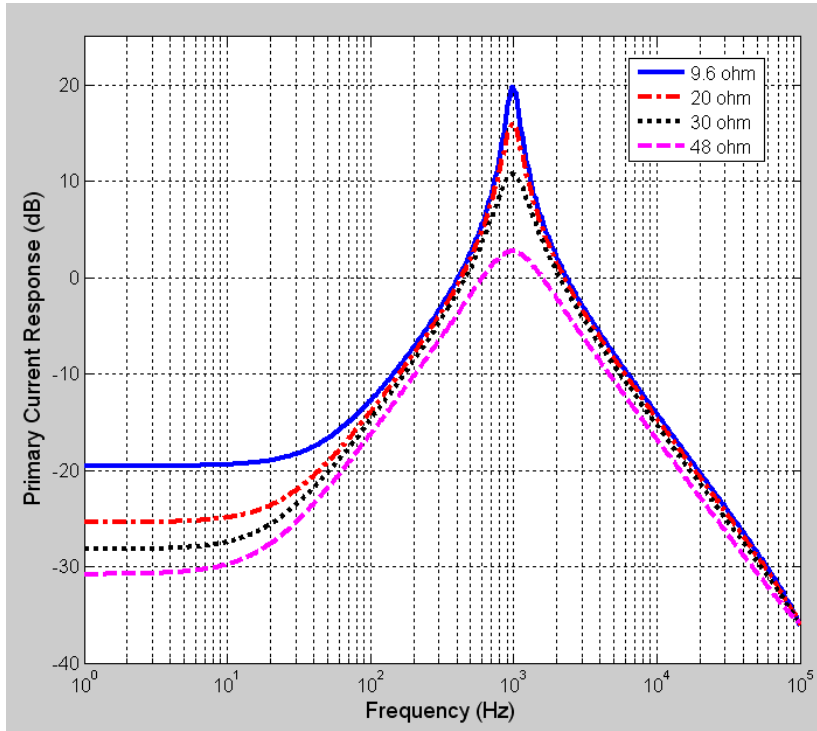
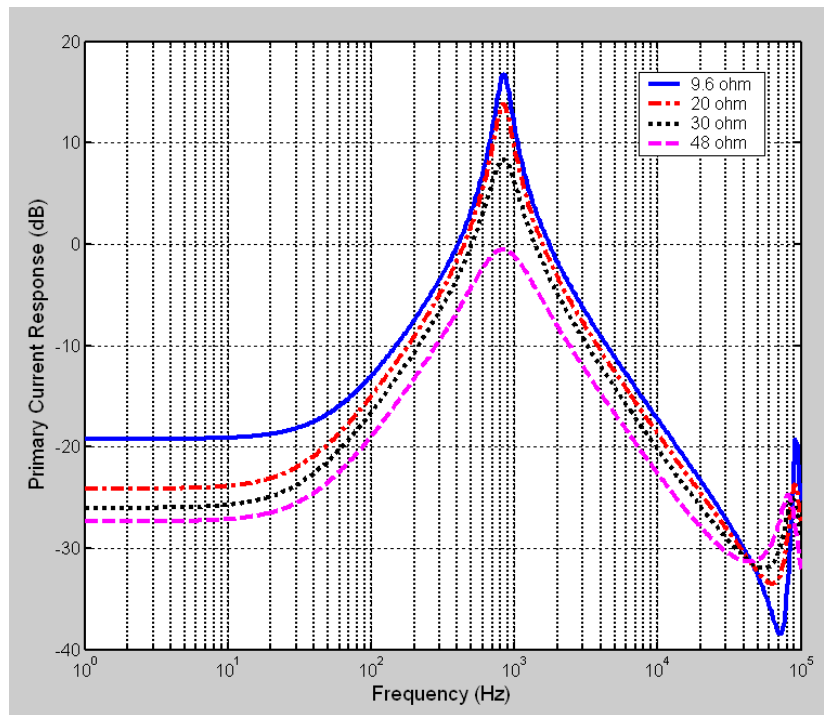


Figure 2-12: SPICE macromodel with ac  $V_{tone}$  at output side

For transmission of information from the secondary side to the primary without using another data link, the solution can be found with a small voltage perturbation at the secondary output. The SPICE macromodel is modified by adding an ac voltage source in series with the output load (Figure 2-12), and the response of the primary current  $\bar{I}_s$  is obtained through ac analysis.



(a)  $V_{IN} = 30 \text{ V}$ ,  $k = 0.51$  (gap = 10 mm)



(b)  $V_{IN} = 30 \text{ V}$ ,  $k = 0.32$  (gap = 20 mm)

Figure 2-13: Frequency response of primary current to secondary tone signal

Figure 2-13 illustrates the primary current response to the ac signal excitation. There is a peaking response at the double-pole position, which should be avoided for data signalling.

The gain response smoothly declines at a rate of 20 dB/decade along both sides of the peak. Similar response curves are obtained for a lower transformer coupling case in Figure 2-12(b). A frequency band range from 20 kHz to 30 kHz is selected for transmission of output voltage information. This frequency band is determined by the geometric mean of the switching frequency (300 – 400 kHz) and the double-pole frequency. With the use of this frequency band, high speed information exchange can be achieved with relatively simple modulation scheme.

# Chapter 3                      System Design

Two hardware prototype boards, namely, the primary side controller board and the secondary side controller board, are built to implement the functions of the transcutaneous power regulator. Detailed design procedures for these two control boards are discussed in this chapter.

## 3.1 Primary Side Controller Board

The main core on the primary side controller board is the CPU, and the first issue in the design process is to select the DSP CPU.

### 3.1.1 Primary Side DSP Functional Requirements

Functional requirements for the primary side DSP include:

1. Two pairs of PWM signals for driving the phase-shift full-bridge circuit should be generated. The PWM period corresponding to the resonant circuit switching frequency should be in the range from 300 kHz to 400 kHz. For phase-shift PWM duty ratio control, there should be programmable time delay between the two pairs of PWM outputs.
2. Fast ADC channels are needed to sample three analog signals continuously. The fastest analog source is the tone signal (after filtering) for decoding the secondary output voltage and this signal needs to be sampled at a rate of 120 k samples/second. The other two analog signals are dc input voltage  $V_{IN}$  level and the peak of primary current level,  $I_{p,pk}$ . It is good to have a 12-bit ADC resolution, but 10-bit ADC is adequate. Appendix 5 provides an analysis of ADC resolution requirements for all analog signals.
3. An analog comparator is required to convert the sinusoidal shape primary current  $I_p$  into digital form for time difference comparison. A CPU with internal analog comparator will be a favourable choice. In order to change the reference current level at different values of coupling coefficient  $k$ , the reference voltage level in the analog comparator should be programmable.
4. The time difference between the output of analog comparator and the PWM control signal will be compared and the result will be used for switching frequency adjustment, it is desirable if the DSP CPU can assist the hardware module for performing the time measurement.

5. The CPU needs to perform DSP functions for tone signal decoding, system closed-loop control and switching frequency adjustment. Since these operations involve intensive DSP operations, the CPU of choice should contain hardware DSP engine that speeds up the computational performance.

In summary, the basic requirements for the DSP CPU are two inter-related PWM modules with 4 PWM output pins, 3 analog ADC pins, 1 analog comparator input pin, 2 digital input pins (with edge detection and time stamp, for phase difference measurement). There is one optional pin for the analog comparator output and two to three output test pins as system status indicators. Adding  $V_{CC}$ ,  $AV_{CC}$  (power) and  $GND$ ,  $AGND$  (ground) pins, CPU reset pin, system clock pin(s), and emulator control pins, a CPU with 20 pins to 28 pins is needed. For prototype board construction, it will be an added advantage if DIP package is available for the selected DSP CPU.

### 3.1.2 Primary Side DSP Selection

For sourcing DSP CPU, our first choice is Texas Instruments (TI), which has been the leading DSP manufacturer for many years. There have been numerous designs in control applications using the TMS320F28x series DSP. In terms of functional performance, TI's new Piccolo series microcontroller TMS320F28022 can be used as the primary side controller. Another DSP of choice is Microchip's dsPIC33FJ16GS502 DSP. Table 3-1 lists out the functional performances of the two DSPs, it can be seen that TI's DSP outperforms the Microchip's DSP in many ways. However, at the time hardware design began, the TI Piccolo chip was not available yet, only the precedent TMS320F28x series was available. However, this series of DSP all have a large pin count of 100, which is too many for our design, so the Microchip's dsPIC33FJ16GS502 DSP was selected as the primary side controller. Moreover, the Piccolo chip is only available in 38-pin plastic small outline package (PSOP) or 48-pin plastic quad flatpack (PQFP) package, an adaptor socket is needed to connect the DSP to the prototype board.

Figure 3-1 shows the block diagram of the Microchip's DSP, which belongs to the GS series DSP. This series is specially designed for switching mode power supply (SMPS) applications. As the CPU system clock is generated by an on-chip oscillator (at 7.37 MHz), there is no need for an external crystal. The clock frequency is further increased to 80 MHz (for 40 MIPS performance) by an on-chip PLL. The PWM resolution is 1.04 ns. Thus, when the switching frequency is set between 300 kHz and 400 kHz, it will have a corresponding

PWM period count value between 3200 and 2400. The period count corresponds to a true 12-bit controllable PWM resolution, which is acceptable in our application.

Table 3-1: Comparison between TI's DSP and Microchip's DSP

	TMS320F28022	dsPIC33FJ16GS502
Program flash	32k bytes	16k bytes
On-chip RAM	12k bytes	2k bytes
Processing speed	50 MIPS (max.)	40 MIPS (max.)
PWM resolution	180 ps	1.04 ns
ADC resolution	12 bits	10 bits
ADC conversion speed	3 MSPS (max.)	4 MSPS (max.)
Capture pin with time-stamp	1 / 2	2
On-chip oscillator	Yes	Yes

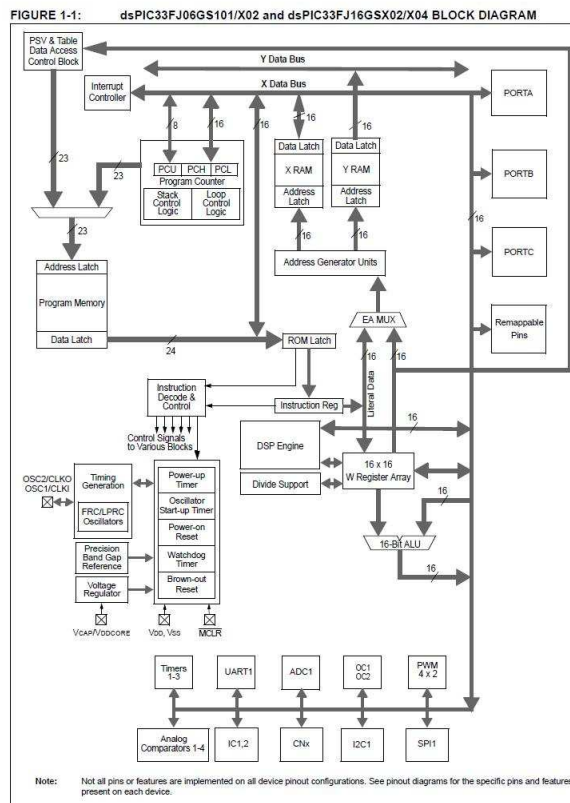


Figure 3-1: Block diagram of dsPIC33FJ16GS502 DSP [138]

### 3.1.3 Inductor Coils Selection

The transcutaneous transformer is the medium of power transfer during inductive coupling. Its construction is critical for achieving high power efficiency. Coupling coefficient  $k$  can be maximized by using transformer coils with larger coupling areas. Further improvement in  $k$  can be made by using a ferrite core, so that the magnetic flux is more concentrated, producing less leakage flux. Another issue in the transformer coil design is to reduce the loss during coupling. The loss is mainly due to the ac resistance in the coil, causing eddy currents, skin depth effect and proximity effect.

For an individual wire, current tends to concentrate along the outer wall, hence the name skin effect. For the influence of the current through neighbouring wires, the term proximity effect applies. A useful parameter for assessing the degree to which skin and proximity effects take place is the skin depth  $\delta$ . It is defined as the distance over which an EM planar wave in a conductive medium is attenuated by  $1/e$  ( $\approx 0.37$ ), it can be calculated as

$$\delta = \sqrt{\frac{2\rho}{\omega\mu}} \quad (3.1)$$

where  $\rho$  = resistivity of conductor,

$\omega$  = angular frequency of current,

$\mu$  = absolute magnetic permeability of conductor.

For copper, the skin depth at various frequencies is shown in Table 3-2. To reduce the loss due to skin depth effect, Litz wires are used in the construction of the transcutaneous transformer coils. Litz wires are conductors made up of multiple individually insulated strands twisted or woven together. The diameter of individual strand wire is so small that the eddy-current losses are minimized. In our system, the Litz wires for transformer coils are AWG 46×640. From Table 3-3, it can be seen that the transcutaneous transformer can operate up to 1 MHz of switching frequency.

Table 3-2: Skin Depth of Copper Wire at Various Frequencies

Frequency	Skin Depth ( $\mu\text{m}$ )
60 Hz	8470
10 kHz	660
100 kHz	210
1 Mhz	66
10 Mhz	21

(Source: [http://en.wikipedia.org/wiki/Skin\\_effect](http://en.wikipedia.org/wiki/Skin_effect))

Table 3-3: AWG Gauges Table

AWG	Diameter (mm)	AWG	Diameter (mm)
10	2.590	15	1.450
20	0.813	25	0.455
30	0.254	35	0.142
40	0.079	46	0.040

The transcutaneous transformer is made up of two spiral shape circular coils at the primary and secondary sides. Formulae for inductance calculation can be found in [140], and the formula for calculating the mutual inductance between circular coils with inclined axes can be found in [141]. However, for inductive coupling application, the coupling coefficient  $k$  will be of more interest. There are some guidelines [142-143] to improve the coupling coefficient when building the transformer coils:

- Enhancement is achieved by distributing the turns of the coils across the radii instead of concentrating them at the outer circumferences.
- Transcutaneous transformer with larger outer radius is less sensitive to gap variations, so there is less change in the coupling coefficient when the gap separation is changed.
- Outer diameter of the primary winding must be bigger than the outer diameter of the secondary winding, and inner diameter of primary winding must be smaller than the inner diameter of the secondary winding.



- Series resistance is a major loss in our system. For best power converter efficiency and high Q resonant tank operation, capacitors with low ESR should be used. Metallized plastic film capacitors will be a good choice and suitable dielectrics are polyester, polypropylene, and polystyrene. Another choice is the multilayer ceramic (MLC) capacitors. The rated voltage can be up to 5000 V and exhibit low ESRs at high frequencies. But the MLC capacitors are more expensive.
- Capacitors should have a high voltage rating. Series connected resonant tanks normally ring with high voltage. Thus, the capacitors in use should withstand considerable voltage strength. According to captured voltage waveforms in the experiment, the peak resonant voltage can be up to 200 V, and the voltage rating  $> 500$  V is preferred.

AVX SMD type high voltage MLC chips 1000 V, 2200 pF, COG type capacitors (Part number 1812AA222JA) are selected as the resonant capacitors. In order to further reducing the ESR value, five SMD capacitors are soldered together to form one resonant capacitor. The surface mould (SMD) type package is used because of their small size, and they can be easily soldered or removed from the PCB.

The measured capacitance values for  $C_p$  and  $C_s$  are 10.99nF and 11.09nF, respectively. Their effective ESR is 19 m $\Omega$  (300 kHz) and 17 m $\Omega$  (400 kHz) for  $C_p$  capacitor; and is 22 m $\Omega$  (300 kHz) and 20 m $\Omega$  (400 kHz) for  $C_s$  capacitor. The ESR resistances are much lower than the series resistances in the inductor coils.

### 3.1.5 Power MOSFETs Selection

The power MOSFETs are the switching devices for the phase-shift full bridge circuit. The flowing current is mainly the primary inductor current (max. 5A peak) and the voltage strength is the  $V_{IN}$  input voltage (30 V to 45 V). The basic requirement is fast switching (i.e. low  $C_{gs}$  and  $C_{gd}$ ) and low  $r_{DS(on)}$  resistance, and the voltage rating is 80 V or above.

The selected MOSFETs are Vishay's Si7852ADP. They are 80V n-channel MOSFET, and have a low  $r_{DS(on)}$  resistance of 17 m $\Omega$  at  $V_{GS} = 10$  V. The gate-source charge  $Q_{gs}$  is 9 nC and the gate-drain charge  $Q_{gd}$  is 8 nC (at  $V_{DS} = 40$  V and  $V_{GS} = 10$  V), and the typical values of rise time and fall time are 9 ns and 9 ns, respectively.

### 3.1.6 Rectifier Diodes Selection

There are two places in the control circuit where rectifier diodes are used. In the primary circuit, the diodes are placed in parallel with the switching MOSFETs, with direction the same as the NMOS's body diodes. The selected (totally four) schottky diodes are having low forward voltage, and they replace the function of the body diodes so that power loss is reduced during the time period of reverse current flow when the attached MOSFET is 'off'.

Another place for the rectifier diodes is the full-bridge rectifier at the secondary output. Since two of the diodes are conducting when there is current flowing to the load, selection of rectifier diodes with low forward voltage drop is crucial to achieving high power efficiency.

The selected rectifier diode is Vishay's V10P10 high current density surface mount Trench MOS barrier schottky rectifier. The breakdown voltage is 100V and it can allow 10 A of continuous current flow. Its forward voltage  $V_F$  is 0.453 V at  $I_F = 5$  A at 25°C.

### 3.1.7 Hardware Prototype Board

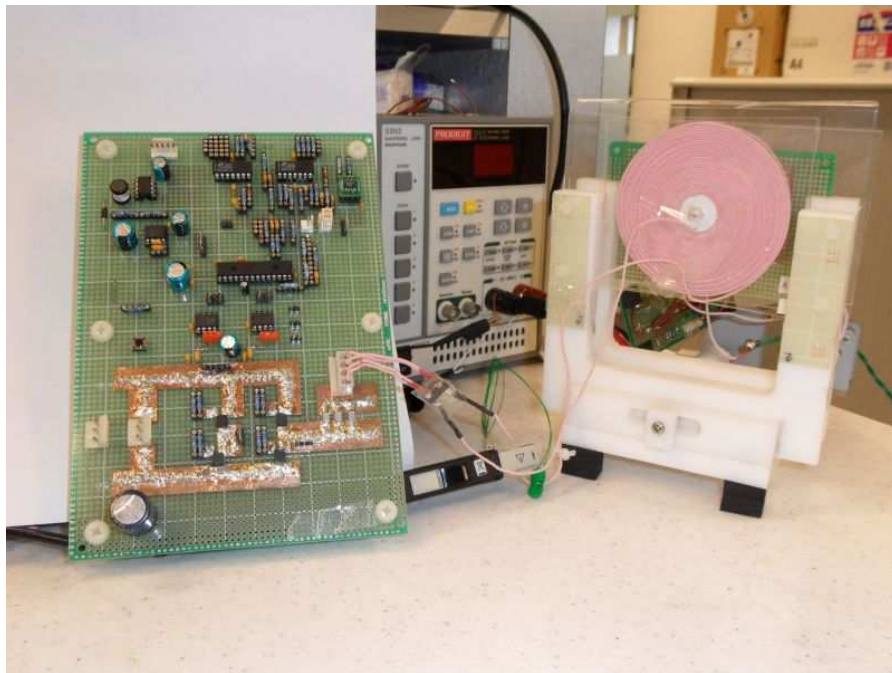


Figure 3-2: Primary side controller board and transcutaneous transformer

Figure 3-2 shows the image of the primary side controller board (left) and the transcutaneous transformer (right). The circuit diagram of the primary side controller is shown in Appendix 1. The components used by the primary controller board are selected

according to the discussions in the previous sections. At the lower end of the primary controller board are the four MOS transistors for PSFB control. An advantage of the ZVS mode of operations is that there is a minimum amount of heat generated and no heat sinks are required. To shorten the circuit connection path, the SMD resonant capacitors are placed directly between the full-bridge circuit and the header for the primary transformer coil.

At the middle of the board is the heart of the primary side controller, the 28-pin dsPIC33FJ16GS502 DSP. It is operating at 3.3 V supply voltage with an internal oscillator running at 7.37 MHz. An on-chip PLL multiplier will speed up the system clock for 40 MIPS operation. Between the DSP and the MOS transistors are ICs for gate driving, the International Rectifier's IRS2011. They are high and low side gate drivers, one for one leg of the full-bridge rectifier.

At the upper end of the board are the analog components, two op-amp ICs and one low-pass filter. The purpose of the analog circuits is to shape the three ADC signals and one comparator signal for the DSP chip. The input voltage range for the ADC signals is 0 V to 3.3 V ( $V_{DD}$ ), and for analog comparator signal the voltage range is 0 V to 1.2 V. In order to reduce the switching noise coupled to the analog circuits, the PWM switching circuits and the analog circuits are intentionally placed at the two ends of the PCB.

At the upper left side of the board is the supply voltage generation circuit, which will generate  $\pm 5$  V voltage for the op-amp chips, and +3.3 V supply voltage for the DSP. All these voltages are generated from a +12 V voltage source, and it is also the supply voltage for the gate driver ICs.

The  $V_{IN}$  voltage to the full-bridge circuit comes from another header (closed to the MOS transistors), and the voltage range is from 30 V to 45 V.

Figure 3-3 shows an expanded view of Figure 3-2. It can be seen that a toroid (with green color wiring) is passing through the primary transformer coil. The toroid is functioned as a current pick-up device, and the wire endings are connected to a 2-pin connector. The connector will be plugged into the primary side controller board (upper-left corner of Figure 3-3), at which primary current waveform will be converted into voltage signal. The peak level of primary current is obtained using peak detector circuit. The tone signal for secondary voltage identification is also derived from the primary current signal. The signal first passes through a peak detection circuit, low-pass filtering, and then band-pass filtering.

Figure 3-4 shows the circuit board at the secondary side of the transcutaneous transformer. This part of the circuits is assumed to be placed inside the human body. The circuit board contains a 4-pin header for connection to the secondary transformer coil, the secondary side resonant capacitor  $C_p$ , the full-bridge rectifier (with four diodes), and the

output capacitor  $C_O$ . There are also header pins connected to the circuit's output voltage. These headers are connections to electronic load and voltmeter for circuit testing and monitoring.

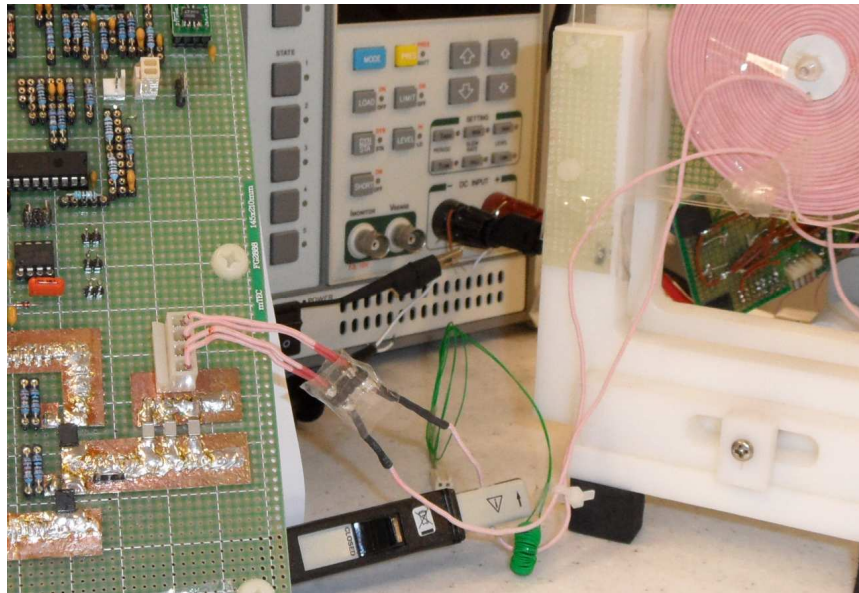


Figure 3-3: Expanded view to show the current pick-up toroid

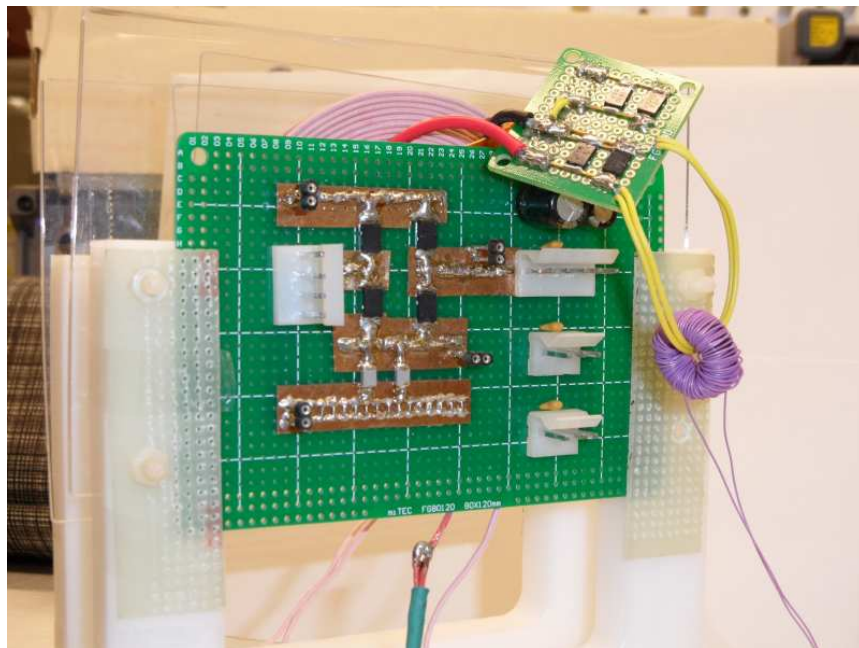


Figure 3-4: Secondary side rectifier board

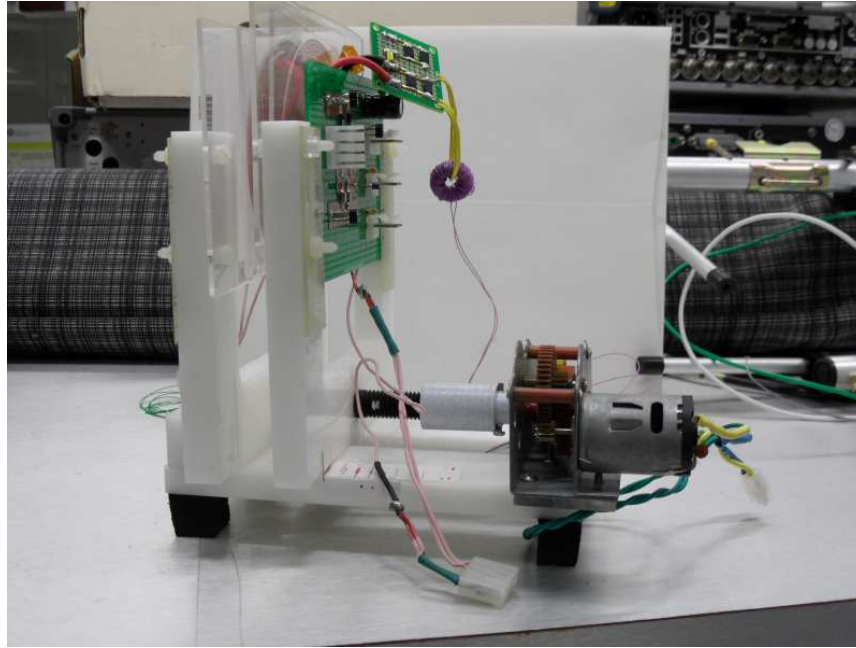


Figure 3-5: Mechanical setup for transcutaneous transformer

### 3.2 Secondary Side Controller Board

The secondary side of the power converter is a much simpler design. There is a 4-bit MCU that functions as an output voltage sampler and a square wave tone signal generator (according to the result of A/D sampling). There is a 60:1 transformer that converts the  $\pm 6$  V square wave signal into  $\pm 0.1$  V and injects it into the output circuit path.

The major requirement of the secondary side controller is small size and low power consumption. The small size requirement is due to the limited space inside the human body, and the low power requirement is for the reduction of unwanted heat generation. The CPU of choice is Micorchip's 4-bit MCU PIC12F615, and it is an 8-pin CPU that can operate at 2 V supply voltage. Typical supply current is 245  $\mu$ A ( $V_{DD} = 2.0$ V, internal oscillator @4 MHz). The CPU contains a 10-bit analog-to-digital converter (ADC) for output voltage sampling. An output tone signal with frequency between 20 kHz to 30 kHz is generated with an on-chip hardware PWM module. Figure 3-6 shows the block diagram of the PIC12F615 CPU.

Figure 3-7 shows the secondary side controller board, and its circuit diagram is shown in Appendix 2. The input power to the board can be sourced from an external +12 V power supply, or directly from the 24 V secondary output voltage. For normal operation, the voltage source will be the secondary output voltage. It has been tested thoroughly that the secondary controller board can be powered up with the output voltage starting up initially at zero

voltage. The driving circuit for voltage coupling coil is a half-bridge circuit, and an IRS2004 half-bridge driver is used to drive two low-power BS170 MOSFETs. There is a shutdown control in the half-bridge driver. When the secondary output voltage is below 12 V, the half-bridge driver is disabled and no square-wave tone signals are sent out. There are two LED lamps on the prototype board as status indicators, the red LED will flash at a rate according to the secondary output voltage level. When the voltage level is low, the flashing rate is slow; when the voltage level is high, the LED flashing rate is high. For the green LED, it is turned on when the output voltage level is within the 24.0 V±0.15 V range.

Since the whole secondary board will be placed inside the human body, circuit design with few components count is used. When all circuit components are changed into surface mount type, the final PCB size can be significantly reduced.

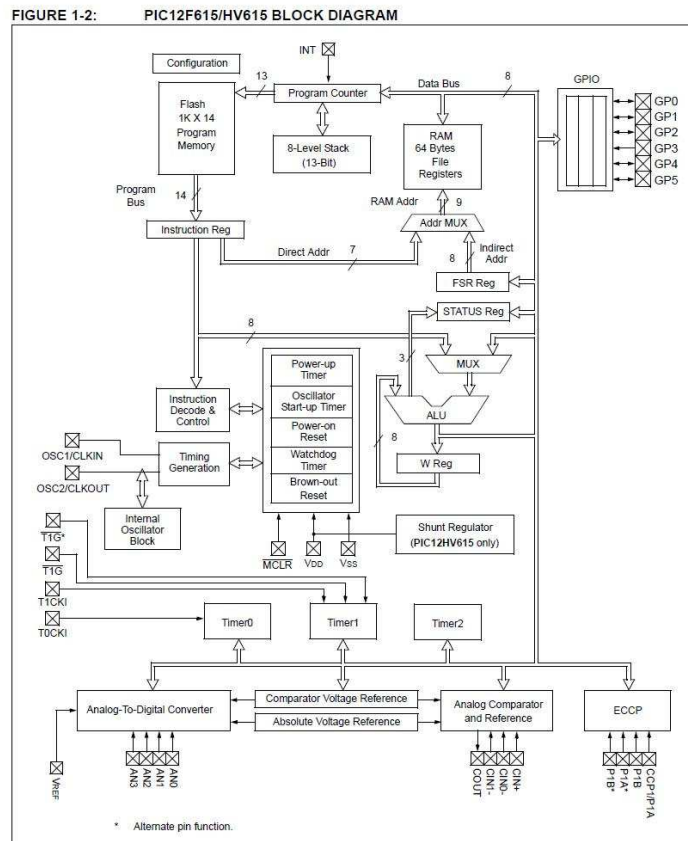


Figure 3-6: Block diagram of PIC12F615 MCU [139]

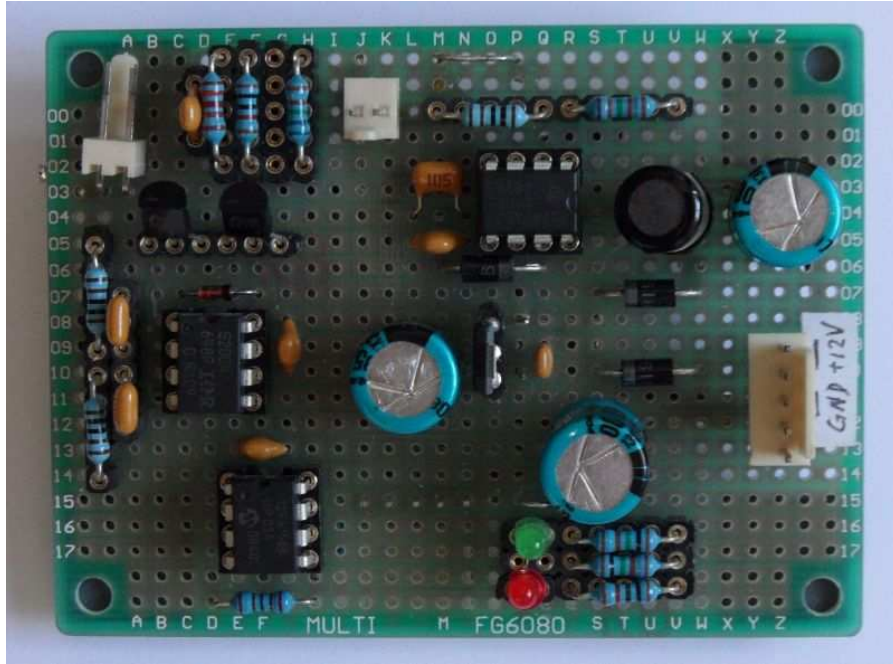


Figure 3-7: Secondary side controller board

### 3.3 Switching Frequency Control

Control of the switching frequency is done by tracking the primary current  $I_p$  level at the beginning of PWM signal. The exact control method is implemented as a phase-locked loop (PLL) frequency tracking algorithm with PI control for phase error compensation.

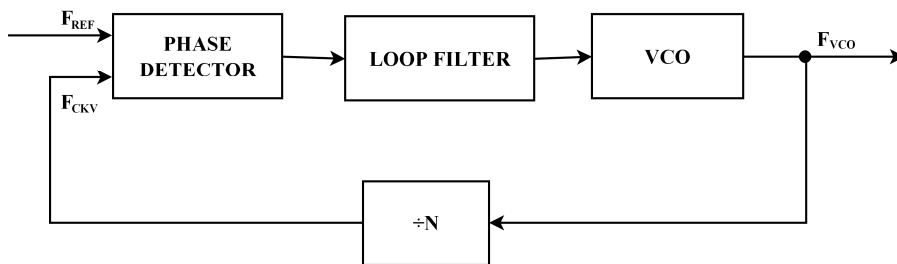


Figure 3-8: Block diagram of analog PLL

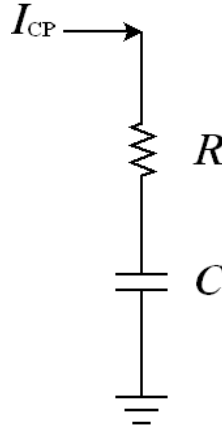


Figure 3-9: Loop filter for CPPLL

Figure 3-8 shows the block diagram of an analog phase-locked loop. A reference signal (i.e. the primary current  $I_P$ ) of frequency  $F_{REF}$  is compared with the output signal (i.e. the PWM switching signal) of frequency  $F_{CKV}$ . There is a gain of  $K_P$  in phase detector and the resulting phase difference is low-pass filtered by the loop filter. The output of the loop filter is a slowly moving dc voltage. When the dc voltage level is changed, the frequency of the voltage controlled oscillator (VCO) is updated and a new frequency signal is generated for phase comparison.

In the PLL design, the high and low frequency range must be defined. The open-loop gain is

$$H(s) \cdot G(s) = K_p \cdot K_f \cdot K_o \cdot K_n \quad (3.2)$$

where  $K_p$  = phase comparator gain

$K_f$  = low-pass filter transfer gain

$K_o = K_v/s$ , is the VCO gain

$K_n = 1/n$ , the divider ratio

The open-loop gain of the charge-pump phase-locked loop (CPPLL) in Figure 3-9 is given by [144, 145]

$$LG(s) = \frac{I_{CP}}{2\pi} \cdot \frac{K_{VCO}}{s} \cdot \frac{1}{N} \cdot \frac{s + \omega_z}{s} \cdot R \quad (3.3)$$

where  $\omega_z$  is the zero frequency

$$\omega_z = \frac{1}{RC} \quad (3.4)$$

The phase margin for the system is given by

$$PM = \arctan\left(\frac{\omega_{UGBW}}{\omega_z}\right) \quad (3.5)$$

In other words, given the PLL specifications of the phase margin ( $PM$ ) and the unity gain bandwidth ( $\omega_{UGBW}$ ), the required zero frequency  $\omega_z$  can be found as

$$\omega_z = \frac{\omega_{UGBW}}{\tan(PM)} \quad (3.6)$$

Based on  $|LG(j\omega_{UGBW})|=1$ , the resistance value  $R$  can be found as

$$R = \frac{2\pi N}{I_{CP}K_{VCO}} \cdot \frac{\omega_z^2}{\sqrt{\omega_z^2 + \omega_{UGBW}^2}} \quad (3.7)$$

Then, from (3.3) and (3.5), the capacitance value  $C$  is found to be

$$C = \frac{\tan(PM)}{R \cdot \omega_{UGBW}} \quad (3.8)$$

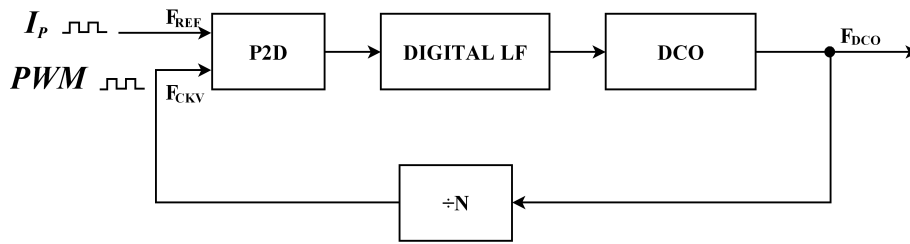


Figure 3-10: Block diagram of all-digital PLL

For digital software implementation, the block diagram of PLL is modified as shown in Figure 3-10. It consists of a phase-to-digital converter (P2D), a digital loop filter (LF), a digitally controlled oscillator (DCO), and a feedback divider. The P2D senses the phase difference between the reference clock  $F_{REF}$  and the DCO dividing clock  $F_{CKV}$ . This information is filtered by the first-order digital LF and then is used to control the DCO. The reference clock  $F_{REF}$  is obtained from the analog comparator output of the  $I_p$  primary current, and it is a digital output signal. In our system, the divider  $N$  is equal to one and the DCO clock signal ( $F_{CKV}$ ) is actually the full bridge PWM driving signal.

The all-digital phase-locked loop (ADPLL) of Figure 3-10 has a structure and operation very similar to a second-order CPPLL. The principal difference is that the phase error information is processed in different ways. The rising edges of the digitalized  $I_p$  and the PWM signals are captured by the DSP's input capture hardware module, one for each input signals. The time of input capture is saved as a 16-bit counter value obtained from Timer 3,

which is running at a clock speed of 40 MHz. Thus, the time resolution of the counter value is 25ns, and the difference of the counter value  $cnt_{diff} = (cnt_{PWM} - cnt_{ip})$  is the resulting output of the phase-to-digital converter. The switching frequency of the power converter is between 300 kHz to 400 kHz, and taking the worst case 400 kHz frequency for calculation, the transfer function of the P2D module (i.e. the gain  $K_p$ ) is

$$P2D(s) = \frac{T_{REF}}{2\pi \cdot \Delta_{TDC}} = \frac{1/400 \times 10^3}{2\pi \cdot 25ns} = \frac{50}{\pi} \quad (3.9)$$

A digital equivalent of an analog loop filter consists of a proportional path with a gain  $\alpha$  and an integral path with a gain  $\beta$ . The z-domain transfer function of the digital loop filter is given by

$$LF(z) = \alpha + \beta \frac{1}{1-z^{-1}} = \frac{(\alpha + \beta) - \alpha z^{-1}}{1-z^{-1}} \quad (3.10)$$

The parameters of a digital loop filter  $\alpha$  and  $\beta$  can be obtained from the parameters of an analog loop filter R and C by using the bilinear transform. The bilinear transform is commonly used to design digital filters based on their analog prototypes.

$$s = \frac{2}{T_s} \frac{1-z^{-1}}{1+z^{-1}} \quad (3.11)$$

where  $T_s$  is the sampling time of a discrete-time system, which is 0.5 ms in our DSP system.

For the CPPLL, a charge pump (CP) is used to generate a charge which is proportional to the time difference between the UP and DN pulses. The resulting charge is pumped into the analog filter, the output voltage of which controls the VCO. This similarity allows one to extend the design procedure for a second-order CPPLL to a second-order ADPLL.

The phase error in the digital domain is filtered by a first-order digital loop filter and then fed into the DCO with a transfer function given by

$$DCO(s) = \frac{K_{DCO}}{s} \quad (3.12)$$

Again using the worst-case switching frequency of 400 kHz, the PWM resolution is 1.04 ns (or 1/960 MHz). Thus, 400 kHz is represented as  $960 \times 10^6 / 400 \times 10^3 = 2400$  PWM period counter value. So,

$$K_{DCO} = \frac{400 \times 10^3}{2400} = 167 \quad (3.13)$$

The design of the digital PLL loop filter follows the procedures in [145]. The sampling time  $T_s$  is 0.5 ms, and the unity gain bandwidth  $\omega_{UGBW}$  is set to 1/10 of the sampling frequency ( $= 2\pi \times 200$  Hz). Also, the phase margin (PM) is set to 45°, and the required zero  $\omega_z$  is

$$\omega_z = \frac{\omega_{UGBW}}{\tan(PM)} = \frac{2\pi \times 200}{\tan(45^\circ)} = 1257 \quad (3.14)$$

With  $I_{CP}$  equal to  $2\pi \times P2D(s)$ , the values of the filter components can be found as

$$R = \frac{N}{P2D(s) \cdot K_{DCO}} \frac{\omega_z^2}{\sqrt{\omega_z^2 + \omega_{UGBW}^2}} = \frac{1}{50/\pi \cdot 167} \frac{1257 \times 1257}{\sqrt{1257^2 + 1257^2}} = 0.3344$$

$$C = \frac{\tan(PM)}{R \cdot \omega_{UGBW}} = \frac{1}{0.3344 \times 1257} = 2.38 \times 10^{-3}$$

and the filter coefficients are

$$\alpha = R - \frac{T_s}{2C} = 0.3344 - \frac{0.5 \times 10^{-3}}{2 \times 2.38 \times 10^{-3}} = 0.23$$

$$\beta = \frac{T_s}{C} = \frac{0.5 \times 10^{-3}}{2.38 \times 10^{-3}} = 0.21$$

### 3.4 Secondary Output Voltage Feedback Control

As discussed in Section 2.4.2, tone signals between 20 kHz and 30 kHz will be used to transmit the secondary output voltage information from the transformer secondary to the primary side for voltage regulation. Three different signal modulation methods can be used for information transmission, namely, amplitude modulation, frequency modulation, and phase modulation.

In terms of work load in demodulation, amplitude modulation is the simplest way of decoding. The tone signal at a predefined frequency is obtained by band-pass filtering, and the tone amplitude will then be mapped to a value that represents the secondary output voltage. This method will work when output loading is fixed. Another condition is that there should be no variation in coupling coefficient  $k$ . As shown in Figure 2-13, the tone signal amplitude in the primary current is changing with the output loading  $R_L$  and with coupling coefficient  $k$ , it is difficult to set the reference tone level that corresponds to the desired 24 V output voltage level.

With the advances in DSP algorithm development, frequency spectrum calculation can be done with moderate complexity. So, frequency modulation is a viable solution for data transmission, and the problem is how fast the information data can be decoded.

For phase modulation, information can be transmitted as two sinusoidal tone signals, one at frequency  $X$  and the other one at frequency  $2X$ . The phase difference between the two tones can be retrieved as data information. However, this method can only be applied for

situation where the switching frequency is fixed. When the switching frequency is changing (for output load change or  $k$  value change), there is a phase offset between the two tone signals. Even worse, for different load settings, the phase offset will be different. Another way for phase modulation is to transmit only a single tone frequency, but the tone signal is divided into segments of fixed time slots. Between two time slots, the phase of the two segments will be adjusted to represent new data information. Decoding at the primary side must include phase information decoding together with algorithm for data segment synchronization, and the decoding job is much more complex than frequency demodulation. Also, signals sent out at the secondary side must be sinusoidal in shape, not square-wave as in the frequency modulation case.

Due to the difficulty in obtaining good results in amplitude modulation or phase modulation, frequency modulation technique is selected as the method of secondary voltage information transmission. Decoding of tone signals is done by Goertzel algorithm, which is a fast DSP algorithm for tone detection. The tone signal is decoded for every 0.5 ms time interval.

The Goertzel algorithm for  $N$  consecutive samples of data is summarized as below [146]:

1. Recursively compute for  $n = 1, \dots, N$

$$v_k(n) = 2 \cos(2\pi f_k / f_s) \cdot v_k(n-1) - v_k(n-2) + x(n) \quad (3.15)$$

where  $v_k(-1) = 0$ ,  $v_k(0) = 0$ , and  $x(n)$  is the input waveform sequence.

2. Compute once at the last step

$$|X(k)|^2 = v_k^2(N) + v_k^2(N-1) - 2 \cos(2\pi f_k / f_s) \cdot v_k(N) \cdot v_k(N-1) \quad (3.16)$$

where  $|X(k)|^2$  is the spectral energy of the  $k$ -th tone.

At the start of every 0.5 ms interval, 16 samples of ADC data of the tone signal are consecutively read into a data buffer, and spectral information in the form of squared magnitude at seven frequency points are calculated. Besides the five tone frequencies listed in Table 3-5, additional frequencies at both ends of the tone frequency range (i.e., 17.5 kHz and 32.5 kHz) are added for detection of unwanted disturbances nearby. To prevent random noise being treated as a valid tone signal, a threshold level for the decision of good or bad tone signals is necessary. As shown in the macromodel simulation results of Figure 3-11, the tone signal responses in the frequency range of 20 kHz to 30 kHz for different values of output loading resistance  $R_L$  are similar, with smaller response amplitude for larger  $R_L$ . But since the magnitude of the primary current level is different when the output load changes,

the received tone signal amplitude is smaller for larger  $R_L$ . To account for the signal level changes with different output loads, a threshold level proportional to the square of the peak primary current,  $I_{Ppk}$ , is used to compare with the tone signal spectral energy level.

Table 3-5: Tone Frequency Assignment for Secondary Output Voltage

Secondary output voltage (V)	Tone frequency
Below 12.00 V	No tone signal
12.00 – 23.25	20.0 kHz
23.25 – 23.85	22.5 kHz
23.85 – 24.15	25.0 kHz
24.15 – 24.75	27.5 kHz
Over 24.75 V	30.0 kHz

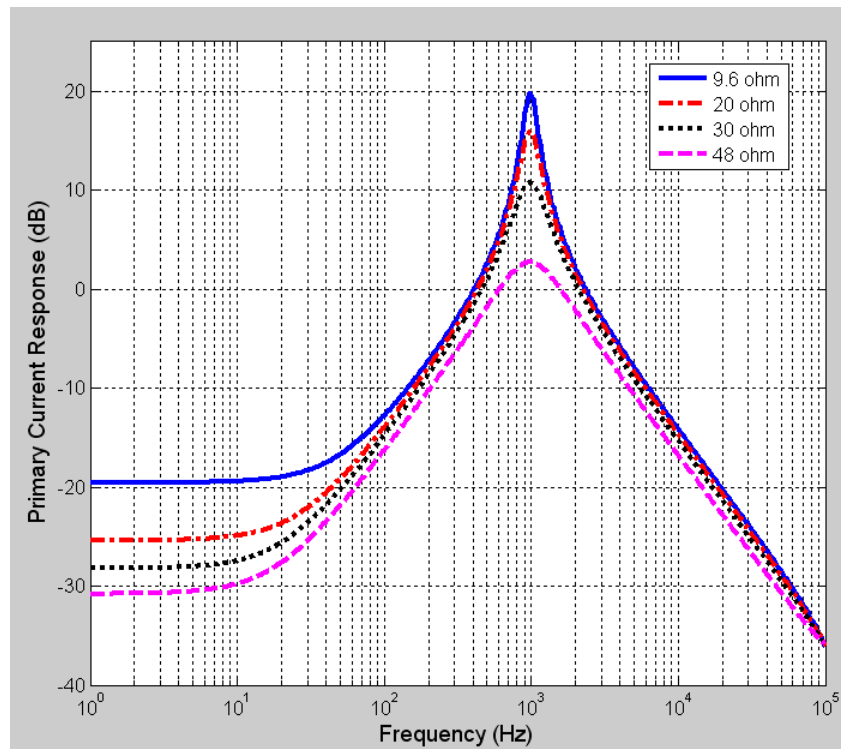


Figure 3-11: Frequency response of primary current to secondary tone signal for different output load  $R_L$

The tone signal ADC data,  $x(n)$ , are treated as 16-bit data, and the energy data,  $v_k(n)$ , are 32-bit data. The coefficient data for each of the tone frequency,  $\cos(2\pi f_k/f_s)$ , with  $f_s = 120$  kHz, are scaled by 1024 levels and are treated as 16-bit data. Their values are listed in Table 3-6.

Table 3-6: Data Coefficients for Goertzel Algorithm

Tone frequency	$\cos(2\pi f_k/f_s)$	Data Scaled by 1024
17.5 kHz	0.6088	623
20.0 kHz	0.5000	512
22.5 kHz	0.3828	391
25.0 kHz	0.2588	265
27.5 kHz	0.1305	133
30.0 kHz	0.0000	0
32.5 kHz	-0.1305	-133

### 3.5 Voltage Loop Control

Figure 2-11 shows the line-to-output response of the TET circuit at different gap separations, and the response for 9.6  $\Omega$  output load is shown (in blue color) in Figure 3-12 again. Generally speaking, the worst case in stability control exists with low resistance output loading. For analog circuit control, a type II compensation circuit can be used to stabilize the control loop, resulting in a unity-gain bandwidth of 2 kHz with 50° phase margin. However, the primary controller board is now using DSP for system control and the control-loop stability is handled by software using a PI (proportional-integral) control algorithm. The digital PI controller is updated every 0.5 ms, and it will create a time delay effect called zero-order hold on the control system. Due to the simple response shape of the PI controller and the zero-order hold effect, the unity-gain bandwidth has to be selected at a lower frequency, e.g., 30 Hz, and the corresponding phase margin is close to 90°.

The frequency response of the PI controller is

$$H(s) = K_p + \frac{K_I}{s} = 0.06 + \frac{20}{s} \quad (3.17)$$

and the corresponding transfer function in the z-domain is

$$H(z) = \frac{0.06z - 0.045}{z - 1} \quad (3.18)$$

The converter response curves using the PI controller are shown in Figure 3-12 in purple colour. In the transcutaneous power converter system, the secondary output voltage is first sampled by a microcontroller at the secondary side, and a tone signal is then generated at the secondary circuit. The tone signal will couple through the transcutaneous transformer and it will lead to primary current fluctuation. At the primary side, the small amplitude tone variation in the primary current is picked up by an analog amplifier circuit together with low-pass/band-pass filters. So, there will be time delay due to tone decoding, and time delay for analog signal transmission. The time delay for tone signal decoding is the time of one complete tone period, which is 50  $\mu$ s for 20 kHz tone and 33  $\mu$ s for 30 kHz tone. For normal operation, the output voltage should be around 24.0 V and a tone frequency of 25 kHz will be generated, and the nominal time delay is 40  $\mu$ s. The analog circuit travel time delay is measured with an oscilloscope and the results are shown in Figure 3-13. The time delay for the 20 kHz tone signal is 75  $\mu$ s and for 30 kHz tone signal is 70  $\mu$ s. The worst-case total time delay is 125  $\mu$ s, which is 1/4 of the time between PI controller update. According to [147], the time delay in digital control mostly affects the system phase response at high frequency. But since the unity gain bandwidth in our system is set to a low frequency (and with large phase margin), the stability of the control loop will not be affected by the time delay.

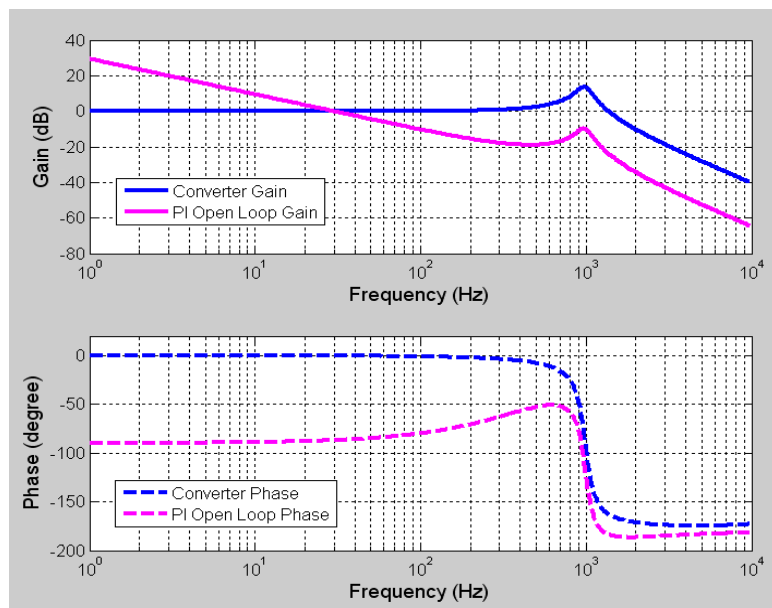
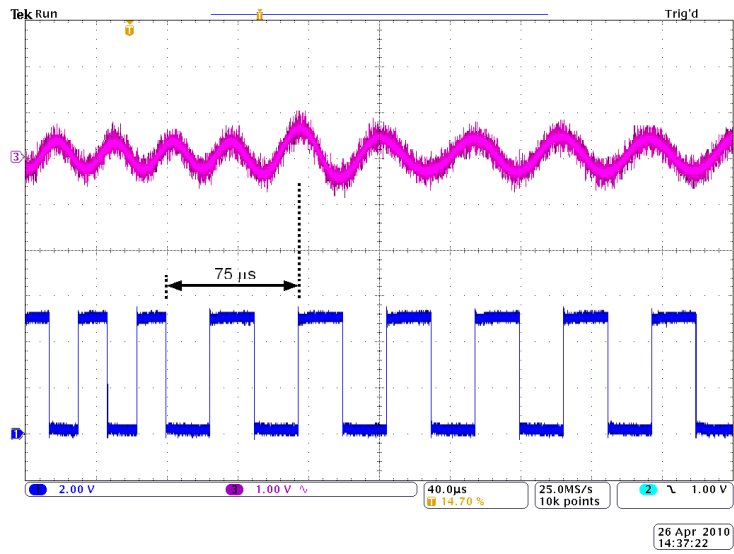
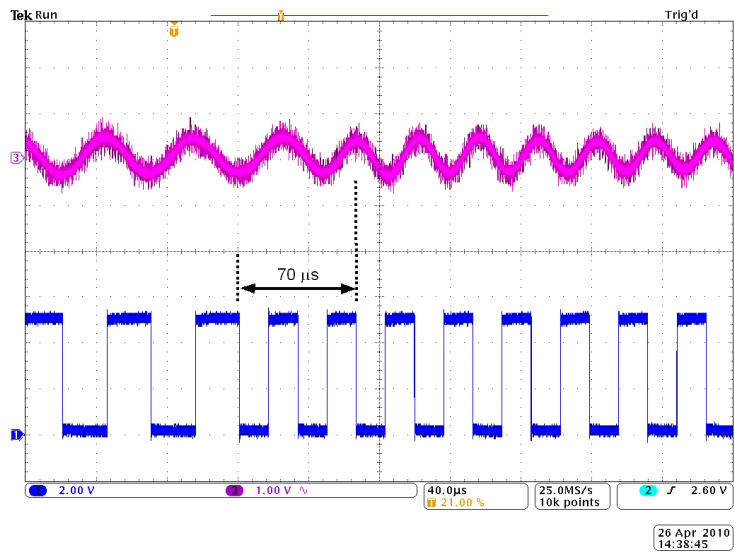


Figure 3-12: Converter response using PI compensation



(a) 20 kHz tone signal time delay



(b) 30 kHz tone signal time delay

Figure 3-13: Time delay for tone signal from secondary side to primary

### 3.6 Effect of Duty Ratio on Output Voltage (Input Voltage Feed-forward)

By fundamental magnitude approximation (FMA), we get

$$V_{s, pk} = V_{IN} \cdot \frac{4}{\pi} \sin\left(\frac{D\pi}{2}\right) \quad (3.19)$$

where  $V_{s, pk}$  is the peak amplitude of the AC equivalent sinusoidal input voltage. Thus,

$$\frac{\partial V_{s, pk}}{\partial D} = 2 \cdot V_{IN} \cdot \cos\left(\frac{D\pi}{2}\right) \quad (3.20)$$

Clearly, for different values of duty ratio  $D$ , the AC input voltage amplitude is nonlinearly changing with  $D$ , and the same effect will occur at the secondary output voltage. To linearize the effect of PWM duty ratio control, a scaling factor of

$$\delta = \frac{1}{2 \cdot V_{IN} \cdot \cos\left(\frac{D\pi}{2}\right)} \quad (3.21)$$

is applied to the final control signal of the duty cycle, and the evaluation of  $\cos(\cdot)$  function is implemented using a 64-entry lookup table. By the addition of the scaling factor  $\delta$ , the effect of input voltage  $V_{IN}$  is now included in the closed-loop control system. So, it is an input voltage feed-forward control system.

The input voltage range of our power converter is specified as 30 V to 45 V. It is not suggested to work with input voltage higher than 45 V. At high input voltage  $V_{IN}$ , in order to regulate the secondary output voltage  $V_O$  to the desired 24 V level, the PWM duty ratio  $D$  will become small. A small duty PWM signal has a larger phase difference with the primary current  $I_p$  and a higher switching frequency (away from the resonant frequency  $f_r$ ) is required in order to meet the ZVS condition. There are two disadvantages for running switching frequency away from the resonant frequency. First, the power efficiency will drop. Next, the received power level of the tone signal from the secondary side will become weaker when the switching frequency is off from resonance, and it will increase the failure rate of tone demodulation.

### 3.7 Transient Output Voltage Control

Since the primary current  $I_p$  is the medium for receiving the secondary output voltage tone signal, it is required that the rate of change of  $I_p$  is much slower than the tone signal.

When there is a large change in  $I_p$ , (i.e., during start-up, input voltage change, and output load change), the tone signal will be distorted and tone decoding will fail. Thus, supplementary methods of voltage control during transient conditions are necessary.

At start-up, the principle of operation is to limit the primary current rising rate. First, the switching frequency will be set to the highest allowable frequency (i.e., 400 kHz) so that the ZVS condition is ensured. Next, the peak level of the primary current  $I_{p,pk}$  is monitored. If the current rising rate is too fast, PWM control will be used to restrict it. During this time, there is no output voltage tone signal decoding. To prevent over voltage at the secondary output, the maximum level of  $I_{p,pk}$  is limited to 2 A. When the primary current is detected to be stable for more than 10 ms, it will enter the normal working mode and tone decoding will start. At the same time, the phase control algorithm will drive the switching frequency to the desired frequency range near resonance.

As mentioned previously, the effect of input voltage  $V_{IN}$  has been absorbed in the scaling factor for PWM control. Thus, there is no special handling for input voltage. However, when there is sudden change in the input voltage which is faster than the PWM voltage control loop, PWM control will be used to regulate  $V_{IN,pk}$  according to equation (3-19), and afterward it will wait for the new coming tone signals for output voltage control.

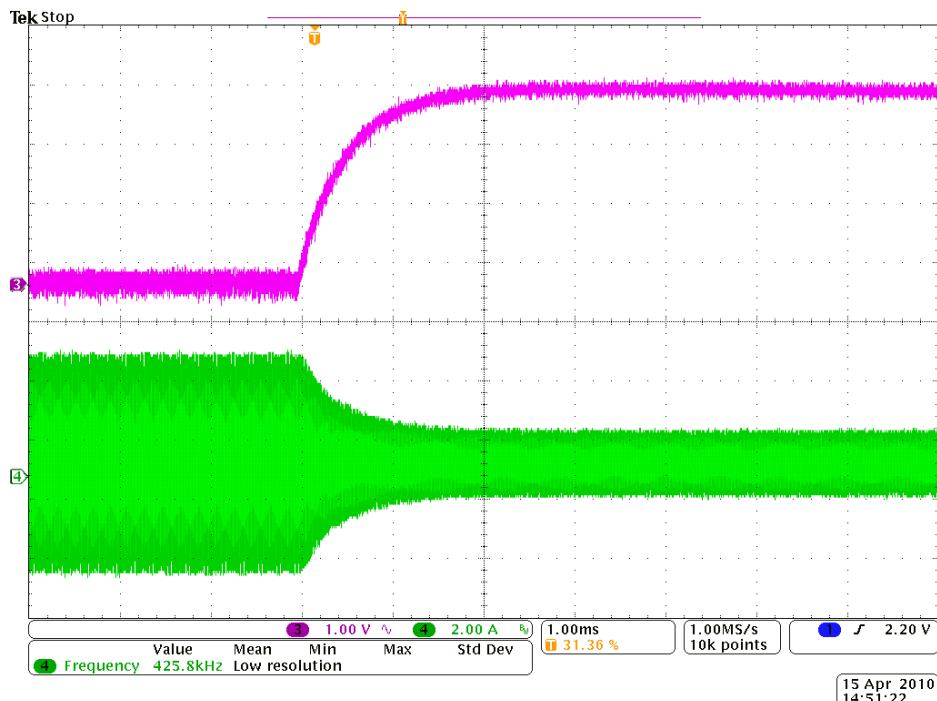


Figure 3-14: Output voltage  $V_O$  and primary current  $I_p$  during load transient from 9.6  $\Omega$  to 48  $\Omega$  (no PWM control)

For output load step change, Figure 3-14 shows the output voltage response (upper trace) during load transient when there is no PWM control. It can be seen that the voltage/current transition period can be completed within 2 ms. In order to compensate for the output voltage overshoot/undershoot, corrective control action must be applied within the first 0.5 ms of the transition period. In order to have fast response to the load transient, the tone decoding function is disabled and the control loop response time is increased to 0.1 ms.

The following criteria are used for the activation of this load transient control:

$$\begin{cases} \frac{\Delta I_{p,pk}}{I_{p,pk}} > \frac{1}{8}, \text{ or} \\ \Delta I_{p,pk} > 0.2 \text{ A} \end{cases} \quad (3.22)$$

The control of the output load transient is divided into two states, each with an distinctive controlling target. The first 1.0 ms belongs to the first control state. Its target is to reduce the output voltage overshoots/undershoots, and to reset the output voltage to the 24 V final level as close as possible. It is assumed that the rate of change of  $I_p$  is due to the change in output current consumption. For the case of output current increase, insufficient amount of current is supplied from the primary side and output voltage undershoot will occur. To recover the voltage level, an additional amount of current has to be provided. The PWM duty cycle is updated using

$$D \rightarrow D + K_1 (I_{p,pk})^{-1} \frac{\Delta I_{p,pk}}{\Delta t} \quad (3.23)$$

for state 1. In (3.23),  $K_1$  is a constant for data scaling,  $I_{p,pk}$  is the peak primary current level, and  $\frac{\Delta I_{p,pk}}{\Delta t}$  is the primary current level change since last update. The same control action will be done for the case of output current decrease, but this time the sign of  $\frac{\Delta I_{p,pk}}{\Delta t}$  will be negative and the control action is to reduce the primary current.

When the 1.0 ms control period ends, the second control state starts. The rate of change of current level is slower than that in state 1, and the control objective is to regulate the output voltage level without knowing the exact output voltage level. This is done by output loading estimation. First, the input impedance is calculated with the formula

$$Z_{in} = \frac{V_{s,pk}}{I_{p,pk}} = \frac{V_{IN}}{I_{p,pk}} \cdot \frac{4}{\pi} \sin\left(\frac{D\pi}{2}\right) \quad (3.24)$$

A table is prepared to map between  $Z_{in}$  and the peak primary current  $I_{p,est}$  for the output voltage at steady state. The PWM duty cycle is updated using

$$D \rightarrow D + K_2 Z_{in} (I_{p,est} - I_{p,pk}) \quad (3.25)$$

State 2 control will stop when  $I_{p,pk}$  is stable (variation  $< 0.2$  A) for three consecutive time slots (each 0.1 ms). Normal PWM control by tone decoding will then be used.

# Chapter 4 Experimental Results

In this chapter, measured waveforms of the power regulator at steady state are displayed. Dynamic responses of the transcutaneous power regulator under load transient and transformer gap separation variation are shown. Power efficiencies under different output loading conditions are measured and the results are displayed. It is followed by a power loss analysis. Suggestions for further improvement are given.

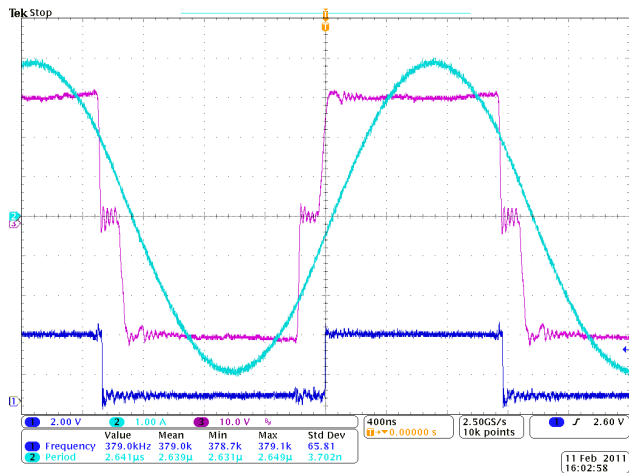
## 4.1 Essential Waveforms at Steady-State

Figures 4-1 and 4-2 show the measured waveforms for the phase-shifted full-bridge converter with gap separation of 10 mm and 20 mm, respectively. In each case, the supply voltage  $V_{IN}$  is 30 V and three loading conditions are shown. For all of the measured graphs, Ch 1 (in deep blue) is the PWM gate signal for Q1, which is the power MOSFET at the lagging leg of the full-bridge with connection to  $V_{IN}$  supply. Ch 2 (in light blue) is the primary inductor current  $I_P$ , and Ch 3 (in purple) is the voltage difference  $V_{AB}$  across the two legs. Figures 4-3 and 4-4 show the steady state waveforms at gap separation of 15 mm, with input supply voltage  $V_{IN}$  set to 30 V and 45 V, respectively. There is an additional Ch 4 (in green) waveform in Figures 4-3 and 4-4. It is the secondary side inductor current. The extra waveforms show the relationship between primary side control and the secondary side results.

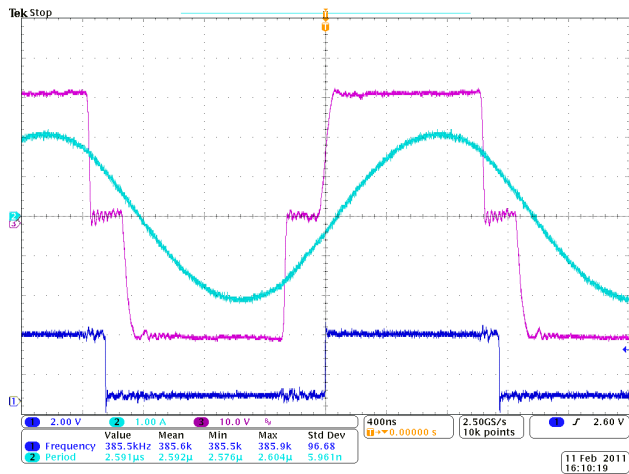
From the graphs, it can be seen that the primary current is essentially sinusoid in shape, with slight distortion for light loads. The current  $I_P$  is lagging behind the voltage  $V_{AB}$  waveform, providing charging current for ZVS condition.

Other observations from the waveforms are

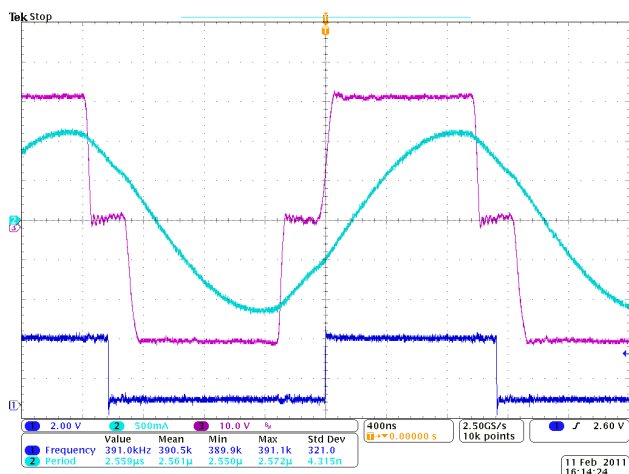
- Comparing between the two edges of the  $V_{AB}$  waveform, the leading edge is rising more slowly, due to the smaller amplitude of current  $I_P$ .
- The inductor current is reduced when the output loading  $R_L$  is increased.
- The phase difference between  $V_{AB}$  waveform and the current  $I_P$  increases as the loading  $R_L$  increases.



(a) Converter waveforms for 9.6  $\Omega$  output loading

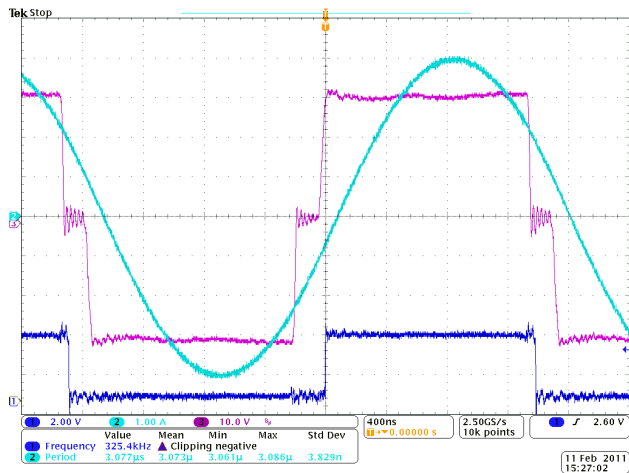


(b) Converter waveforms for 20  $\Omega$  output loading

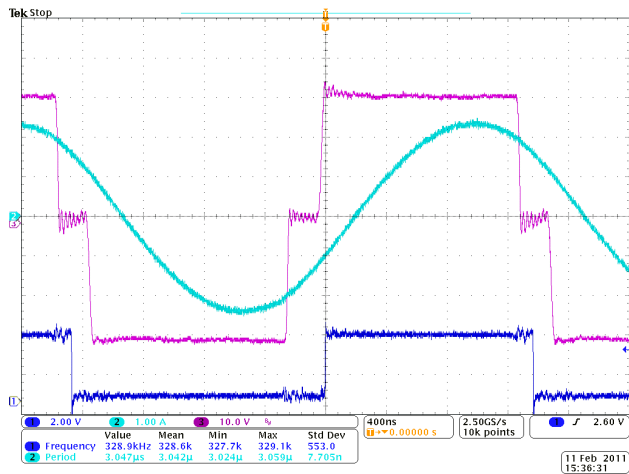


(c) Converter waveforms for 48  $\Omega$  output loading

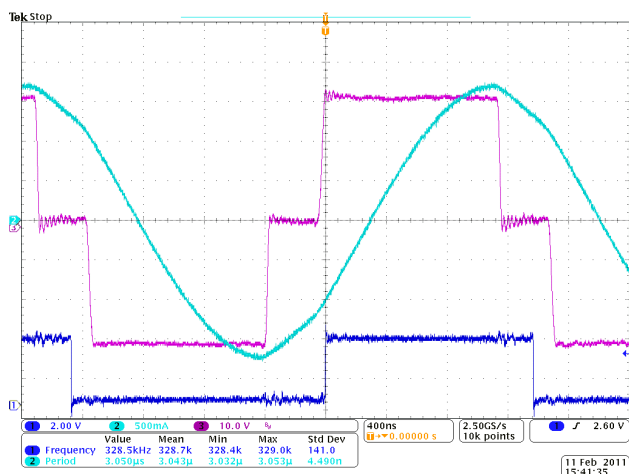
Figure 4-1: Converter waveforms at gap separation of 10 mm ( $V_{IN} = 30$  V)



(a) Converter waveforms for 9.6 Ω output loading

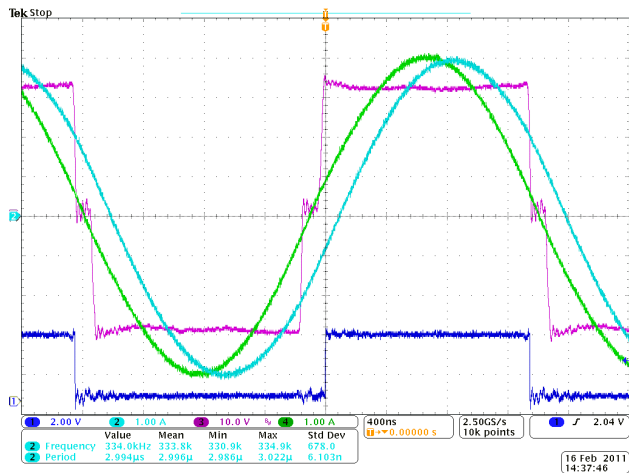


(b) Converter waveforms for 20 Ω output loading

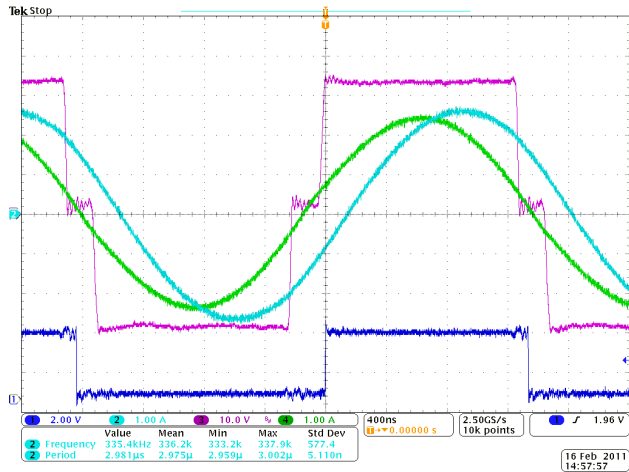


(c) Converter waveforms for 48 Ω output loading

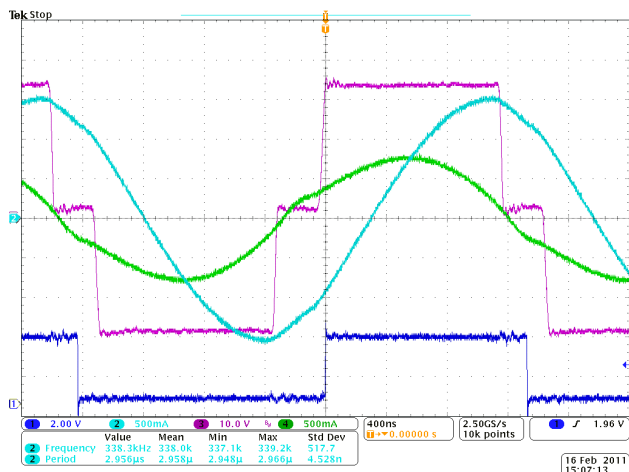
Figure 4-2: Converter waveforms at gap separation of 20 mm ( $V_{IN} = 30$  V)



(a) Converter waveforms for 9.6  $\Omega$  output loading

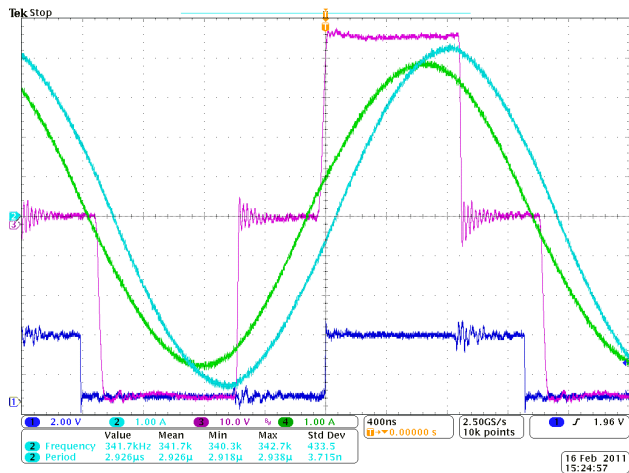


(b) Converter waveforms for 20  $\Omega$  output loading

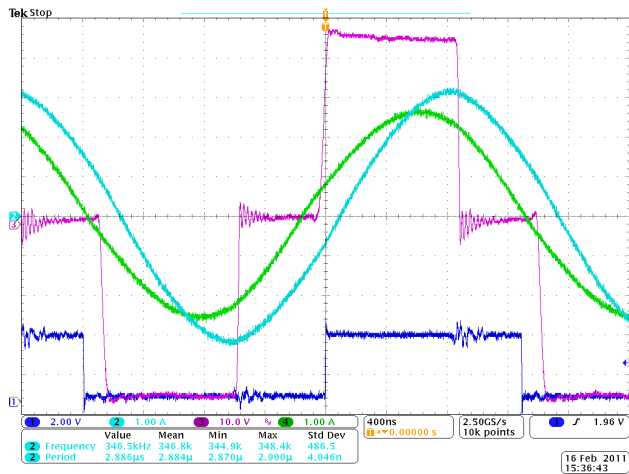


(c) Converter waveforms for 48  $\Omega$  output loading

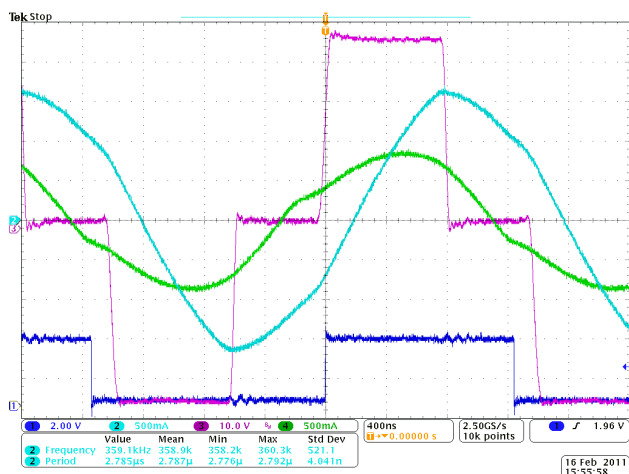
Figure 4-3: Converter waveforms at gap separation of 15 mm ( $V_{IN} = 30$  V)



(a) Converter waveforms for 9.6  $\Omega$  output loading



(b) Converter waveforms for 20  $\Omega$  output loading



(c) Converter waveforms for 48  $\Omega$  output loading

Figure 4-4: Converter waveforms at gap separation of 15 mm ( $V_{IN} = 45$  V)

For the effect of gap separation, the main difference appears in the inductor current  $I_p$ . The current's magnitude is largest at a gap separation of 20 mm, due to the increase of the magnetization current when coupling coefficient  $k$  is smaller. Such difference is becoming significant when output load  $R_L$  is large.

In Figure 4-3, when supply voltage  $V_{IN}$  is 30 V, the switching frequency is close to the resonant frequency. The secondary current  $I_S$  is in phase with the primary side  $V_{AB}$  waveform. In Figure 4-4, when supply voltage  $V_{IN}$  is 45 V, the duty ratio of the phase-shifted full-bridge converter is reduced to deliver the same power level to the secondary side. As a result, a higher switching frequency is set by the control loop in order to meet the ZVS condition. This higher frequency generates additional phase shift between the primary voltage  $V_{IN}$  and the secondary current  $I_S$ . The distortion in the secondary current  $I_S$  at output loading of 48  $\Omega$  is due to the changing of conduction path for the full-bridge diode rectifier when current  $I_S$  is changing its polarity.

## 4.2 Output Voltage Transient Response

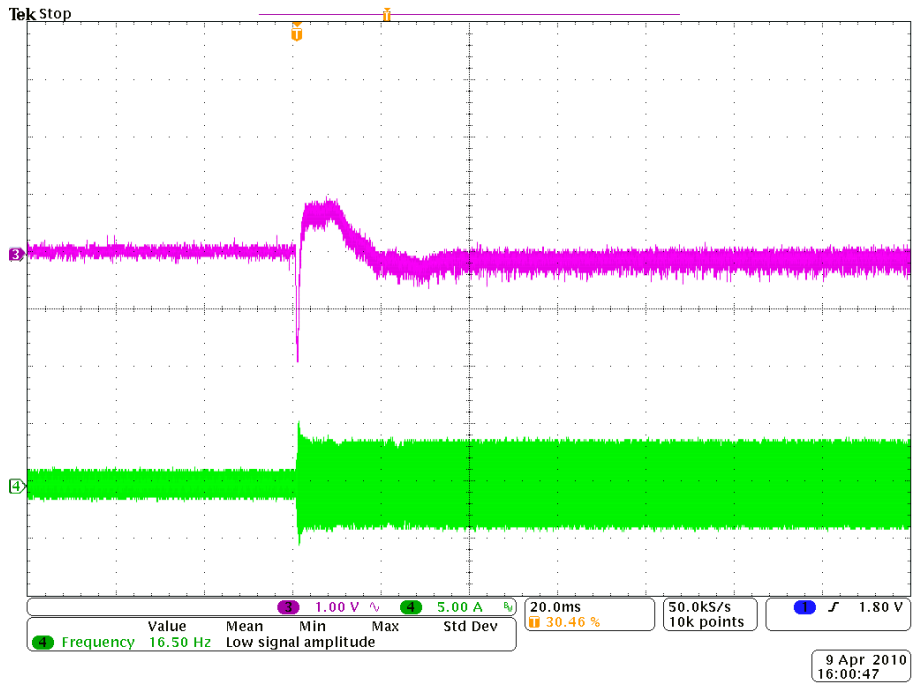
For the transient load responses, Figure 4-5 shows the measured results of the transcutaneous power regulator undergoing min-load-to-full-load and full-load-to-min-load changes at  $V_{IN} = 30$  V and gap separation of 10 mm. It can be seen that the output voltage can be recovered within 40 ms. By using the dynamic load transient control, the secondary output almost returns to its normal level within a few ms. Afterwards, the PI control takes over and the output voltage slowly converges to the final level. This is the typical response timing for control systems with unity-gain bandwidth of 30 Hz. For better system response timing, the control loop bandwidth has to be widened. However, since there are rechargeable batteries and other stages of power regulation at the secondary side of the artificial heart control system, the current converter response time should be acceptable.

It is undesirable for further speeding up of the dynamic control part of the output voltage response because the system may become unstable. For the PI response, the response time may be reduced by the following actions:

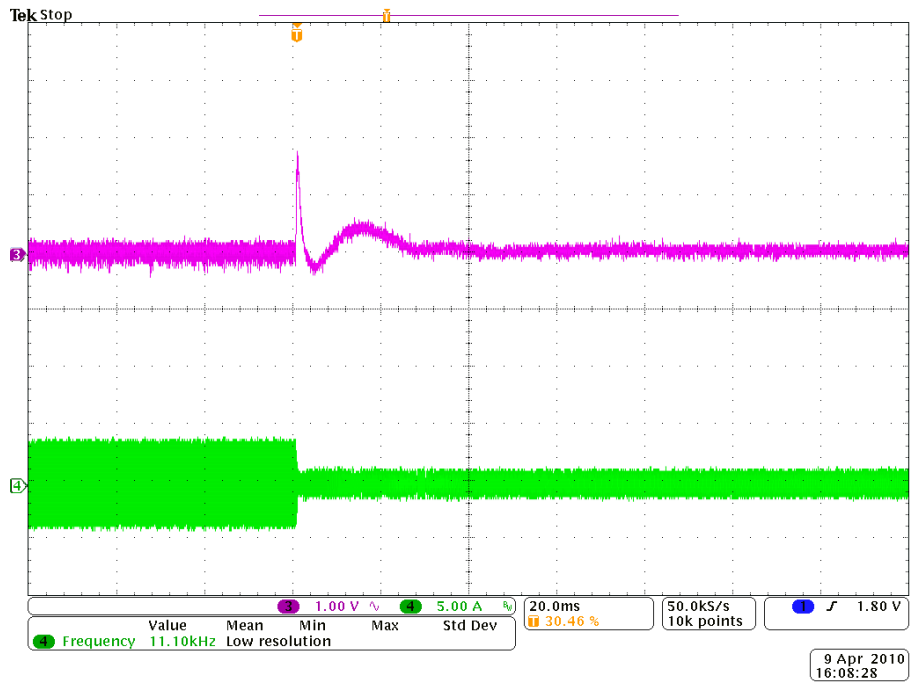
1. Increase the unity-gain bandwidth by using a smaller size output capacitor  $C_O$ . The double-pole position of the open-loop transfer function is proportional to  $\frac{1}{\sqrt{(L_1 + L_2)C_o}}$ .

If the output capacitance is reduced from 300  $\mu$ F to 100  $\mu$ F, then the new double-pole position will be at 1.7 kHz, and a new unity-gain bandwidth can be designed at 50 Hz. This is not a big improvement, though the system response will be faster.

- Replace the PI algorithm by a faster control algorithm, such as non-linear control, fuzzy or neural control algorithm.

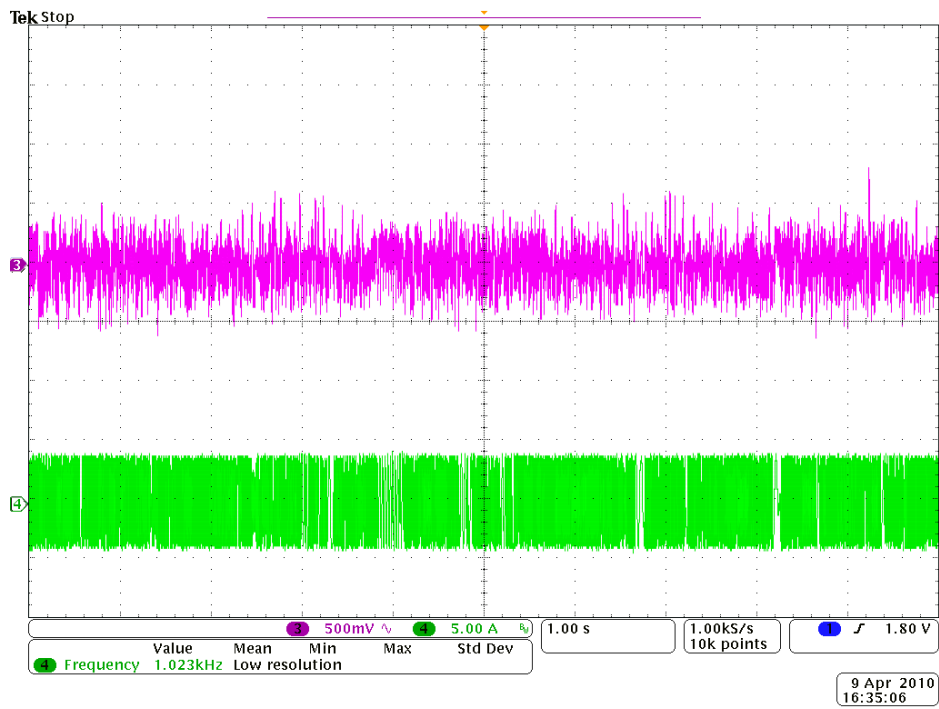


(a) Load change from 48  $\Omega$  to 9.6  $\Omega$

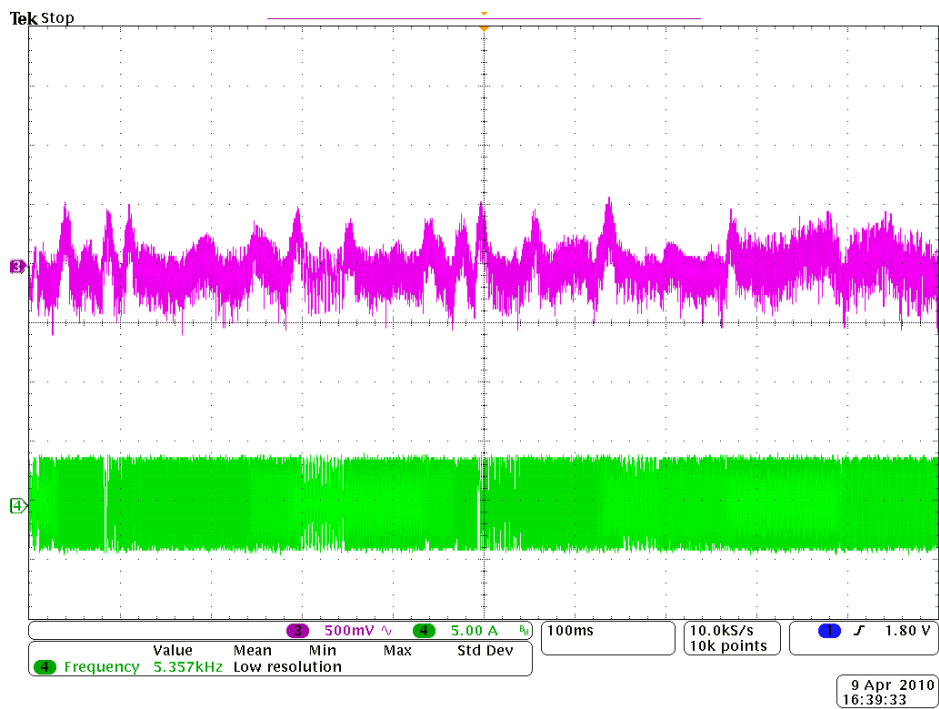


(b) Load change from 9.6  $\Omega$  to 48  $\Omega$

Figure 4-5: Output voltage response during load transient,  $V_{IN} = 30 \text{ V}$ ,  $k = 0.51$



(a) Output voltage during transformer gap separation width variation



(b) Expanded view of output voltage

Figure 4-6: Output voltage variation during transformer gap movement

### 4.3 Frequency Tracking With Moving Gap

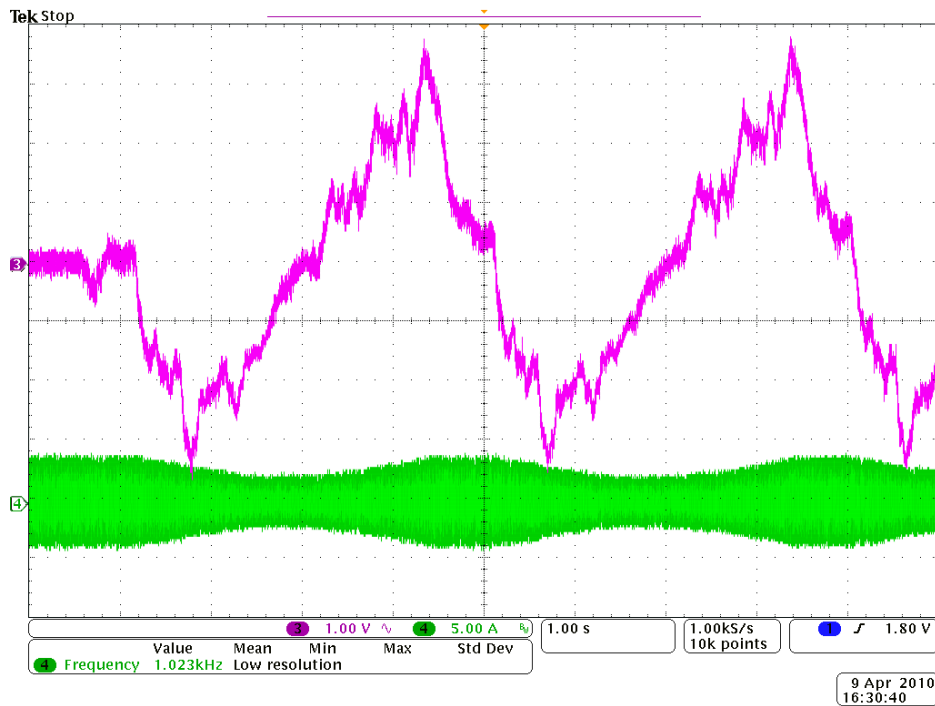


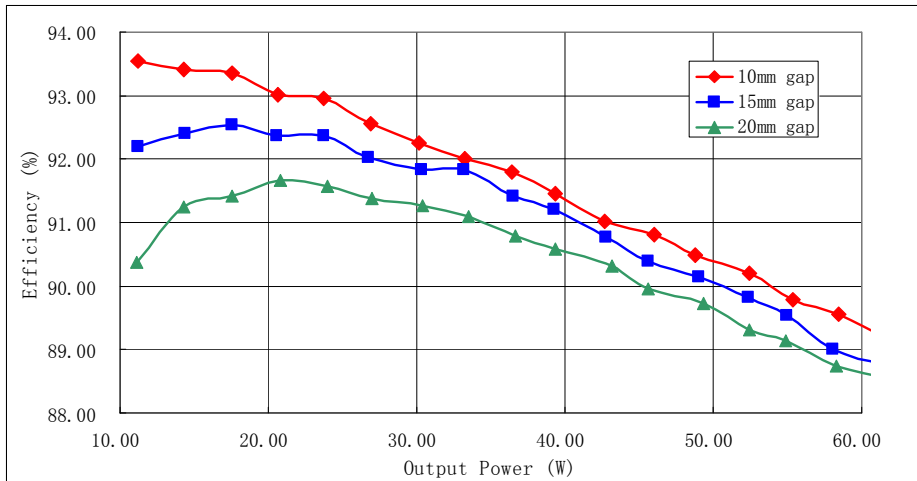
Figure 4-7: Output voltage when no frequency control is made during gap movement

Figure 4-6 shows the output voltage waveforms (upper trace) when the transformer gap is varying between the separation width of 10 mm and 20 mm. The lower trace is the primary current  $I_p$  waveform. The waveforms are taken under full-load condition and the gap movements are driven by a dc motor. One complete separation movement between 10 mm and 20 mm (and then moving backward) takes 4 seconds.

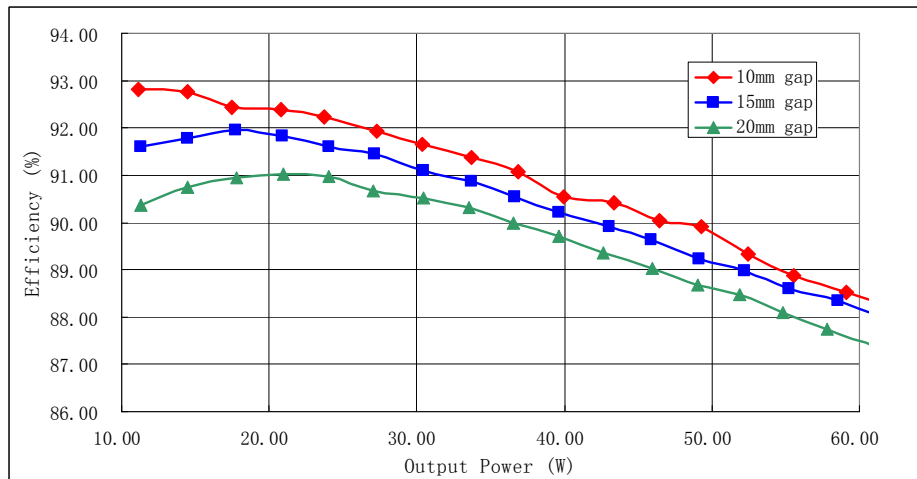
By changing the transformer gap separation from 10 mm to 20 mm, the coupling coefficient varies from 0.51 to 0.32. The corresponding series connected compensation networks will have the resonant frequency shifted from 377 kHz to 321 kHz in 2 seconds, and then shifted back from 321 kHz to 377 kHz in another 2 seconds. The correction of the resonant frequency change is done by the PLL control, which updates the PWM switching frequency according to the phase error between the primary current  $I_p$  and the PWM switching waveform. As seen from Figure 4-6, the output voltage variation is limited to within  $\pm 0.5$  V for the whole testing period, the frequency tracking control can be regarded as successful. At the same time, there is no visible variation in the amplitude of the primary current  $I_p$  waveforms. As a comparison, Figure 4-7 shows the output voltage waveform with the same dc motor driving the transformer gap variation, but the PWM and frequency control

functions are disabled. There is a 7 V peak-to-peak output voltage variation, and this amplitude is much larger than that under frequency control.

#### 4.4 Converter Efficiency



(a)  $V_{IN} = 30\text{ V}$



(b)  $V_{IN} = 45\text{ V}$

Figure 4-8: Measured converter efficiency

The measured efficiency of the regulator at  $V_{IN} = 30\text{ V}$  and  $45\text{ V}$  for different transformer gap separations are shown in Figure 4-8. It can be seen that the power converter can maintain its power efficiency for gap separation as large as 20 mm. For applications of the power supply in artificial hearts, the power requirement is from 15 W to 35 W, and the

power regulator attends the highest efficiency for this range. The design of our power converter can deliver an output power up to 60 W, which provides additional margin for extra power consumption requirement inside the human body. Another reason for the additional power margin is for exception handling. When materials or devices with magnetic properties are placed near-by, there may be distortion of the magnetic field generated by the primary side of the transcutaneous transformer. The distortion in the inductive linkage will weaken the power transfer capability of the converter and a higher output power from the primary side is needed.

## 4.5 Loss Analysis

Six major types of losses can be identified in the transcutaneous power regulator:

- (a) Forward diode voltage drop ( $\times 2$ ) in the full bridge rectifier circuit at the secondary: The rectifier converts the ac resonant voltage into the dc output voltage. Since two diode forward voltages are involved, this is a significant part of the power loss.
- (b) Conduction loss in the current flowing paths: The series resistances in the primary path are the MOSFET's  $r_{DS(on)}$  resistance ( $\times 2$ ) in the full-bridge power MOSFETs, the ESRs in the primary inductor coil and in the resonant capacitor  $C_p$ . Within a switching time period, current will flow through the anti-parallel diodes across the associated MOSFETs under some operating modes. More detailed explanations are given in the calculation of part (c) power loss. The change of current path will affect the conduction loss calculation. However, since the MOSFET's  $r_{DS(on)}$  resistance is relatively small, for simplicity, it can be assumed that two MOSFETs are on for the whole cycle period. For the secondary path, the series resistances are the ESRs in the secondary tank circuit,  $L_s$  and  $C_s$ . The secondary current path also includes the diode bridge, but the loss is already included in part (a) loss, so it is not included here to avoid duplication. In the power supply, the output load is in the range from  $9.6 \Omega$  to  $48 \Omega$ , which is small in resistance value. In order to minimize the power loss, care should be taken to reduce the current path series resistances.
- (c) Power losses in the primary current flowing through the anti-parallel diodes across the power MOSFETs in the full-bridge circuit: This is a special form of conduction loss. When the associated MOSFET is off or when current is flowing in the reverse direction, the anti-parallel diode will conduct. Since the forward diode voltage drop is larger than the MOSFET's  $r_{DS(on)}$  voltage drop, it is calculated independently.

- (d) Switching loss in the power MOSFETs: There are turn-on switching losses and turn-off switching losses for all four MOSFETs, and the total switching loss is proportional to the switching frequency  $f_S$ . Due to ZVS at turn-on and snubber effect by the MOS capacitances at turn-off, the switching losses have been tuned to a minimal value.
- (e) Output capacitor's ESR loss due to AC current flow: The current to the output load is a dc current of magnitude  $I_O$ , but the current in the secondary path is an ac current of  $\frac{\pi}{2} I_O \sin(\omega t)$  and the output capacitor will provide the current which is the difference between the two currents. There is in-flow and out-flow of current within one switching cycle. When there is ESR in the output capacitor, there will be power loss due to the  $\Delta I_O$  flow.
- (f) Hysteresis loss in the transformer coils when magnetic material such as ferrite is used as core in the wiring: Due to nonlinear B-H response property of the magnetic material, extra energy is required to generate a complete sweep of the B-H curve. The hysteresis loss is given by

$$P_{\text{hyst}} = k_h V_C f_S (B_{\text{max}})^2$$

where  $k_h$  is the hysteresis loss constant for the material,

$V_C$  is the volume of the core ( $\text{cm}^3$ ),

$f_S$  is the switching frequency (Hz), and

$B_{\text{max}}$  is the maximum excursion of the operating flux density

In our system, air core transformer coils are used, and there is no hysteresis loss.

For the part (a) loss, it is assumed that there are always two diodes being biased at forward direction and their forward voltage ( $V_F$ ) drops are constant and equal to  $V_F$  at output load current. According to datasheet of Vishay's V10P10 schottky rectifier,  $V_F$  at 0.5 A (25°C) is 0.35 V, and  $V_F$  at 2.5 A (25°C) is 0.45 V.

$$\text{Power loss at 0.5A} = (0.35 \times 2) \times 0.5 = 0.35 \text{ W}$$

$$\text{Power loss at 2.5A} = (0.45 \times 2) \times 2.5 = 2.25 \text{ W}$$

For the part (b) losses, according to datasheet for Vishay's Si7852ADP N-channel MOSFET, the  $r_{\text{DS(on)}}$  resistance is 17 mΩ. For other parts of the calculation, they are dependent parameters of the switching frequency and the coupling coefficient. So, calculation will be done for two separate cases. In the first case, for 10 mm transformer gap

separation, when the coupling coefficient  $k$  value is large, the circulation current  $I_P$  is small, but the resonant frequency is close to 400 kHz. In the second case, for 20 mm transformer gap separation, with a larger value of  $k$ , the circulation current  $I_P$  is large, but the resonant frequency is close to 300 kHz. The measured ESRs for the transformer coils at 300 kHz and 400 kHz can be found in Table 3-4, and the resonant frequencies corresponding to gap separations of 10 mm and 20 mm are 377 kHz and 321 kHz, respectively. It is assumed that the actual switching frequency is 2% above the resonant frequency, and switching frequencies of 384 kHz and 327 kHz are taken for the 10 mm and 20 mm transformer gap cases. As seen from Table 3-4, the equivalent series resistance (ESR) in the inductor coil increases by more than 20% from 300 kHz to 400 kHz, and the interpolation by log scale is used to calculate their resistance values and the results are tabulated in Table 4-1. For 10 mm transformer gap separation, the switching frequency is assumed to be 384 kHz, and the primary and secondary current path series resistances are

$$R_{PRI} = 17 + 566 + 2 \times 17 = 617 m\Omega$$

$$R_{SEC} = 20 + 394 = 414 m\Omega$$

For 20 mm transformer gap separation,  $f_s$  is assumed to be 327 kHz, and

$$R_{PRI} = 19 + 496 + 2 \times 17 = 549 m\Omega$$

$$R_{SEC} = 22 + 350 = 372 m\Omega$$

Table 4-1: Series Resistances for Resonant Tank Components

	327 kHz (20mm gap)	384 kHz (10mm gap)
$C_P$	19 mΩ	17 mΩ
$C_S$	22 mΩ	20 mΩ
$L_P$	496 mΩ	566 mΩ
$L_S$	350 mΩ	394 mΩ
$L_M$	10.81 μH	17.07 μH

At the secondary side, the circulation ac current is related to the output load current by [133]

$$I_{S(rms)} = \frac{\pi}{2\sqrt{2}} I_o \quad (4.1)$$

and the conduction loss at the secondary current path is

$$\frac{1}{2} R_{SEC} \cdot I_{S(rms)}^2 = \frac{\pi^2}{16} R_{SEC} \cdot I_O^2 \quad (4.2)$$

The primary circulation current can be approximated by the current close to the resonance condition. Using a scale factor of  $\sqrt{8}/\pi$  for ac voltage to ac (rms) voltage conversion, the real part and imaginary parts of the ac voltage as seen by the transformer secondary (without the  $L_2$  leakage inductance) are

$$\begin{aligned} V_{S,r} &= \frac{\sqrt{8}}{\pi} (V_O + 2V_F) + R_{SEC} \cdot I_{S(rms)} \\ &= \frac{\sqrt{8}}{\pi} (V_O + 2V_F) + \frac{\pi}{\sqrt{8}} R_{SEC} \cdot \frac{V_O}{R_L} \\ &= \frac{\sqrt{8}}{\pi} \left( 1 + \frac{R_{SEC}}{R_E} \right) V_O + \frac{4\sqrt{2}}{\pi} V_F \end{aligned} \quad (4.3)$$

$$V_{S,i} = 2\pi f L_2 - \frac{1}{2\pi f C_S} \approx 2 \cdot 2\pi \Delta f L_2 = 4\pi \Delta f L_2 \quad (4.4)$$

where  $R_E$  is the effective ac load resistance, and  $\Delta f$  is the difference between the switching frequency and the secondary resonant frequency. The voltage across the transformer  $L_M$  terminal at the primary is

$$V_{Lm} = \frac{1}{n} \sqrt{V_{S,r}^2 + V_{S,i}^2} \quad (4.5)$$

Assuming that the  $L_M$  terminal current is 90° out of phase with the secondary current, the conduction loss at the primary current path can be calculated as

$$\frac{1}{2} R_{PRI} \cdot \left( \left( \frac{V_{Lm}}{\omega L_M} \right)^2 + (n I_{S(rms)})^2 \right) = \frac{1}{2} R_{PRI} \cdot \left( \frac{V_{S,r}^2 + V_{S,i}^2}{n \cdot (2\pi f L_M)^2} + \frac{n^2 \pi^2}{8} I_O^2 \right) \quad (4.6)$$

For transformer turns ratio  $n = 29/30 = 0.9667$ , the results of the estimated primary current and the corresponding losses are shown in Table 4-2.

The part (c) anti-parallel diode conduction losses calculation is based on the waveforms shown in Figure 4-9. Under operating modes 2 and 5,  $V_{AB} = 0$ , the left and right legs of the full-bridge are tied either both to supply voltage  $V_{IN}$  or both to the ground level. One of the full-bridge legs will have reverse current flowing through it. So, one anti-parallel diode is conducting. Under operating modes 3 and 6, the current itself is negative. Thus, two anti-parallel diodes are conducting. Since the power losses are the same for operating modes 2 and 5, and also for operating modes 3 and 6, only two operating modes calculations are required.

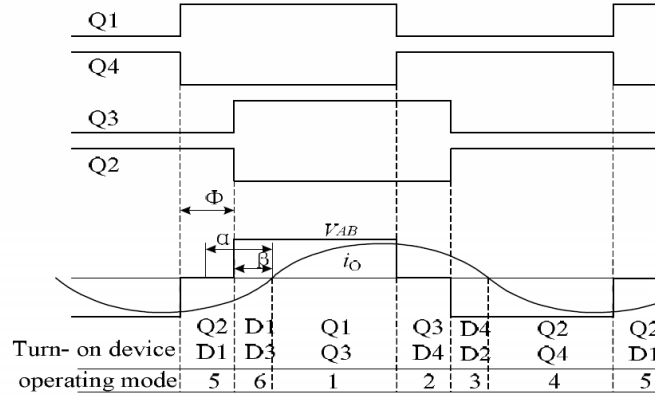


Figure 4-9: PSFB PWM operating modes for resonant converter [148]

The magnitude of the primary current  $I_p$  has been calculated in part (b), and the conduction angle for each operating mode can be obtained by waveforms captured by the oscilloscope. The power loss for operating mode 6 is

$$P_1 = \frac{1}{\pi} \int_0^\beta 2V_F I_{p,pk} \sin \theta d\theta = \frac{2V_F I_{p,pk}}{\pi} (1 - \cos \beta) \quad (4.7)$$

The power loss for operating mode 5 is

$$P_2 = \frac{1}{\pi} \int_\beta^{\beta+\phi} V_F I_{p,pk} \sin \theta d\theta = \frac{V_F I_{p,pk}}{\pi} (\cos \beta - \cos(\beta + \phi)) \quad (4.8)$$

For the part (d) switching losses, since the ZVS condition is automatically set when the switching frequency control algorithm is taking action, all four MOSFETs are assumed to be turned on at zero voltage (diode forward voltage  $V_F$  in reality), and the turn on switching losses can be neglected. At turn off, the voltages  $V_{DS}$  of all four MOSFETs are kept at low voltage level by the parasitic capacitances and the drain-source voltage rises only after the MOSFETs are in the off state. So the MOSFETs' turn-off losses are all small. In summary, due to ZVS condition, the turn on losses are small; and due to the holding of MOSFETs'  $V_{DS}$  during the turn off period, the switching off losses are also small.

For the part (e) output capacitor ESR losses, the power loss can be calculated as

$$P_{ESR} = \frac{1}{\pi} \int_0^\pi r_{ESR} \cdot I_O^2 \left( \frac{\pi}{2} \sin \theta - 1 \right)^2 d\theta = r_{ESR} \cdot I_O^2 \left( \frac{\pi^2}{8} - 1 \right) \quad (4.9)$$

where  $r_{ESR}$  is the equivalent series resistance of the output capacitor, and  $I_O$  is the DC output load current. In the power supply design, Panasonic Series FC type (low ESR type) aluminium electrolytic capacitor (330  $\mu$ F, 50 V) was selected as the output capacitor, and the impedance at 100 kHz is 0.063  $\Omega$ . The results of power loss calculation are shown in Table 4-2.

Note that in Table 4-2, the percentage figures in the parentheses are relative to the output load power, not the total input power ( $= P_{out} + Loss$ ). The loss calculations are done for other loading values, and the results are shown in Figure 4-10. It can be seen that the estimated power losses are generally lower than the measured power losses by 1% to 2%. The additional losses may be due to the following factors:

- The calculation done here does not take the thermal effect into consideration. When the power regulator is being heated up, the forward diode voltage  $V_F$  will decrease but the series resistance of the inductor coils will increase.
- The parasitic capacitances and wiring resistance on the prototype board will induce additional losses to the power regulator.
- Both primary and secondary inductor currents are assumed to be sinusoidal, but their actual waveshapes are non-ideal. This means that there are higher frequency harmonic components in the flowing current, which will incur more power losses because the Litz wire ac resistances are higher at higher frequencies.
- Another source of inaccuracy of the error estimation comes from the deviation from the ideal resonant frequency operation. In reality, the switching frequency is higher than the resonant point, and this off-resonance condition will degrade the quality factor of the resonant tanks.

Disregarding the under-estimation of 1% - 2% of power losses, the estimated power efficiency curves at two different gap separations follow closely the measured efficiency curves.

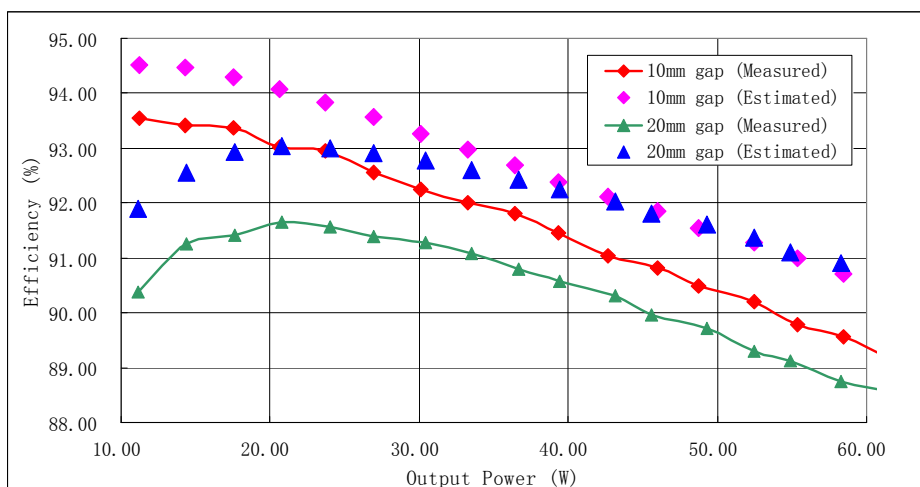


Figure 4-10: Loss analysis of the transcutaneous power regulator at  $V_{IN} = 30$  V and two different gap separations

Table 4-2: Power Losses Calculation

	$R_L = 9.6\Omega$ (60W)	$R_L = 48\Omega$ (12W)
Gap = 10mm, $f_s = 384$ kHz		
Primary current $I_{P,rms}$	2.75 A	0.79 A
Secondary bridge diode loss	2.250 W (3.75%)	0.350 W (2.92%)
Primary conduction loss	2.336 W (3.95%)	0.191 W (1.95%)
Anti-parallel diodes power loss	0.078 W (0.13%)	0.085 W (0.71%)
Secondary conduction loss	1.596 W (2.65%)	0.064 W (0.55%)
Output capacitor ESR loss	0.092 W (0.15%)	0.004 W (0.03%)
Total estimation loss	6.352 W (10.59%)	0.693 W (5.77%)
Measured power loss	7.272 W (12.12%)	0.834 W (6.95%)
Gap = 20mm, $f_s = 327$ kHz		
Primary current $I_{P,rms}$	2.90 A	1.18 A
Secondary bridge diode loss	2.250 W (3.75%)	0.350 W (2.92%)
Primary conduction loss	2.308 W (4.06%)	0.381 W (4.24%)
Anti-parallel diodes power loss	0.094 W (0.16%)	0.216 W (1.80%)
Secondary conduction loss	1.434 W (2.39%)	0.057 W (0.48%)
Output capacitor ESR loss	0.092 W (0.15%)	0.004 W (0.03%)
Total estimation loss	6.178 W (10.30%)	1.0084 W (8.40%)
Measured power loss	7.751 W (12.92%)	1.235 W (10.29%)

From Table 4-2, it can be seen that the current path conduction losses and diode forward voltage drops in the secondary full-bridge rectifier circuit are the two major losses in the regulator. In order to further improve the power efficiency, these losses are the focus of attention. The system efficiency can be improved by using synchronous rectifiers to replace the full-bridge rectifier. The voltage drop  $V_F$  is 0.35 V ( $\times 2$ ) for 0.5 A output current and 0.45

V ( $\times 2$ ) for 2.5 A output current. If the total voltage drop can be reduced to 0.1 V, then the power efficiency can be improved by 2.5% (0.5 A) and 2.9% (2.5 A). For the conduction loss, the amplitude of the secondary side current is fixed by the output load current. Thus, very little improvement can be done on the secondary side, but for the primary side, the primary current  $I_p$  may be reduced by using a higher transformer turns ratio.

# Chapter 5 Conclusion

## 5.1 Summary

In this thesis, detailed design procedures for a transcutaneous power regulator with high efficiency are presented. The theoretical operating principles are introduced, and the system design using digital signal processor (DSP) as a primary side controller and an 8-bit microcontroller at the secondary side is given. Control algorithms for switching frequency adaptation and output voltage regulation are given. In order to give fast response to load transient, a special control algorithm is added in the software with only primary current monitoring. With the help of this transient control, the secondary output voltage can be recovered in a short time.

A phase-shifted full-bridge (PSFB) circuit is used as the driving circuit, which can achieve ZVS turn on for all MOSFET drivers. Double-tuned resonant circuits are used to compensate for the leakage inductances in the transcutaneous transformer for best power transfer through inductive coupling at high frequencies (300 kHz to 400 kHz). Power losses are minimized by using Litz wires for the transformer coils and rectifier diodes with small forward voltage drop.

A SPICE macromodel is developed for the power regulator circuit, and it provides fast simulation of the system. Based on the SPICE macromodel, the open-loop response of the TET circuit is obtained and a digital PI closed-loop control is derived for stable output voltage regulation.

## 5.2 Contributions

A new control method is utilized for transmission of the secondary output voltage information using the same transformer for power and information. While other analog solutions need multi-chips for a complete system design: (i) PWM control, (ii) PLL frequency tracking, (iii) analog comparator for reference current level trigger, and (iv) extra hardware for secondary voltage sensing, the solution described in this thesis uses only a single-chip DSP to implement all functions, resulting in a simpler hardware design. The frequency band in the range of 20 kHz to 30 kHz is used for information transmission with frequency modulation. A summary of the major contributions is as follows.

1. By introducing a SPICE macromodel for fast simulation of the double tuned resonant circuit, construction of system response curves can be performed conveniently to assist the design of the control for voltage loop stability. The SPICE macromodel also helps the selection of signal tone frequency band for secondary voltage information transmission.
2. All complex functional modules, namely, PWM control, PLL frequency tracking and DSP tone detection, have been integrated into a single-chip DSP. This results in a simple hardware solution for the transcutaneous power regulator design.
3. A practical solution for secondary voltage feedback has been proposed and confirmed by hardware implementation.
4. A loss analysis has been performed, which provides a good approximation of the system losses for wide load ranges. The conduction loss and the rectifier full-bridge forward voltage drop have been identified as the two major losses in the system.

### **5.3 Suggestions for Future Work**

Further research works can be done for the transcutaneous power regulator design, particularly for the artificial heart systems. Some suggestions are listed below.

#### **5.3.1 Simpler Control Algorithm – No PWM Control**

In order to achieve full system control at the primary side, a complex control software program that integrates (i) switching frequency control with PLL algorithm, (ii) output voltage regulation with tone signalling, (iii) PI algorithms for control-loop stabilization, and (iv) output voltage transient control, is needed. In real situations, there are rechargeable batteries at the secondary side circuit that acts as a buffer to the coupled output voltage fluctuation, and the 24 V output voltage will be further down converted to a lower voltage for driving the motor pump and the heart controller system. Thus, the sole responsibility of the primary controller in the power transfer device is to track the resonant frequency of the double-toned system and to make sure that power is transferred to the secondary side at maximum efficiency.

A simpler control algorithm can be used in the new system design (which may not be called power regulator) such that no secondary output voltage regulation is necessary. Full duty ratio (i.e., no PWM control) will be used for achieving the best power transfer ratio. Also, the phase information in the primary current  $I_p$  will be used for switching frequency

control. Since there is no need for periodic secondary output voltage information, the 20–30 kHz frequency band can be used as information channel for the artificial heart controller. Such information includes body temperature, heart beat rate, blood flow rate, and other patient's body status information. Additional information includes the rechargeable battery status and the output voltage level. All these information can be transmitted at a much lower rate than the original output voltage information, so the current channel bandwidth is sufficient for practical application. With careful design, a two-side communication channel can be built.

### **5.3.2 Data Logging with PC and Search for Better Control Algorithm**

The primary controller DSP in use has a hardware UART module for serial communication with a computer or PC. The status information of the control software can thus be sent to the PC side for data logging. An optimization algorithm such as a genetic algorithm and neural network control method may be used to search for alternative algorithms for better system response and better switching frequency tracking.

The transcutaneous power regulator is actually a nonlinear system with switching frequency  $f_s$ , duty ratio  $D$ , coupling coefficient  $k$ , and input voltage  $V_{IN}$  as parameters. This nonlinear system may be transformed into a linear system by means of state feedback and nonlinear transformations. After feedback linearization, a system can be dealt with by linear controller design. Feedback linearization by means of neural networks which allow the identification of nonlinear models without the complicated and costly development of models based on physical laws is a possible approach. For practical implementation, a dynamic or recurrent neural network, which has an inherent property to mimic nonlinear dynamic systems, may be a promising candidate.

### **5.3.3 AC Input Power Regulator**

For much of the literature on the design of artificial heart power regulators, the systems are designed for DC-DC operation, and the input side is a regulated dc level. However, for day-to-day operations, input power from the ac mains is unavoidable. The voltage provided by the pre-regulator is high (close to 400 V DC), and this voltage level may not be suitable for direct use. Also, components with high breakdown voltage are expensive and their  $r_{DS(on)}$  or ESR resistances are usually high. Although the primary transformer coil is placed outside the human body, it is still in touch with the patient's skin. Thus, an isolation

transformer between the ac main and the primary tank circuit is required. The isolation transformer may be used to step down the pre-regulated voltage to 80 V – 100 V. At this range of input voltage, it is easier to design for driving MOSFETs. At the same time, the transcutaneous transformer may be designed with special features that enhance the power efficiency:

- The turns ratio will be  $m : 1$ , where  $m$  is between 2 to 3. In this case, the secondary coil will consist of fewer turns and it can be constructed for smaller size. For the primary coil, it will have more turns in the wiring. A smaller secondary coil is more favourable since it is implanted inside the human body.
- A smaller coil implies a smaller series resistance, and less heat loss will be generated inside the human body. For the primary side, the coil's inductance will increase due to the increase in the number of turns, so will the inductance  $L_M$ . At the same time, the conduction loss at the primary side may decrease. The secondary circulation current is fixed by the output loading condition, and a smaller primary circulation current (reduced by a ratio of  $m$ ) will be seen. Meanwhile, the effective voltage across the inductance  $L_M$  will also be reduced by a factor of  $m$ , and the current  $I_{Lm}$  will also decrease.
- The primary DSP controller may also be functioned as a power factor controller (PFC), and a single chip solution for the primary side hardware control is possible.

#### **5.3.4 Testing with Non-Resistive Load and Battery Charging**

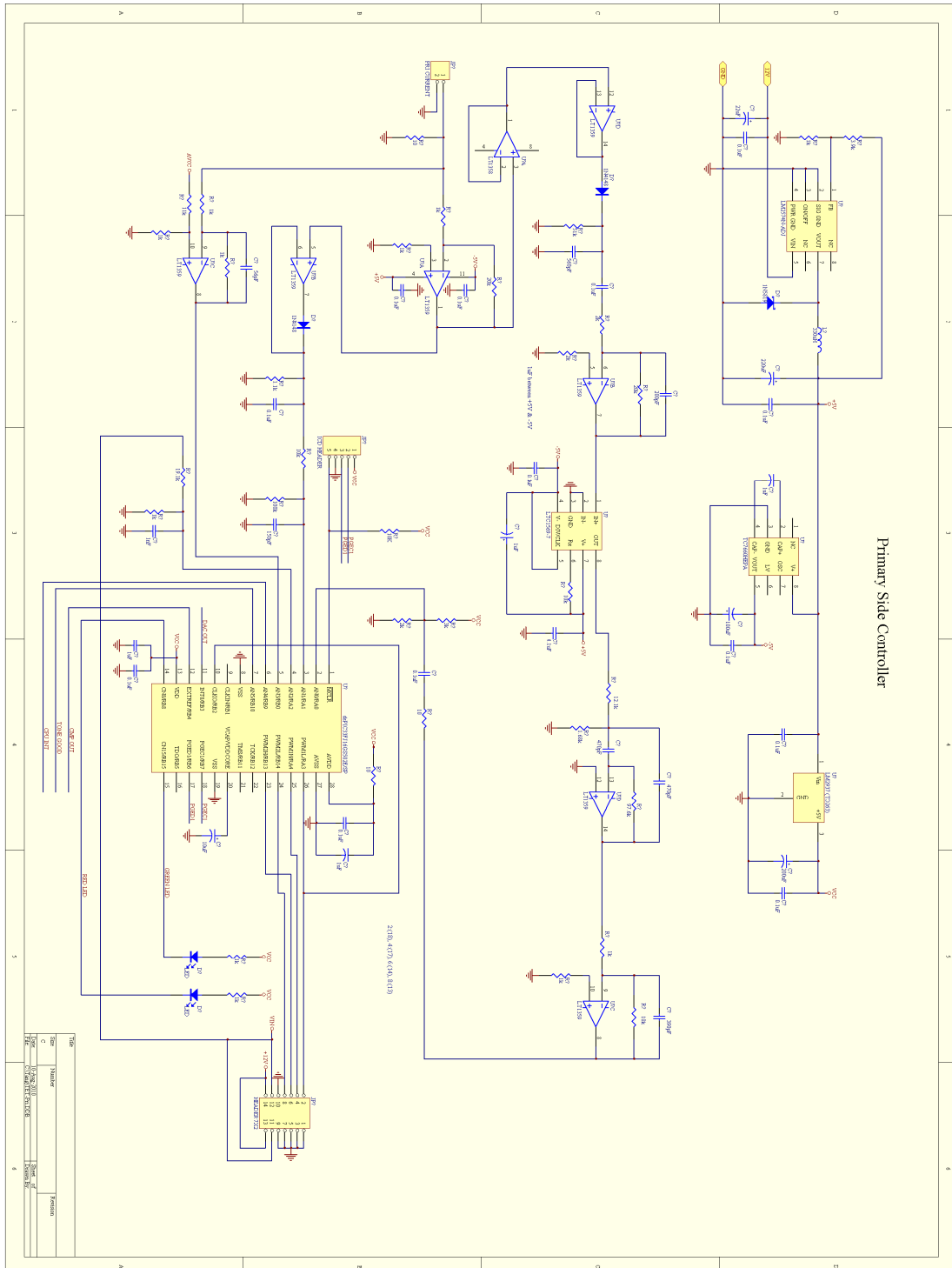
At the secondary side of the artificial heart system, there is a mechanical mini-pump that circulates the blood flow inside the human body. The blood flow rate is regulated by the heart controller. Since the pumping operations may have different load current behaviours that are different from a resistive load, a detailed study on the pumping load and the primary current phase shift relationship is necessary. The primary controller should properly control the switching frequency so that it is close to the resonant point under all loading conditions. Besides, there are rechargeable batteries at the secondary side of the whole artificial heart system, and the charging of the secondary battery may change the control mechanism at the primary side.

### **5.3.5 Secondary Side Rectification and Tone Signalling using Synchronous Rectifiers**

As seen in the power loss analysis (Section 4.4), the forward diode voltage drop in the secondary side full-bridge rectifier circuit accounts for 2 – 3% of power loss in the TET system. This will generate a lot of waste heat inside the human body. The power loss can be minimized by using synchronous rectifiers to replace the functions of the full-bridge circuit. Besides, the hardware system is now sending the secondary side output voltage to the primary using a  $\pm 0.1$  V square pulse tone signal by using a 60:1 coupling transformer. By a proper 'on'/'off' control of one of the synchronous rectifiers, the same ac tone signal can be generated without the coupling transformer.

Furthermore, since an artificial heart system will also transmit data telemetry information at periodic time intervals, the tone signalling protocol may be improved to add time interval for extra information transmission. If the UART serial link software for communication between the primary side DSP and PC is completed, then the information received from the system secondary can be displayed on the PC in real time to show the data logging function. In addition, an ECG measurement circuit can be built using the hardware resource from the secondary side controller, and an artificial heart operating system can be partially simulated.

# Appendix 1 Circuit Diagram of Primary Side Controller Board







## Appendix 3 SPICE Circuit File for Line-to-Output Response Generation (Gap = 10 mm)

```

TET bode plot(k-10mm_bode)
*****
*
.param L1=16.22e-6
.param L2=15.99e-6
.param Lm=17.07e-6
*
.param Rp=12e-3
.param Rs=15e-3
.param Rm=12e-3
*
.param Cp=10.99e-9
.param Cs=11.09e-9
*
.param Co=330e-6
.param Resr=10e-3
*
*****
*
* RL may be 9.6, 20, 30, or 48
*
.param RL=48
*
*****
*
.param Vin=30
.param VFS=377e3
*
*****
*
* Input Section
*
Vfs nfs 0 dc {VFS}
Rfs nfs 0 1Meg
Bws nws 0 v=(2*pi*v(nfs))
Rws nws 0 1Meg
*
Vs ns 0 dc {Vin} ac 1
*Vs ns 0 dc {Vin}
Bis ns 0 i={4/pi}*sqrt(i(Vir)*i(Vir)+i(Vii)*i(Vii))

```

```

*
*****
*
* Real part circuit
*
* <Vs-r>=0
Bir nir1 0 v={L1}*v(nws)*i(Vii)
+ - v(nvr)
Rir nir1 nir2 {Rp}
Vir nir2 nir dc 0
Lir nir nlmr {L1} ic=0
*
Bivr 0 nvr i={Cp}*v(nws)*v(nvi) + i(Vir)
Cpr nvr 0 {Cp} ic=0
Rvr nvr 0 1Meg
*
Bvlmr nlmr nlmr2 v=-{Lm}*v(nws)*i(Vimi)
Vimr nlmr2 nlmr3 dc 0
Rmr nlmr3 nlmr4 {Rm}
Lmr nlmr4 0 {Lm} ic=0
*
Bvl2r nlmr nl2r1 v=-{L2}*v(nws)*i(Vi2i) + 4/pi*v(no)*i(Vi2r)*V(n_ino)
+ v(nvsr)
Vi2r nl2r1 nl2r2 dc 0
Rsr nl2r2 nl2r3 {Rs}
L2r nl2r3 0 {L2} ic=0
*
Bivsr 0 nvsr i={Cs}*v(nws)*v(nvsi) + i(Vi2r)
Csr nvsr 0 {Cs} ic=0
Rvsr nvsr 0 1Meg
*
*****
*
* Imaginary part circuit
*
* <Vs-i>=-2/pi*Vs
Bii nii1 0 v=-2/pi*V(ns)
+ - {L1}*v(nws)*i(Vir)
+ - v(nvi)
Rii nii1 nii2 {Rp}
Vii nii2 nii dc 0
Lii nii nlmi {L1} ic=0
*
Bivi 0 nvi i=-{Cp}*v(nws)*v(nvr) + i(Vii)
Cpi nvi 0 {Cp} ic=0
Rvi nvi 0 1Meg
*
Bvlmi nlmi nlmi2 v={Lm}*v(nws)*i(Vimr)

```

```

Vimi nlmi2 nlmi3 dc 0
Rmi nlmi3 nlmi4 {Rm}
Lmi nlmi4 0 {Lm} ic=0
*
Bvl2i nlmi nl2i1 v={L2}*v(nws)*i(Vi2r) + 4/pi*v(no)*i(Vi2i)*V(n_ino)
+ v(nvsi)
Vi2i nl2i1 nl2i2 dc 0
Rsi nl2i2 nl2i3 {Rs}
L2i nl2i3 0 {L2} ic=0
*
Bivsi 0 nvsi i=-{Cs}*v(nws)*v(nvsr) + i(Vi2i)
Csi nvsi 0 {Cs} ic=0
Rvsi nvsi 0 1Meg
*
*****
*
* Output Section
*
* Bino = Total output current
Bino nino 0 v=2*sqrt(i(Vi2r)*i(Vi2r)+i(Vi2i)*i(Vi2i))
Rino nino 0 1Meg
*
Bl_ino n_ino 0 v=1/(V(nino)+1e-2)
Rl_ino n_ino 0 1Meg
*
*****
*
Bio 0 no i=2/pi*V(nino)
Rio2 no 0 1Meg
*Vac no no2 0 ac 1
Vac no no2 0 dc 0
Ro no2 0 {RL}
R_esr no2 nesr {Resr}
Cout nesr 0 {Co} ic=0
*
*****
*
.option itl4=100 chgtol=1.0e-28
.option method=gear
*
.ac dec 100 1 100k
*
.end
.control
shell time /t
*destroy all
set units=degrees
run

```

```
shell time /t
*
* Command sequences:
* 1. source k-10mm_bode.o.cir
* 2. plot vdb(no) vp(no)
*
.endc
```

## Appendix 4 SPICE Circuit File for Ip Response Generation (Gap = 20 mm)

```

TET Ip response bode plot(k-20mm_Ip)
*****
*
.param L1=22.30e-6
.param L2=21.99e-6
.param Lm=10.99e-6
*
.param Rp=12e-3
.param Rs=15e-3
.param Rm=12e-3
*
.param Cp=10.99e-9
.param Cs=11.09e-9
*
.param Co=330e-6
.param Resr=10e-3
*
*****
*
* RL may be 9.6, 20, 30, or 48
*
.param RL=9.6
*
*****
*
.param Vin=30
.param VFS=321e3
*
*****
*
* Input Section
*
Vfs nfs 0 dc {VFS}
Rfs nfs 0 1Meg
Bws nws 0 v=(2*pi*v(nfs))
Rws nws 0 10Meg
*
*Vs ns 0 dc {Vin} ac 1
Vs ns 0 dc {Vin}
Bis ns 0 i={4/pi}*sqrt(i(Vir)*i(Vir)+i(Vii)*i(Vii))

```

```

*
*****
*
* Real part circuit
*
* <Vs-r>=0
Bir nir1 0 v={L1}*v(nws)*i(Vii)
+ - v(nvr)
Rir nir1 nir2 {Rp}
Vir nir2 nir dc 0
Lir nir nlmr {L1} ic=0
*
Bivr 0 nvr i={Cp}*v(nws)*v(nvi) + i(Vir)
Cpr nvr 0 {Cp} ic=0
Rvr nvr 0 1Meg
*
Bvlmr nlmr nlmr2 v=-{Lm}*v(nws)*i(Vimi)
Vimr nlmr2 nlmr3 dc 0
Rmr nlmr3 nlmr4 {Rm}
Lmr nlmr4 0 {Lm} ic=0
*
Bvl2r nlmr nl2r1 v=-{L2}*v(nws)*i(Vi2i) + 4/pi*v(no)*i(Vi2r)*V(n_ino)
+ v(nvsr)
Vi2r nl2r1 nl2r2 dc 0
Rsr nl2r2 nl2r3 {Rs}
L2r nl2r3 0 {L2} ic=0
*
Bivsr 0 nvsr i={Cs}*v(nws)*v(nvsi) + i(Vi2r)
Csr nvsr 0 {Cs} ic=0
Rvsr nvsr 0 1Meg
*
*****
*
* Imaginary part circuit
*
* <Vs-i>=-2/pi*Vs
Bii nii1 0 v=-2/pi*V(ns)
+ - {L1}*v(nws)*i(Vir)
+ - v(nvi)
Rii nii1 nii2 {Rp}
Vii nii2 nii dc 0
Lii nii nlmi {L1} ic=0
*
Bivi 0 nvi i=-{Cp}*v(nws)*v(nvr) + i(Vii)
Cpi nvi 0 {Cp} ic=0
Rvi nvi 0 1Meg
*
Bvlmi nlmi nlmi2 v={Lm}*v(nws)*i(Vimr)

```

```

Vimi nlmi2 nlmi3 dc 0
Rmi nlmi3 nlmi4 {Rm}
Lmi nlmi4 0 {Lm} ic=0
*
Bvl2i nlmi nl2i1 v={L2}*v(nws)*i(Vi2r) + 4/pi*v(no)*i(Vi2i)*V(n_ino)
+ v(nvsi)
Vi2i nl2i1 nl2i2 dc 0
Rsi nl2i2 nl2i3 {Rs}
L2i nl2i3 0 {L2} ic=0
*
Bivsi 0 nvsi i=-{Cs}*v(nws)*v(nvsr) + i(Vi2i)
Csi nvsi 0 {Cs} ic=0
Rvsi nvsi 0 1Meg
*
*****
*
* Output Section
*
* Bino = Total output current
Bino nino 0 v=2*sqrt(i(Vi2r)*i(Vi2r)+i(Vi2i)*i(Vi2i))
Rino nino 0 1Meg
*
Bl_ino n_ino 0 v=1/(V(nino)+1e-2)
Rl_ino n_ino 0 1Meg
*
*****
*
Bio 0 no i=2/pi*V(nino)
Rio2 no 0 1Meg
Vac no no2 0 ac 1
*Vac no no2 0 dc 0
Ro no2 0 {RL}
R_esr no2 nesr {Resr}
Cout nesr 0 {Co} ic=0
*
*****
*
.option itl4=100 chgtol=1.0e-28
.option method=gear
*
.ac dec 100 1 100k
*
.end
.control
shell time /t
*destroy all
set units=degrees
run

```

```
shell time /t
*
* Command sequences:
* 1. source k-20mm_Ip.o.cir
* 2. plot db(i(Vs))
*
.endc
```

# Appendix 5 ADC & Comparator Resolution Requirements

In the hardware circuits, there are three analog signals being processed by the primary side DSP: the dc input voltage  $V_{IN}$ , the peak level of primary current  $I_{P,pk}$ , and the tone signals from TET secondary (after filtering). These signals will first be converted by the DSP's ADC (analog-to-digital) module into digital numbers and then be processed by the software program. For good system performance, there are minimum requirements in the ADC resolution for each of the analog signals.

Besides the three ADC sampled analog signals, the primary current waveform is converted into digital signals by the DSP's analog comparator, and the current level is set by an on-chip DAC (digital-to-analog converter). The resolution requirement for the DAC unit will be analyzed in this appendix.

Lastly, at the secondary side of the power regulator, the output voltage will be converted as tone signal in the 20 kHz – 30 kHz frequency band and then transmitted to the primary side. The ADC resolution requirement of the secondary side controller will also be analyzed.

## 1. DC input voltage $V_{IN}$

The dc input voltage  $V_{IN}$  is being combined with the duty ratio  $D$  to form a (feed-forward) coefficient for voltage loop control:

$$\delta = \frac{1}{2 \cdot V_{IN} \cdot \cos\left(\frac{D\pi}{2}\right)}$$

As long as the coefficient value is tracking the variation of  $V_{IN}$  and the duty ratio  $D$ , no fine ADC resolution for  $V_{IN}$  is required. The minimum ADC resolution will be 8-bit.

## 2. Peak level of primary current $I_{P,pk}$

The peak level of primary current  $I_{P,pk}$  is mainly used for output loading transient detection; and for the first phase of transient current PWM control. There is no need for fine ADC resolution in the transient detection phase because the criteria for load transient is quite

loose. There is a stricter requirement on the ADC resolution during transient current PWM control since  $\frac{\Delta I_{p,pk}}{\Delta t}$  is used as the control parameter for PWM update. The ADC resolution requirement for the (peak) primary current  $I_{p,pk}$  will be 9-bit.

### **3. Tone signals from TET secondary**

The tone signals from TET secondary need to be frequency decoded by Goertzel algorithm to determine the current output voltage level. Since Goertzel algorithm is actually a spectral energy calculation function, the accuracy of the waveforms is not important as long as the sine wave shape is there. The ADC resolution requirement will be 9-bit.

### **4. Primary current reference level (for analog comparator)**

For the analog comparator, it set the reference current level for conversion of sinusoidal shape primary current  $I_p$  into digital waveform. The digital waveform will be compared with the starting PWM signal for PLL frequency tracking. In the power regulator, the amplitude of  $I_p$  is less than 5 A under all loading conditions. So the full range of  $I_p$  is 10 A (from -5 A to +5 A). According to the graphs of primary current cutting level in Figure 2-8, the curve with slowest changing slope is the one for 48 ohm output loading. Within the normalize frequency range from 1.00 to 1.05, the curve has at least 1/4 A of current level variation. In order to achieve a 1% frequency resolution (i.e.  $\pm 0.01 f_s/f_i$  normalized frequency), the resolution of current cut level is 1/20 A and a total of 200 comparator steps is needed. The DAC resolution for analog comparator will be 8-bit.

### **5. Secondary side output voltage $V_O$**

The last analog signal under consideration is the secondary side output voltage  $V_O$ . The designed output voltage level is 24 V. This voltage information is converted into 5 voltage bands and the narrowest voltage band is 24 V  $\pm$  0.15 V. Taking half of the voltage band margin as the ADC resolution requirement, and setting the maximum  $V_O$  voltage as 35V, then  $35 / (0.15/2) = 467$  ADC steps are required. So the ADC resolution requirement for the output voltage  $V_O$  is 9-bit.

In our hardware system, the ADC and DAC modules for the primary and secondary side controllers all have 10-bit resolution, and they all fulfill the basic requirements for each of the analog signals under control.

## References

- [1] K. Van Schuylenbergh and R. Puers, *Inductive Powering: Basic Theory and Application to Biomedical Systems*. Springer Science + Business Media B.V., 2009.
- [2] B. Lenaerts and R. Puers, *Omnidirectional Inductive Powering for Biomedical Implants*. Springer Science + Business Media B. V., 2009.
- [3] H.H. Skilling, *Fundamentals of Electric Waves*. Wiley, New York/London, 1948.
- [4] R. Pethig, "Dielectric properties of biological materials: biophysical and medical applications," *IEEE Trans. Electrical Insulation*, vol. 19, no. 5, pp. 453-474, Oct. 1984.
- [5] A.M. Sodagar and P. Amin, "Capacitive coupling for power and data telemetry to implantable biomedical microsystems," in *Proceedings of the 4th International IEEE EMBS Conference on Neural Engineering*, pp. 411-414, May 2009.
- [6] J.C. Schuder, H.E. Stephenson, and J.F. Townsend, "High-level electromagnetic energy transfer through a closed chest wall," *IRE Internat. Conv. Rec.*, pt. 9, pp. 119-124, 1961.
- [7] J.C. Schuder and H.E. Stephenson, "Energy transport to a coil which circumscribes a ferrite core and is implanted within the body," *IEEE Trans. Biomedical Engineering*, vol. BME-12, no. 3, pp. 154-163, July 1965.
- [8] J.C. Schuder, G.K. Raines, H.E. Stephenson, and J.W. Mackenzie, "Low-frequency piezoelectric energy conversion for an intrathoracic artificial heart," *IEEE Trans. Biomedical Engineering*, vol. BME-15, no. 1, pp. 24-33, January 1968.
- [9] J.C. Schuder, J.H. Owens, H.E. Stephenson, and J.W. Mackenzie, "Response of dogs and mice to long-term exposure to the electromagnetic field required to power an artificial heart," *Trans. Amer. Soc. Artif. Int. Organs*, vol. 14, pp. 291-295, 1968.
- [10] J.C. Schuder, J.H. Gold, and H.E. Stephenson, "An inductively coupled RF system for the transmission of 1 kW of power through the skin," *IEEE Trans. Biomedical Engineering*, vol. BME-18, no. 4, pp. 265-273, July 1971.
- [11] J.C. Schuder, "Powering an artificial heart: Birth of the inductively coupled-radio frequency system in 1960," *Artificial Organs*, vol. 26, no. 11, pp. 909-915, Nov. 2002.
- [12] J.W. Fuller, "Apparatus for efficient power transfer through a tissue barrier," *IEEE Trans. Biomedical Engineering*, vol. BME-15, no. 1, pp. 63-65, Jan. 1968.
- [13] J.C. Norman, V.H. Covelli, W.F. Bernhard, and J. Spira, "An implantable nuclear fuel capsule for an artificial heart," *Trans. Amer. Soc. Artif. Int. Organs*, vol. 14, pp. 204-208, 1968.

- [14] G.H. Myers, G.E. Reed, A. Thumin, S. Fascher, and L. Cortes , “A transcutaneous power transformer,” *Trans. Amer. Soc. Artif. Int. Organs*, vol. 14, pp. 210-214, 1968.
- [15] R. Kadefors, E. Kaiser, and I. Petersen, “Energizing implantable transmitters by means of coupled inductance coils,” *IEEE Trans. Biomedical Engineering*, vol. BME-16, no. 3, pp. 177-183, July 1969.
- [16] F.W. Fraim and F.N. Huffman, “Performance of a tuned ferrite core transcutaneous transformer,” *IEEE Trans. Biomedical Engineering*, vol. BME-18, no. 5, pp. 177-183, Sept. 1971.
- [17] W.H. Ko and J. Hyneczek, “Implant evaluation of a nuclear power source,” *IEEE Trans. Biomedical Engineering*, vol. BME-21, no. 5, pp. 238-241, May 1974.
- [18] W.J. Kolff and J. Lawson, “Status of the artificial heart and cardiac assist devices in the United States,” *Trans. Amer. Soc. Artif. Int. Organs*, vol. 21, pp. 620-638, 1975.
- [19] E.S. Hochmair, “System optimization for improved accuracy in transcutaneous signal and power transmission,” *IEEE Trans. Biomedical Engineering*, vol. BME-31, no. 2, pp. 177-186, Feb. 1984.
- [20] C. Sherman, B.D.T. Daly, W. Clay, and K. Dasse, “In vivo evaluations of a transcutaneous energy transmission (TET) system,” *Trans. Amer. Soc. Artif. Int. Organs*, vol. 30, pp. 143-147, 1984.
- [21] D.C. Galbraith, M. Soma, and R.L. White, “A wide-band efficient inductive transdermal power and data link with coupling insensitive gain,” *IEEE Trans. Biomedical Engineering*, vol. BME-34, no. 4, pp. 265-275, Apr. 1987.
- [22] M. Soma, D.C. Galbraith, and R.L. White, “Radio-frequency coils in implantable devices: Misalignments analysis and design procedure,” *IEEE Trans. Biomedical Engineering*, vol. BME-34, no. 4, pp. 276-282, Apr. 1987.
- [23] W.J. Weiss, G. Rosenberg, A.J. Snyder, W.E. Pae, W.E. Richenbacher, and W.S. Pierce, “In vivo performance of a transcutaneous energy transmission system with the Penn State motor driven ventricular assist device,” *ASAIO Journal*, vol. 35, pp. 284-288, 1989.
- [24] T.H. Nishimura and L. Ding, “Implantable artificial heart system and new actuator control by power electronic system,” in *Proc. of IEEE international Conference on Systems Engineering, 1989*, pp. 289-292, 1989.
- [25] H. Matsuki, K. Nadehara, T. Watanabe, K. Murakami, and T. Yamamoto, “High-output transmitting coil with cloth structure utilizing amorphous magnetic fiber for implanted artificial heart,” *IEEE Trans. Magnetics*, vol. 25, no. 9, pp. 3812-3814, Sept. 1989.
- [26] W.J. Weiss, G. Rosenberg, A.J. Snyder, T.J. Cleary, R.P. Gaumont, D.B. Geselowitz, and W.S. Pierce, “Permanent circulatory support systems at the Pennsylvania State

- University,” *IEEE Trans. Biomedical Engineering*, vol. 37, no. 2, pp. 138-145, Feb. 1990.
- [27] Y. Mitamura, E. Okamoto, A. Hirano, and T. Mikami, “Development of an implantable motor-driven assist pump system,” *IEEE Trans. Biomedical Engineering*, vol. 37, no. 2, pp. 146-156, Feb. 1990.
- [28] N.O. Sokal and A.D. Sokal, “Class E – A new class of high-efficiency tuned single-ended switching power amplifiers,” *IEEE J. Solid-State Circuits*, vol. SC-10, no. 3, pp. 168-176, June 1975.
- [29] F.H. Raab, “Idealized operation of the class E tuned power amplifier,” *IEEE Trans. Circuits and Systems*, vol. CAS-24, no. 12, pp. 725-735, Dec. 1977.
- [30] M.K. Kazimierczuk and K. Puczek, “Exact analysis of class E tuned power amplifier at any Q and switch duty cycle,” *IEEE Trans. Circuits and Systems*, vol. CAS-34, no. 2, pp. 149-159, Feb. 1987.
- [31] C.M. Zierhofer and E.S. Hochmair, “High-efficiency coupling-insensitive transcutaneous power and data transmission via an inductive link,” *IEEE Trans. Biomedical Engineering*, vol. 37, no. 7, pp. 716-722, July 1990.
- [32] D. Jaron, “Current status of the artificial heart and cardiovascular assist devices,” in *Proc. of the 3rd Annual IEEE Symposium on Computer-Based Medical Systems, 1990*, pp. 3-6, 1990.
- [33] K. Smith, G. Bearnson, H. Kim, R. Layton, R. Jarmin, J.R. Fratto, and J. Smith, “Electronics for the electronhydraulic total artificial heart,” in *Proc. of the 3rd Annual IEEE Symposium on Computer-Based Medical Systems, 1990*, pp. 517-524, June 1990.
- [34] A. Ghahary and B.H. Cho, “Design of a transcutaneous energy transmission system using a series resonant converter,” in *Proceedings of 21st Annual IEEE Power Electronics Specialists Conf. 1990, PESC’90*, pp. 1-8, 1990.
- [35] R.A. Nazarian, A.J. Snyder, and S. Ford, “Development of a totally implantable artificial heart concept to implementation,” *IEEE Case Studies in Medical Instrument Design*, pp. 95-110, 1991.
- [36] P.D. Diegel, T. Mussivand, J.W. Holfert, J.T. Juretech, J.A. Miller, G.K. Maclean, Z. Szurmak, J.P. Santerre, K. Rajagopalan, D.B. Olsen, and W. Keon, “Electrohydraulic ventricular assist device development,” *ASAIO Journal*, vol. 39, pp. M306-M310, 1992.
- [37] P.R. Troyk and M.A.K. Schwan, “Closed-loop class E transcutaneous power and data link for microimplants,” *IEEE Trans. Biomedical Engineering*, vol. 39, no. 6, pp. 589-599, June 1992.

- [38] H. Matsuki, M. Shliki, K. Murakami, and T. Yamamoto, "Investigation of coil geometry for transcutaneous energy transmission for artificial heart," *IEEE Trans. Magnetics*, vol. 29, no. 5, pp. 2406-2408, Sept. 1992.
- [39] G.B. Bearnson, S.R. Krivoy, R.D. Jarmin, J.R. Fratto, P. Khanwilkar, K.R. Crump, and K.D. Smith, "Electronics development for the Utah electronhydraulic total artificial heart," in *Proc. of the 6th Annual IEEE Symposium on Computer-Based Medical Systems, 1993*, pp. 247-252, 1993.
- [40] J.M. Ahn, D.W. Kang, H.C. Kam, and B.G. Min, "In vivo performance evaluation of a transcutaneous energy and information transmission system for the total artificial heart," *ASAIO Journal*, vol. 39, pp. M208-M212, 1993.
- [41] J.A. Miller G. Gelanger, and T. Mussivand, "Development of an autotuned transcutaneous energy transfer system," *ASAIO Journal*, vol. 39, pp. M706-M710, 1993.
- [42] H. Sakamoto and K. Harada, "A novel converter for non-contact charging with electromagnetic coupling," *IEEE Trans. Magnetics*, vol. 29, no. 6, pp. 3228-3230, June 1993.
- [43] Y. Taenaka, T. Masuzawa, E. Tatsumi, H. Anai, K. Toda, H. Akagi, T. Nakatani, Y. Baba, K. Eya, Y. Wakisaka, H. Takano, K. Koshiji, E. Shu, T. Utsunomiya, and Y. Fukui, "Development and evaluation of components for a totally implantable artificial heart system," *ASAIO Journal*, vol. 40, pp. M314-M318, 1994.
- [44] T. Mussivand, A. Hum, M. Diguier, K.S. Holmes, G. Vecchio, R.G. Masters, P.J. Hendry, and W.J. Keon, "A transcutaneous energy and information transfer system for implanted medical devices," *ASAIO Journal*, vol. 41, pp. M253-M258, 1995.
- [45] R.P. Phillips, "A high capacity transcutaneous energy transmission system," *ASAIO Journal*, vol. 41, pp. M259-M262, 1995.
- [46] T. Masuzawa, Y. Taenaka, E. Tatsumi, J.M. Ahn, T. Ohno, K. Toda, K. Miyazaki, Y. Wakisaka, K. Eya, Y. Baba, T. Nakatani, H. Takano, C. Uyama, K. Koshiji, Y. Fukui, K. Takahashi, K. Tsuchimoto, and K. Tsukahara, "Set-up, improvement, and evaluation of an electrohydraulic total artificial heart with a separately placed energy converter," *ASAIO Journal*, vol. 42, pp. M328-M332, 1996.
- [47] W.J. Weiss, G. Rosenberg, A.J. Snyder, M. Rawhouser, W.S. Pierce, H. Kusagawa, S. Mehta, G.A. Prophet, J.A. Marlotte, R.A. Nazarian, S.K. Ford, and D.L. Hicks, "Recent improvements in a completely implanted total artificial heart," *ASAIO Journal*, vol. 42, pp. M342-M346, 1996.
- [48] H. Matsuki, Y. Yamakata, N. Chubachi, S.I. Nitta, and H. Hashimoto, "Transcutaneous DC-DC converter for totally implantable artificial heart using

- synchronous rectifier,” *IEEE Trans. Magnetics*, vol. 32, no. 9, pp. 5118-5120, Sept. 1996.
- [49] H. Matsuki, Y. Yamakata, N. Jinguji, S. Nitta, N. Hoshimiya, and N. Chubachi, “Energy transferring system reducing temperature rise for implantable power consuming devices,” in *Proc. of the 18th Annual International Conf. of IEEE EMBS*, pp. 185-186, 1996.
- [50] D.B. Melvin, D.L. Glos, D. Nebrigic, A.J. Helmicki, R.L. Brown, P.N. Purcell, and H.T. Henderson, “In vivo comparison of two enteric-pouch power transformers for circulatory support,” *Artificial Organs*, vol. 21, no. 8, pp. 935-946, Aug. 1997.
- [51] K. Shiba, E. Shu, K. Koshiji, K. Tsukahara, K. Tsuchimoto, T. Ohu-mi, T. Nakamura, S. Endo, T. Masuzawa, E. Tatsumi, Y. Taenaka, and H. Takano, “Efficiency improvement and in vivo estimation of externally-coupled transcutaneous energy transmission system for a totally implantable artificial heart,” in *Proc. of the 19th Annual International Conf. of IEEE EMBS*, pp. 2503-2505, Nov. 1997.
- [52] T. Masuzawa, E. Tatsumi, Y. Taenaka, M. Nakamura, S. Endo, H. Takano, K. Koshiji, Y. Fukui, T. Murai, and K. Tsukahara, “Progress of an electrohydraulic total artificial heart system with a separate energy converter,” *ASAIO Journal*, vol. 45, pp. 471-477, 1999.
- [53] R.D. Dowling, S.W. Etoch, K. Stevens, A. Butterfield, S.E. Koenig, A. Johnson, B. Chiang, and L.A. Gray, “Initial experience with the AbioCor implantable replacement heart at the University of Louisville,” *ASAIO Journal*, vol. 46, pp. 579-581, 2000.
- [54] R. Puers and G. Vandervoorde, “Recent progress on transcutaneous energy transfer for total artificial heart systems,” *Artificial Organs*, vol. 25, no. 5, pp. 400-405, May 2001.
- [55] T. Ozeki, T. Chinzei, Y. Abe, I. Saito, T. Isoyama, S. Mochizuki, M. Ishimaru, K. Takiura, A. Baba, T. Toyama, and K. Imachi, “Function for detecting malposition of transcutaneous energy transmission coils,” *ASAIO Journal*, vol. 49, pp. 469-474, 2003.
- [56] T.C. Rintoul and A. Dolgin, “Thoratec transcutaneous energy transformer system: A review and update,” *ASAIO Journal*, vol. 50, pp. 397-400, 2004.
- [57] S. Weber, K. Kamohara, R.S. Klatte, V. Luangphakdy, C. Flick, J.F. Chen, F. Casas, Y. Ootaki, M. Kopcak, M. Akyama, G.B. Hirschman, P.A. Chapman, A. Donahue, W. Wetterau, C. Prisco, R. Mast, C. Sherman, K. Fukamachi, and W.A. Smith, “MagScrew TAH: An update,” *ASAIO Journal*, vol. 51, pp. xxxvi-xivi, 2005.
- [58] H. Miura, S. Arai, Y. Kakubari, F. Sato, H. Matsuki, and T. Sato, “A synchronous rectification using a digital PLL technique for contactless power supplies,” *IEEE Trans. Magnetics*, vol. 42, no. 10, pp. 3997-3999, Oct. 2005.

- [59] S. Arai, H. Miura, F. Sato, H. Matsuki, and T. Sato, "Examination of circuit parameters for stable high efficiency TETS for artificial hearts," *IEEE Trans. Magnetics*, vol. 42, no. 10, pp. 4170-4172, Oct. 2005.
- [60] H. Miura, S. Arai, Y. Kakubari, F. Sato, H. Matsuki, and T. Sato, "Improvement of the transcutaneous energy transmission system utilizing ferrite cored coils for artificial hearts," *IEEE Trans. Magnetics*, vol. 42, no. 10, pp. 3578-3580, Oct. 2006.
- [61] E. Okamoto, Y. Yamamoto, Y. Akasaka, T. Motomura, Y. Mitamura, and Y. Nose, "A new transcutaneous energy transmission system with hybrid energy coils for driving an implantable biventricular assist device," *Artificial Organs*, vol. 33, no. 8, pp. 622-626, Aug. 2009.
- [62] R. Kadefors, "Controlled external powering of miniaturized chronically implanted biotelemetry devices," *IEEE Trans. Biomedical Engineering*, vol. BME-23, no. 2, pp. 124-129, Feb. 1976.
- [63] A. Ghahary and B.H. Cho, "Design of transcutaneous energy transmission system using a series resonant converter," *IEEE Trans. Power Electronics*, vol. 7, no. 2, pp. 261-269, Apr. 1992.
- [64] C.G. Kim, and B.H. Cho, "Transcutaneous energy transmission with double tuned duty cycle control," in *Proceedings of the 31st Intersociety Energy Conversion Engineering Conference, IECEC 96*, pp. 587-591, Aug. 1996.
- [65] G.B. Joungh and B.H. Cho, "An energy transmission system for an artificial heart using leakage inductance compensation of transcutaneous transformer," *IEEE Trans. Power Electronics*, vol. 13, no. 6, pp. 1013-1022, Nov. 1998.
- [66] C.S. Wang, G.A. Covic, and O.H. Stielau, "Power transfer capability and bifurcation phenomena of loosely coupled inductive power transfer system," *IEEE Trans. Industrial Electronics*, vol. 51, no. 1, pp. 148-157, Feb. 2004.
- [67] W. Zhou and H. Ma, "Design considerations of compensation topologies in ICPT system," in *Proceedings of 22nd Annual IEEE Applied Power Electronics Conf. 2007, APEC 2007*, pp. 985-990, 2007.
- [68] P. Si, A.P. Hu, S. Malpas, and D. Budgett, "A frequency control method for regulating wireless power to implantable devices," *IEEE Trans. Biomedical Circuits and Systems*, vol. 3, no. 1, pp. 22-29, Mar. 2008.
- [69] H.L. Li, A.P. Hu, and G.A. Convic, "FPGA controlled high frequency resonant converter for contactless power supply," in *Proceedings of IEEE Power Electronics Specialists Conf. 2008, PESC 2008*, pp. 245-250, 2008.
- [70] T.D. Dissanayake, A.P. Hu, S. Malpas, L. Bennet, A. Taberner, L. Booth, and D. Budgett, "Experimental study of a TET system for implantable biomedical devices," *IEEE Trans. Biomedical Circuits and Systems*, vol. 3, no. 6, pp. 370-378, Dec. 2009.

- [71] T.D. Dissanayake, D.M. Budegtt, P. Hu, L. Bennet, S. Pyner, L. Booth, S. Amirapu, Y. Wu, and S.C. Malpas, "A novel low temperature transcutaneous energy transfer system for high power implantable medical devices: Performance and validation in sheep," *Artificial Organs*, vol. 34, no. 5, pp. E160-E167, May 2010.
- [72] Q. Chen, S.C. Wong, C.K. Tse, and X. Ruan, "Analysis, design and control of a transcutaneous power regulator for artificial heart," *IEEE Trans. Biomedical Circuits and Systems*, vol. 3, no. 1, pp. 23-31, Feb. 2009.
- [73] A.J. Moradewicz and P. Kazmierkowski, "FPGA based control of series resonant converter for contactless power supply," in *Proceedings of IEEE International Symposium on Industrial Electronics 2008, ISIE 2008*, pp. 245-250, 2008.
- [74] J. Sallan, J.L. Villa, A. Llombart, and J.F. Sanz, "Optimal design of ICPT system applied to electric vehicle battery charge," *IEEE Trans. Industrial Electronics*, vol. 56, no. 6, pp. 2140-2149, June 2009.
- [75] W. Fang, W. Liu, J. Qian, H. Tang, and P. Ye, "Modeling and simulation of a transcutaneous energy transmission system used in artificial organ implants," *Artificial Organs*, vol. 33, no. 12, pp. 1069-1074, Dec. 2009.
- [76] A.J. Moradewicz and P. Kazmierkowski, "Contactless energy transfer system with FPGA-controlled resonant converter," *IEEE Trans. Industrial Electronics*, vol. 57, no. 9, pp. 3181-3190, Sept. 2010.
- [77] D.J. Thrimawithana and U.K. Madawala, "A primary side controller for inductive power transfer systems," in *Proceedings of IEEE International Conf. on Industrial Technology, ICIT 2010*, pp. 661-666, 2010.
- [78] J. Hirai, T.W. Kim, and A. Kawamura, "Study on intelligent battery charging using inductive transmission of power and information," *IEEE Trans. Power Electronics*, vol. 15, no. 2, pp. 335-345, Mar. 2000.
- [79] A. Prodic, D. Maksimovic, and R.W. Erickson, "Digital controller chip set for isolated DC power supplies," in *Proc. of the 18th Annual IEEE Applied Power Electronics Conf. and Exposition, 2003, APEC'03*, pp. 866-872, 2003.
- [80] T. Mussivand, A. Hum, K.S. Holmes, and W.J. Keon, "Wireless monitoring and control for implantable rotary blood pumps," *Artificial Organs*, vol. 21, no. 7, pp. 661-664, July 1997.
- [81] K. Inoue, K. Shiba, E. Shu, K. Koshiji, K. Tsukahara, T. Oh-umi, T. Masuzawa, E. Tatsumi, Y. Taenaka, and H. Takano, "Transcutaneous optical telemetry system – investigation on deviation characteristics," in *Proc. of the 19th Annual International Conf. of IEEE EMBS*, pp. 2235-2237, Nov. 1997.

- [82] K. Inoue, K. Shiba, E. Shu, K. Koshiji, K. Tsukahara, T. Oh-umi, T. Masuzawa, E. Tatsumi, Y. Taenaka, and H. Takano, "Transcutaneous optical telemetry system with infrared laser diode," *ASAIO Journal*, vol. 44, pp. 841-844, 1998.
- [83] A. Homma, Y. Taenaka, E. Tatsumi, Y. Takewa, T. Kamimura, H. Naitoh, M. Oshikawa, T. Mizuno, K. Shioya, H.S. Lee, T. Tsukiya, Y. Kakuta, N. Katahira, H. Takano, S. Kitamura, K. Koshiji, K. Shiba, Y. Fukui, H. Wakui, K. Tsuchimoto, H. Fukuda, and K. Tsukahara, "Current status of national cardiovascular center totally implantable artificial heart system," in *SICE Annual Conference in Sapporo*, pp. 436-441, Aug. 2004.
- [84] K.S. Guillory, A.K. Misener, and A. Pungor, "Hybrid RF/IR transcutaneous telemetry for power and high-bandwidth data," in *Proc. of the 26th Annual International Conf. of IEEE EMBS*, pp. 4338-4340, Sept. 2004.
- [85] D.M. Ackermann, B. Smith, K.L. Kilgore, and P.H. Peckham, "Design of a high speed transcutaneous optical telemetry link," in *Proc. of the 28th Annual International Conf. of IEEE EMBS*, pp. 2932-2935, Aug. 2006.
- [86] D.M. Ackermann, B. Smith, X.F. Wang, K.L. Kilgore, and P.H. Peckham, "Design the optical interface of a transcutaneous optical telemetry link," *IEEE Trans. Biomedical Engineering*, vol. 55, no. 4, pp. 1365-1373, Apr. 2008.
- [87] S. Parmentier, R. Fontaine, and Y. Roy, "Laser diode used in 16 Mb/s, 10 mW optical transcutaneous telemetry system," in *Proc. of Biomedical Circuits and Systems Conf. 2008, BioCAS 2008*, pp. 377-380, 2008.
- [88] H. Matsuki, k. Ofuji, N. Chubachi, and S. Nitta, "Signal transmission for implantable medical devices using figure-of-eight coils," *IEEE Trans. Magnetics*, vol. 32, no. 5, pp. 5121-5123, Sept. 1996.
- [89] M. Takahashi, K. Watanabe, F. Sato, and H. Matsuki, "Signal transmission system for high frequency magnetic telemetry for an artificial heart," *IEEE Trans. Magnetics*, vol. 37, no. 4, pp. 2921-2924, July 2001.
- [90] T. Takura, H. Ishiai, F. Sato, H. Matsuki, and T. Sato, "Basic evaluation of signal transmission coil in transcutaneous magnetic telemetry system for artificial hearts," *IEEE Trans. Magnetics*, vol. 41, no. 10, pp. 4173-4175, Oct. 2005.
- [91] Y. Hu and M. Sawan, "A fully integrated low-power BPSK demodulator for implantable medical devices," *IEEE Trans. Circuits and Systems I: Regular Papers*, vol. 52, no. 12, pp. 2552-2562, Dec. 2005.
- [92] W.H. Ko, J. Hyneczek, and J. Homa, "Single frequency RF powered ECG telemetry system," *IEEE Trans. Biomedical Engineering*, vol. BME-26, no. 2, pp. 105-109, Feb. 1979.

- [93] K.W. Fernald, J.J. Paulos, B.A. Stackhouse, and R.A. Heaton, "A self-tuning digital telemetry IC for use in a microprocessor-based implantable instrument," *IEEE Journal of Solid-State Circuits*, vol. 27, no. 12, pp. 5121-5123, Dec. 1992.
- [94] H.J. Song, D.R. Allee, and K.T. Speed, "Single chip system for bio-data acquisition, digitization and telemetry," in *Proceedings of the 1997 IEEE International Symposium on Circuits and Systems*, vol. 3, pp. 1848-1851, June 1997.
- [95] M. Ghovanloo and K. Najafi, "A wideband frequency-shift keying wireless link for inductively powered biomedical implants," *IEEE Trans. Circuits and Systems I: Regular Papers*, vol. 51, no. 12, pp. 2374-2383, Dec. 2004.
- [96] R.N. Simons, F.A. Miranda, J.D. Wilson, and R.E. Simons, "Wearable wireless telemetry system for implantable bio-MEMS sensors," in *Proc. of the 28th Annual International Conf. of IEEE EMBS*, pp. 6245-6248, Aug. 2006.
- [97] J. Choi, J.W. Park, J. Chung, and B.G. Min, "An intelligent remote monitoring system for artificial heart," *IEEE Trans. Information Technology in Biomedicine*, vol. 9, no. 4, pp. 564-573, Dec. 2005.
- [98] P.D. Bradley, "An ultra low power, high performance Medical Implant Communication System (MICS) transceiver for implantable devices," in *Proc. of Biomedical Circuits and Systems Conf. 2006, BioCAS 2006*, pp. 158-161, 2006.
- [99] P. Gandolfo, D. Radovic, M. Savic, and D. Simic, "IEEE 802.15.4a UWB-IR Radio System for Telemedicine," in *Proceedings of the 2008 IEEE International Conf. on Ultra-Wideband (ICUWB2008)*, vol. 3, pp. 11-14, Sept. 2008.
- [100] Z. Tang, B. Smith, J.H. Schild, and P.H. Peckham, "Data transmission from an implantable biotelemetry by load-shift keying using circuit configuration modulator," *IEEE Trans. Biomedical Engineering*, vol. 42, no. 5, pp. 524-528, May 1995.
- [101] G. Wang, W. Liu, M. Sivaprakasam, and G.A. Kendir, "Design and analysis of an adaptive transcutaneous power telemetry for biomedical implants," *IEEE Trans. Circuits and Systems I: Regular Papers*, vol. 52, no. 10, pp. 2109-2117, Oct. 2005.
- [102] M. Ghovanloo, and S. Atluri, "An integrated full-wave COMS rectifier with built-in back telemetry for RFID and implantable biomedical applications," *IEEE Trans. Circuits and Systems I: Regular Papers*, vol. 55, no. 10, pp. 3328-3334, Nov. 2008.
- [103] W. Xu, Z. Luo, and S. Sonkusale, "Fully digital BPSK demodulator and multilevel LSK back telemetry for biomedical implant transceivers," *IEEE Trans. Circuits and Systems II: Express Briefs*, vol. 56, no. 9, pp. 714-718, Sept. 2009.
- [104] T.G. Zimmerman, "Personal area network (PAN)," M.S. thesis, Media Lab., Massachusetts Inst. Technology, Cambridge, MA, 1995.
- [105] T. Handa, S. Shoji, S. Ike, S. Takeda, and T. Sekiguchi, "A very low-power consumption wireless ECG monitoring system using body as a signal transmission

- medium,” in *IEEE Proc. of International Conf. on Solid-State Sensors and Actuators, TRANSDUCERS '97*, vol. 2, pp. 1003-1006, June 1997.
- [106] K. Hachisuka, A. Nakata, T. Takeda, Y. Terauchi, K. Shiba, K. Sasaki, H. Hosaka, and K. Itao, “Development and performance of an intra-body communication device,” in *IEEE Proc. of the 12th International Conf. on Solid State Sensors, Actuator and Microsystems*, vol. 2, pp. 1722-1725, June 2003.
- [107] J.A. Ruiz and S. Shimamoto, “Experimental evaluation of body channel response and digital modulation schemes for intra-body communications,” in *Proceedings of the IEEE International Conf. on Communications*, vol. 1, pp. 349-354, 2006.
- [108] M.S. Wegmueller, A. Kuhn, J. Froehlich, M. Oberle, N. Felber, N. Kuster, and W. Fichtner, “An attempt to model the human body as a communication channel,” *IEEE Trans. Biomedical Engineering*, vol. 54, no. 10, pp. 1851-1857, Oct. 2007.
- [109] M.S. Wegmueller, S. Huclova, J. Froehlich, M. Oberle, N. Felber, N. Kuster, and W. Fichtner, “Galvanic coupling enabling wireless implant communications,” *IEEE Trans. Instrumentation and Measurement*, vol. 58, no. 8, pp. 2618-2625, Aug. 2009.
- [110] M.S. Wegmueller, M. Oberle, N. Felber, N. Kuster, and W. Fichtner, “Signal transmission by galvanic coupling through the human body,” *IEEE Trans. Instrumentation and Measurement*, vol. 59, no. 4, pp. 963-969, Apr. 2010.
- [111] E. Okamoto, Y. Sato, K. Seino, T. Kiyono, Y. Kato, and Y. Mitamura, “Basic study of a transcutaneous information transmission system using intra-body communication,” *Journal of Artificial Organs*, vol. 13, pp. 117-120, 2010.
- [112] G.K. Maclean, P.A. Aiken, W.A. Adams, and T. Mussivand, “Evaluation of nickel-cadmium battery packs for mechanical circulatory support devices,” *ASAIO Journal*, vol. 39, pp. M423-M426, 1993.
- [113] G.K. Maclean, P.A. Aiken, D.G. Duguay, W.A. Adams, and T. Mussivand, “The effect of pulsatile power loads on nickel/cadmium battery cells for mechanical circulatory support devices,” *ASAIO Journal*, vol. 40, pp. 67-69, 1994.
- [114] E. Okamoto, T. Yoshida, M. Fujiyoshi, M. Shimanaka, A. Takeuchi, Y. Mitamura, and T. Mikami, “Feasibility of a Nickel-Metal hydride battery for totally implantable artificial hearts,” *ASAIO Journal*, vol. 42, pp. M332-M337, 1996.
- [115] H. Honda, K. Shiba, E. Shu, K. Koshji, T. Murai, J. Yana, T. Masuzawa, E. Tatsumi, Y. Taenaka, and H. Takano, “Study on lithium-ion secondary battery for implantable artificial heart,” in *Proc. of the 19th Annual International Conf. of IEEE EMBS*, pp. 2315-2317, Nov. 1997.
- [116] H. Honda, K. Shiba, E. Shu, K. Koshji, T. Murai, T. Nakamura, T. Masuzawa, E. Tatsumi, Y. Taenaka, and H. Takano, “Selection of a rechargeable internal back-up

- battery for a totally implantable artificial heart,” *ASAIO Journal*, vol. 45, pp. 339 -343, 1999.
- [117] E. Okamoto, K. Watanabe, K. Hashiba, T. Inoue, E. Iwazawa, M. Momoi, T. Hashimoto, and Y. Mitamura, “Optimum selection of an implantable secondary battery for an artificial heart by examination of the cycle life test,” *ASAIO Journal*, vol. 48, pp. 495-502, 2002.
- [118] W.C. Lin, W.H. Ko, and O.P. Agrawal, “Fast charging circuit for NiCd battery used in implant electronic systems,” *IEEE Trans. Biomedical Engineering*, vol. BME-17, no. 4, pp. 331-334, Oct. 1970.
- [119] D.C. Jeutter, “A transcutaneous implanted battery recharging and biotelemeter power switching system,” *IEEE Trans. Biomedical Engineering*, vol. BME-29, no. 5, pp. 314-321, July 1982.
- [120] W.E. Kim, J.M. Ahn, S.W. Choi, and B.G. Min, “Intelligent Li ion battery management based on a digital signal processor for a moving actuator total artificial heart,” *ASAIO Journal*, vol. 43, pp. M588-M592, 1997.
- [121] K. Shiba, E. Shu, K. Koshji, K. Tsukahara, T. Nakamura, T. Masuzawa, E. Tatsumi, Y. Taenaka, and H. Takano, “A transcutaneous energy transmission system with rechargeable internal back-up battery for a totally implantable total artificial heart,” *ASAIO Journal*, vol. 45, pp. 466-470, 1999.
- [122] E. Okamoto, T. Inoue, K. Watanabe, T. Hashimoto, E. Iwazawa, Y. Abe, T. Chinzei, T. Isoyama, S. Kobayashi, I. Saito, F. Sato, H. Matsuki, , K. Imachi, and Y. Mitamura, “Development of an implantable high-energy and compact battery system for artificial heart,” *Artificial Organs*, vol. 27, no. 2, pp. 184-188, Feb. 2003.
- [123] P. Li, and R. Bashirullah, “A wireless power interface for rechargeable battery operated medical implants,” *IEEE Trans. Circuits and Systems II: Express Briefs*, vol. 54, no. 10, pp. 912-916, Oct. 2007.
- [124] C.R. Davies, F. Fukumura, K. Fukamachi, K. Muramoto, S.C. Himley, A. Massiello, J.F. Chen, and H. Harasaki, “Adaptation of tissue to a chronic heat load,” *ASAIO Journal*, vol. 40, pp. M514-M517, 1994.
- [125] Y. Okazaki, C.R. Davies, T. Matsuyoshi, K. Fukamachi, K.E. Wika, and H. Harasaki, “Heat from an implanted power source is mainly dissipated by blood perfusion,” *ASAIO Journal*, vol. 43, pp. M585-M588, 1997.
- [126] E. Okamoto, T. Makino, M. Nakamura, S. Tanaka, T. Chinzei, Y. Abe, T. Isoyama, I. Saito, S.I. Mochizuki, K. Imachi, Y. Inoue, and Y. Mitamura, “Numerical estimation of heat distribution from the implantable battery system of an undulation pump LVAD,” *Journal of Artificial Organs*, vol. 9, pp. 77-83, 2006.

- [127] E. Okamoto, M. Nakamura, Y. Akasaka, Y. Inoue, Y. Abe, T. Chinzei, I. Saito, T. Isoyama, S. Mochizuki, K. Imachi, and Y. Mitamura, "Analysis of heat generation of lithium ion rechargeable batteries used in implantable battery systems for driving undulation pump ventricular assist device," *Artificial Organs*, vol. 31, no. 7, pp. 538-541, July 2007.
- [128] International Commission on Non-Ionizing Radiation Protection, "Guidelines for Limiting Exposure to Time-Varying Electric, Magnetic, and Electromagnetic Fields (up to 300 GHz)", *Health Physics*, vol. 74, no. 4, pp. 494-522, 1998. Available: <http://www.icnirp.de/PubEMF.htm>
- [129] Guidelines (Wed article). Available: [http://www.rfsafetysolutions.com/RF%20Radiation%20Pages/ICNIRP\\_Guidelines.html](http://www.rfsafetysolutions.com/RF%20Radiation%20Pages/ICNIRP_Guidelines.html)
- [130] T. Yamamoto, K. Koshiji, A. Homma, E. Tatsumi, and Y. Taenaka, "Improvement in magnetic field immunity of externally-coupled transcutaneous energy transmission system for a totally implantable artificial heart," *Journal of Artificial Organs*, vol. 11, pp. 238-240, 2008.
- [131] K. Shiba, M. Nukaya, T. Tsuji, and K. Koshiji, "Analysis of current density and specific absorption rate in biological tissue surrounding transcutaneous transformer for an artificial heart," *IEEE Trans. Biomedical Engineering*, vol. 55, no. 1, pp. 205-213, Jan. 2008.
- [132] N. Higaki and K. Shiba, "Analysis of specific absorption rate and current density in biological tissues surrounding energy transmission transformer for an artificial heart: using magnetic resonance imaging-based human body model," *Artificial Organs*, vol. 34, no. 1, pp. E1-E9, Jan. 2010.
- [133] R.L. Steigerwald, "A comparison of half-bridge resonant converter topologies," *IEEE Trans. Power Electronics*, vol. 3, no. 2, pp. 174-182, Apr. 1988.
- [134] S.C. Wong and A.D. Brown, "Macromodelling series-resonant convertor circuits," *IEE Proc. – Circuits, Devices and Systems*, vol. 142, no. 1, pp. 83-89, Feb. 1995.
- [135] S.C. Wong, "A Macromodel for resonant converter circuits," Ph. D. dissertation, University of Southampton, May 1997.
- [136] Y. Zhang and P.C. Sen, "D-Q model for resonant converters," in *Proceedings of the 35th Annual Power Electronics Specialists Conference, PESC 04*, pp. 1749-1753, June 2004.
- [137] Z. Ye, P.K. Jain, and P.C. Sen, "Phasor-domain modelling of resonant inverters for high-frequency AC power distribution systems," *IEEE Trans. Power Electronics*, vol. 24, no. 4, pp. 911-924, Apr. 2009.

- [138] Microchip Technology Inc., “dsPIC33FJ06GS101/X02 and dsPIC33FJ16GSX02/X04 Data Sheet, High-Performance, 16-bit Digital Signal Controllers,” 2009.
- [139] Microchip Technology Inc., “PIC12F609/615/12HV609/615 Data Sheet, 8-Pin Flash-Based, 8-bit CMOS Microcontrollers,” 2008.
- [140] F.W. Grover, *Inductance Calculations*. New York:Dover, 1964.
- [141] S.I. Babic and C. Akyel, “Calculating mutual inductance between circular coils with inclined axes in air,” *IEEE Trans. Magnetics*, vol. 44, no. 7, pp. 1743-1750, July 2008.
- [142] C.M. Zierhofer and E.S. Hochmair, “Geometric approach for coupling enhancement of magnetically coupled coils,” *IEEE Trans. Biomedical Engineering*, vol. 43, no. 7, pp. 708-714, July 1996.
- [143] C. Fernandez, O. Garcia, R. Prieto, J.A. Cobos, S. Gabriels, and G. Van Der Borcht, “Design issues of a core-less transformer for a contact-less application,” in *Proc. of the 17th Annual IEEE Applied Power Electronics Conference and Exposition, APEC 2002*, pp. 339-345, Sept. 2002.
- [144] P.K. Hanumolu, M. Brownlee, K. Mayaram, and U.K. Moon, “Analysis of charge-pump phase-locked loops,” *IEEE Trans. Circuit and Systems I: Regular Papers*, vol. 51, no. 9, pp. 1665-1674, Sept. 2004.
- [145] V. Kratyuk, P.K. Hanumolu, U.K. Moon, and K. Mayaram, “A design procedure for all-digital phase-locked loops based on a charge-pump phase-locked-loop analogy,” *IEEE Trans. Circuit and Systems II: Express Briefs*, vol. 54, no. 3, pp. 247-251, Mar. 2007.
- [146] G. Schmer, “DTMF tone generation and detection: an implementation using the TMS320C54x,” *Texas instruments, Application Report SPRA096A*, May 2000.
- [147] G.F. Frankin, J.D. Powell, and M.L. Workman, *Digital Control of Dynamic Systems, 3rd ed.* Addison Wesley, Menlo Park, Calif., 1998.
- [148] Z. Zhao, Y. Peng, and Y. Li, “Devices dissipation of series-resonant inverter under pulse-width phase-shift operating mode,” in *Proc. of Asia-Pacific Power and Energy Engineering Conference, (APPEEC) 2010*, pp. 1-4, Mar. 2010.
- [149] International Organization for Standardization, *Implants for surgery – active implantable medical devices – Part 1: General requirements for safety, marking, and for information to be provided by the manufacturer*, ISO 14708-1, 2000.